ELECTROPRODUCTION OF KAONS ON HYDROGEN AND DEUTERIUM

Douglas Michael Koltenuk

A DISSERTATION

in

PHYSICS

Presented to the Faculties of the University of Pennsylvania in Partial Fulfillment

of the Requirements for the Degree of Doctor of Philosophy

1999

H.T. Fortune

Supervisor of Dissertation

N. Lockyer

Graduate Group Chairperson

DEDICATION

To Mom and Dad

ACKNOWLEDGEMENTS

Certainly all the teachers I have been associated with over the years have contributed to getting me where I am today. One of the most influential was my high school math teacher Harry Kutch. He challenged me to be the best I could be, and taught me a number of valuable lessons about what life as an academic-type would be like. I also acknowledge Paul Karchin at Yale for giving me a summer job during which I discovered that particle/nuclear physics analysis was something that I liked and could do well.

From Penn I have to thank Dave Beatty for his help and advice during the time he was a postdoc. He wasn't such a bad roommate in that cockroach-infested excuse for an apartment that we cohabited for a while along with grad students Henry Leigh and Jin Yu. Paul Hausladen was quite helpful during my last days at Penn with the wisdom of a freshly-minted Ph.D.

The Hall C staff scientists, engineers, and technicians without whom the experiment never would have happened include Joe Beaufait, Paul Brindza, Roger Carlini, Jim Dunne, Rolf Ent, Mike Fowler, Steve Hickson, Paul Hood, Thia Keppel, Steve Lassiter, Dave Mack, Joe Mitchell, Steve Wood, and Bill Vulcan. Special thanks to Roger, for ensuring that I had an office and a real computer while I was full-time at JLab, and to Dave, who helped a great deal in my preparation for the pion experiment, and who continued to be involved during and after the kaon experiment.

Postdocs associated with Hall C who were quite helpful on the experiments and in the analysis include Ketevi Assamagan, Paul Gueye, Haiyan Gao, Ole Hansen, Mike Miller, and John Price. Professors who provided wisdom over the years include Keith Baker, Ron Gilman, Pete Markowitz, Ralph Segel, and Paul Stoler.

The Hall C original students, some of whom had already put in long service at JLab before I arrived, are Chris Armstrong, John Arrington, Chris Bochna, Jinseok Cha, Chris Cothran, Dipankar Dutta, Valera Frolov, Dave Meekins, Rick Mohring, Gabriel Niculescu, Ioana Niculescu, Bart Terburg, and Derek Van Westrum. Others who came later that I worked closely with are Steve Avery, Dave Gaskell, Kenneth Gustafsson, and Jochen Volmer. Jinseok has been quite helpful as the fellow graduate student on the experiment. I need to give him credit for finding the discrepancy in the comparison between data and simulation that led to the major breakthrough in the understanding of the data. I owe the fact that I stayed sane during my years in Newport News to Chris Armstrong, since he was both the person I talked the most to about physics and analysis issues, as well as the person with whom I spent the most time socially along with his family (Alex, Josh, Lara, and Katharine) and friends (Sandy, Bari, Dave, and Jennifer). In his honor I'll say, "Go Vegan!"

Now I need to start mentioning those at Argonne National Laboratory who took me in and helped me immensely while I was there. The senior scientists responsible for bringing me to Argonne are Don Geesaman, Hal Jackson, and Ben Zeidman. Hal started my involvement with JLab by inviting me to be a part of his pion experiment, and Ben was kind enough to find room in his kaon experiment when Hal's experiment was significantly delayed. I owe Ben a great deal for that, as well as for his help and guidance over the years. The Argonne postdocs who were involved in Hall C, the kaon experiment, and its later analysis are Kevin Bailey, Bill Cummings, Dirk DeSchepper, Bryon Mueller, Tom O'Neill, David Potterveld, and Joerg Reinhold, with David and Joerg putting in the most work. Without Joerg this analysis would have never been finished, as his contribution has been so immense, I can't even begin to quantify it. Sharing an office with him for a year at Argonne was worth several years of analysis on my own. Also, he took on the responsibility of reviewing my thesis when he wasn't even on my thesis committee. I salute you, Joerg.

I've been associated with my advisor, Terry Fortune, from the first days I stepped onto the Penn campus. He has provided me with numerous opportunities over the years, including making the initial pitch to Hal Jackson that led me to do my thesis experiment at JLab, for which I am quite grateful to have had the opportunity. He gave me the freedom and space I needed as a graduate student to flourish, and he trusted my judgment and my ability to move myself along. I thank him for all he has given me during my time at Penn.

To the friends who have been with me the whole time, Lara, Ihor, and Spence, and to the friends who have played a large role over the last six years, Ana, Francesca, Anna, Aimee, and Tracy, I thank you all for being a part of my journey and supporting me along the way.

I thank Philadelphia for allowing me not to get shot, I thank Newport News for having video stores and good supermarkets, and I thank Chicago for being all that a city should be and more.

Of course, I must also thank my family, who has been with me and behind me my entire life. My parents raised me in an environment where educational achievements were important and valued, but they were only one part of a balanced life. Also, they never put up any obstacles to where I might go, and gave me the support to make my dreams realities. They also let me live with them these past seven months, and their help and patience are much appreciated. My sister Danielle and my Nana get special mentions for also giving me lots of love over the years. And for my grandparents that have passed on over the years, I know you are all very proud of me.

ABSTRACT

ELECTROPRODUCTION OF KAONS ON HYDROGEN AND DEUTERIUM

Douglas Michael Koltenuk

H.T. Fortune

High-statistics data have been acquired for the reactions p(e,e$'$K$^+$) and d(e,e$'$K$^+$) over a range of W from 1.70–1.95 GeV. Coincidence measurements at Q^2=0.38, 0.50, and 0.52 GeV^2 cover a range of virtual photon-kaon angles for both liquid hydrogen and deuterium targets. Monte Carlo simulations have been matched to the data in order to extract cross sections. The W-dependence of the p(e,e$'$K$^+$)Λ and p(e,e$'$K$^+$)Σ^0 cross sections deviates from a previous model fitted to photoproduction data. The difference in cross sections on hydrogen and on the proton in deuterium has been quantified for Λ production. The subtraction of the Λ and Σ^0 contribution from the proton in the deuteron allows the extraction of n(e,e$'$K$^+$)Σ^- cross sections. The wealth of new data on Λ, Σ^0, and Σ^- production will put tight constraints on existing models for kaon production and form factors.

Table of Contents

List of Tables

List of Figures

Chapter 1

Introduction

1.1 Experimental Overview

The construction and commissioning of Thomas Jefferson National Accelerator Facility (TJNAF) marks a new era in the study of the subatomic universe. Since TJNAF is an intermediate-energy accelerator, it has the capability to probe both nucleon and quark structure in nuclei. Currently, the physics world speaks in two separate languages: nuclear and particle. The first major steps toward bridging the gap between looking at nuclei using strictly hadronic OR partonic degrees of freedom will be taken at TJNAF. The reason why these first steps will emerge from TJNAF is its high current, continuous-wave (CW) electron beam. Measurements that would have taken months to do at other accelerators can be performed in days at TJNAF. In addition, the 100% duty factor allows for better signal-to-noise ratios than one could achieve elsewhere. The limiting factor in data acquisition is often the detector hardware and logic electronics rather than the physics event rate. We have taken advantage of this high quality beam to do the world's first precision study of the electroproduction of kaons on deuterium.

The understanding of kaon electroproduction is presently limited to a phenomenological one. Limited amounts of data, the lack of overlap in invariant mass ranges of electro- and photoproduction measurements, and the poor statistical quality of the data force theories to find a best fit of coupling constants and parameters of kaon form factors. Precision kaon electroproduction data are required in order to tightly constrain the variables in these theories. Fundamental questions such as the relative importance of Born terms and resonance terms can be answered. This paper will present some of the world's best measurements of electroproduction cross sections of Λ and Σ^0 on hydrogen, as well as the first measurements below W=1.95 GeV.

There is very little that is currently known about the interactions of baryons containing strange quarks. Kaon electroproduction on deuterium leaves a residual strange baryon Y (Λ, Σ^0, or Σ^-) and a nucleon, and studying the outgoing kaons and electrons provides information on both the K–Y–N coupling constants and the strength of the Y–N interaction. Information on the Y–N interaction is necessary for realistic descriptions to be made of hypernuclei (bound nuclear states that include a strange baryon). Also, threshold effects and interference terms can be studied using a missing mass spectrum with a high statistics yield. Predictions about the existence of strange dibaryons can be tested. The production of kaons on the neutron in deuterium can be measured. The cross section for this reaction can be used to further constrain theoretical models for kaon electroproduction. Previous to TJNAF, the only way to explore any of these topics has been through indirect studies involving pion intermediate states. We have done a direct and detailed study of these interactions for the first time. This paper will present the world's first separation of the Λ, Σ^0, and Σ^- production cross sections on deuterium.

1.2 Kaon Electroproduction on Hydrogen

1.2.1 Kinematic Formalism

Experiment E91–016 measures the semi-exclusive cross section p(e,e$'$K$^+$)Y that can be expressed in terms of a five-fold differential cross section $\frac{d^5\sigma}{dE_{e'}d\Omega_{e'}d\Omega_K}$. This five-fold differential cross section can be reduced to a center-of-mass cross section by use of the formula

$$\frac{d^5\sigma}{dE_{e'}d\Omega_{e'}d\Omega_K} = \Gamma J \frac{d^2\sigma}{d\Omega_{K(cm)}}, \tag{1.1}$$

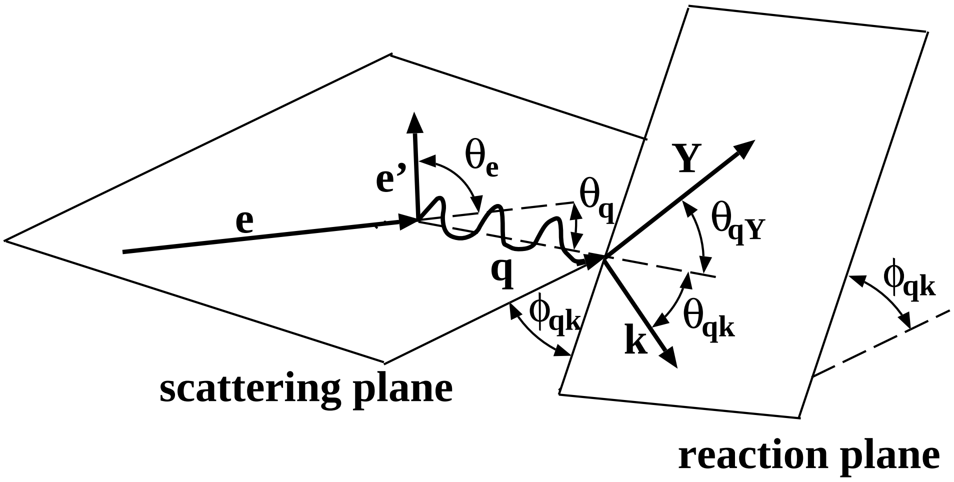

Figure 1.1: Coordinate systems in the scattering and reaction planes for kaon electroproduction.

where Γ is the virtual-photon flux factor,

$$\Gamma = \frac{\alpha}{2\pi^2}\frac{E'}{E}\frac{W^2 - M^2}{2MQ^2}\frac{1}{1-\epsilon}, \tag{1.2}$$

and J is the Jacobian $\frac{d\Omega_{K(cm)}}{d\Omega_K}$. Here E is the initial electron energy, E$'$ is the final electron energy, M is the mass of the proton, W is the invariant mass of the virtual photon-plus-proton system, and Q^2 is the absolute value of the invariant mass squared of the virtual photon. The relevant vectors can be seen in Fig. 1.1.

If we define in the lab frame the four-vector e as (E,0,0,E) (neglecting electron mass), the virtual-photon vector q can be further described as

$$q = e - e' = (\omega, q\sin\theta_q, 0, q\cos\theta_q) = (\omega, \mathbf{q}), \tag{1.3}$$

where ω=E-E$'$. The virtual transverse photon polarization ϵ is given by

$$\epsilon = \frac{1}{1 + 2(1 + \frac{\omega^2}{Q^2}) \tan^2(\frac{\theta_{e'}}{2})}, \tag{1.4}$$

and the virtual longitudinal photon polarization ϵ_L is given by $\epsilon_L = -\frac{q^2}{\omega^2}\epsilon$. The center-of-mass cross section $\frac{d^2\sigma}{d\Omega_{K(cm)}}$ (hereafter referred to as $\frac{d\sigma}{d\Omega_{cm}}$) can be further broken down according to [Dav96],

$$\frac{d\sigma}{d\Omega_{cm}} = \frac{d\sigma_T}{d\Omega_{cm}} + \epsilon_L \frac{d\sigma_L}{d\Omega_{cm}} + \epsilon \cos 2\phi_{qk} \sin^2\theta_{qk} \frac{d\sigma_{TT}}{d\Omega_{cm}} + \sqrt{2\epsilon_L(\epsilon + 1)} \cos\phi_{qk} \sin\theta_{qk} \frac{d\sigma_{LT}}{d\Omega_{cm}}, \tag{1.5}$$

where $\frac{d\sigma_T}{d\Omega_{cm}}$ represents the contribution from unpolarized transverse photons, $\frac{d\sigma_L}{d\Omega_{cm}}$ from longitudinally polarized photons, $\frac{d\sigma_{TT}}{d\Omega_{cm}}$ from transverse linearly polarized photons, and $\frac{d\sigma_{LT}}{d\Omega_{cm}}$ from interference between the transverse and longitudinal components.

If we label the initial target proton vector as p=(M$_p$,0,0,0), then the relevant invariant quantities for E91–016 can be written as follows:

$$s = W^2 = (q + p)^2 = (M_p + \omega)^2 - \mathbf{q}^2, \tag{1.6}$$

$$Q^2 = -q^2 = \mathbf{q}^2 - \omega^2, \tag{1.7}$$

$$\text{Missing Mass}^2 = M_x^2 = (q + p - k)^2. \tag{1.8}$$

Missing Mass M_x is equal to the sum of the masses of the undetected particles in the final state. For p(e,e$'$K$^+$), the missing-mass spectrum has two sharp peaks

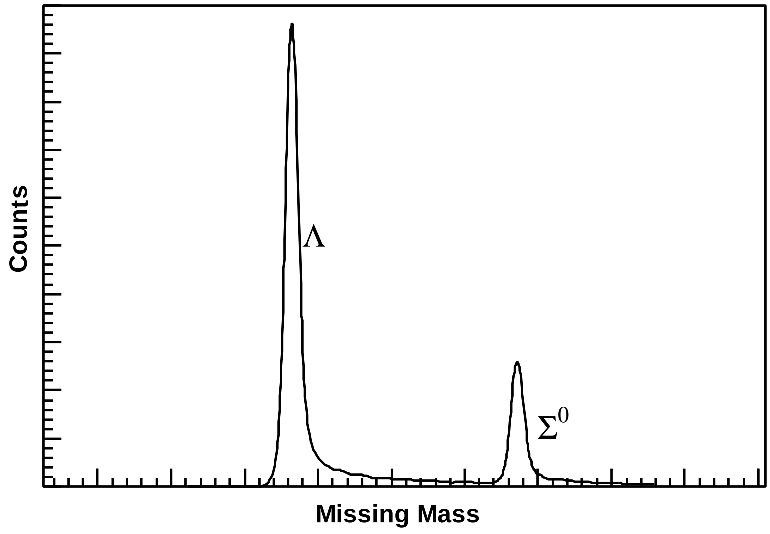

Figure 1.2: Cartoon missing-mass spectrum for p(e,e$'$K$^+$)Y.

at the Λ and Σ^0 masses of 1116 and 1193 MeV (note: in this paper factors of c will be dropped, such that masses and momenta will be expressed in terms of energies) with radiative tails due to additional photons in the final state that grow weaker as missing mass increases (see Fig. 1.2 for a cartoon drawing of how the hydrogen spectra will look).

1.2.2 Previous Experimental Data

The experimental data set for kaon production from hydrogen is sparse. Most of the data were taken before 1980 at electron accelerators with low duty cycles and low kaon counting rates limiting the ability to reduce statistical uncertainties. Missing-mass spectra from previous experiments are presented in Figs. 1.3 and 1.4.

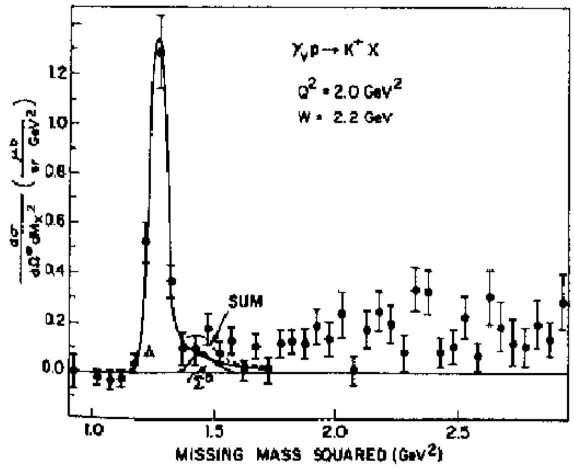

Figure 1.3: Missing-mass squared spectrum for p(e,e′K$^+$)Y, with the vertical axis in cross-section units. Note the broad Λ resolution and the Σ^0 peak appearing as a small shoulder on the side of the Λ peak. From [Beb77].

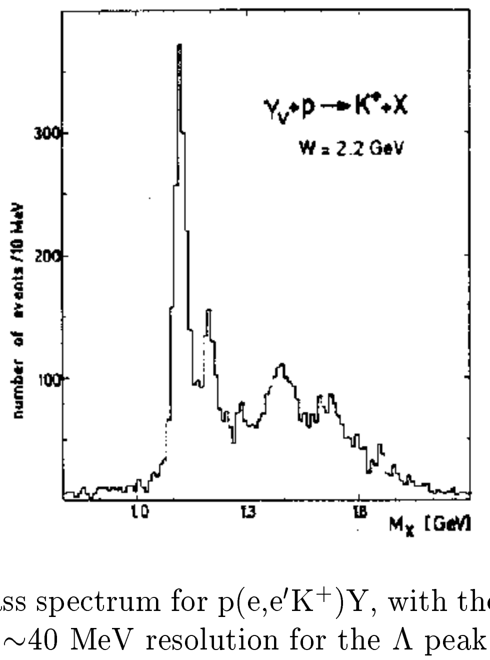

Figure 1.4: Missing-mass spectrum for p(e,e′K$^+$)Y, with the vertical axis in events per 10 MeV. Note the ~40 MeV resolution for the Λ peak and the overlap of the Λ and Σ^0 peaks. From [Bra79].

Resolutions are poor (considering the widths of the Λ and Σ^0 are less than 1 MeV), and overlap of Λ and Σ^0 contributions are significant. Data came from one of three different types of experiments: photoproduction (Q^2=0), electroproduction, and radiative capture with kaon beams. A new batch of data is just now starting to emerge (or will be emerging soon) from a number of next-generation accelerators: along with JLab, there is ELSA (Electron Stretcher Accelerator), ESRF (European Synchrotron Radiation Facility), and the SPring-8 8 GeV Synchrotron under construction in Japan. New photoproduction data from ELSA were published in 1994. Nonetheless, the majority of data comes from experiments that ran from the late 60s to 1979. Also, the photoproduction and electroproduction data sets cover different kinematic ranges in W. Photoproduction experiments generally covered the region from threshold to W=2.0 GeV, whereas electroproduction experiments tended to have an average W of 2.2 GeV, and they never explored the region below 1.95 GeV. The reason to look at higher W in electroproduction experiments was to avoid the influence of resonances that might dominate in the region below W=2.0 GeV. Photoproduction experiments can be more bold since they have fewer degrees of freedom (no Q^2 or ϵ dependences) to sort out. However, this lack of overlap between photo- and electroproduction data sets made it difficult to create theoretical models that are effective over all kinematic ranges, as will be seen below.

It was found in early photoproduction studies that the W–dependence of the cross section behaved as [Boy69]

$$\frac{d\sigma}{dt} = \frac{1}{(W^2 - M^2)^2}|ME|^2, \tag{1.9}$$

where $|ME|^2$ represents the square of the assumed W–independent matrix element. This formula was transformed to apply to electroproduction [Beb77]:

$$\frac{d\sigma}{d\Omega} = \frac{|p_k^*|}{(W^2 - M^2)W}|ME|^2, \tag{1.10}$$

where $|p_k^*|$ is the momentum of the kaon in the center-of-mass frame. With this scaling formula, Bebek scaled all the existing data to a common W (2.15 GeV) and extracted Q^2 dependences for Λ and Σ^0 production at central angles ($\theta_{qk(cm)}$ less than 15^o). These fits are shown in Fig. 1.5 and Fig. 1.6. The question as to whether these extracted W- and Q^2-dependences are valid in the resonance region below 1.95 GeV is one that will be answered by our experiment.

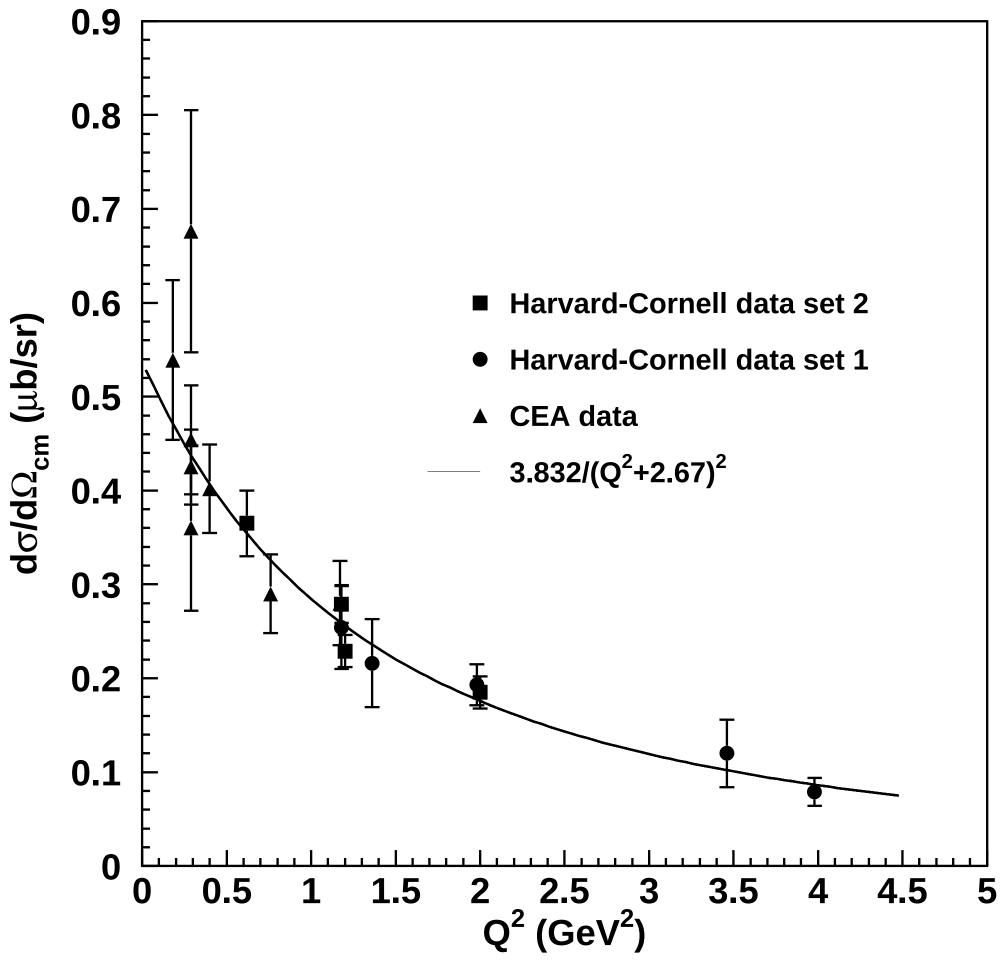

Figure 1.5: Previous data for p(e,e$'$K$^+$)Λ. All points are scaled in W to 2.15 GeV as described in the text. From [Beb77].

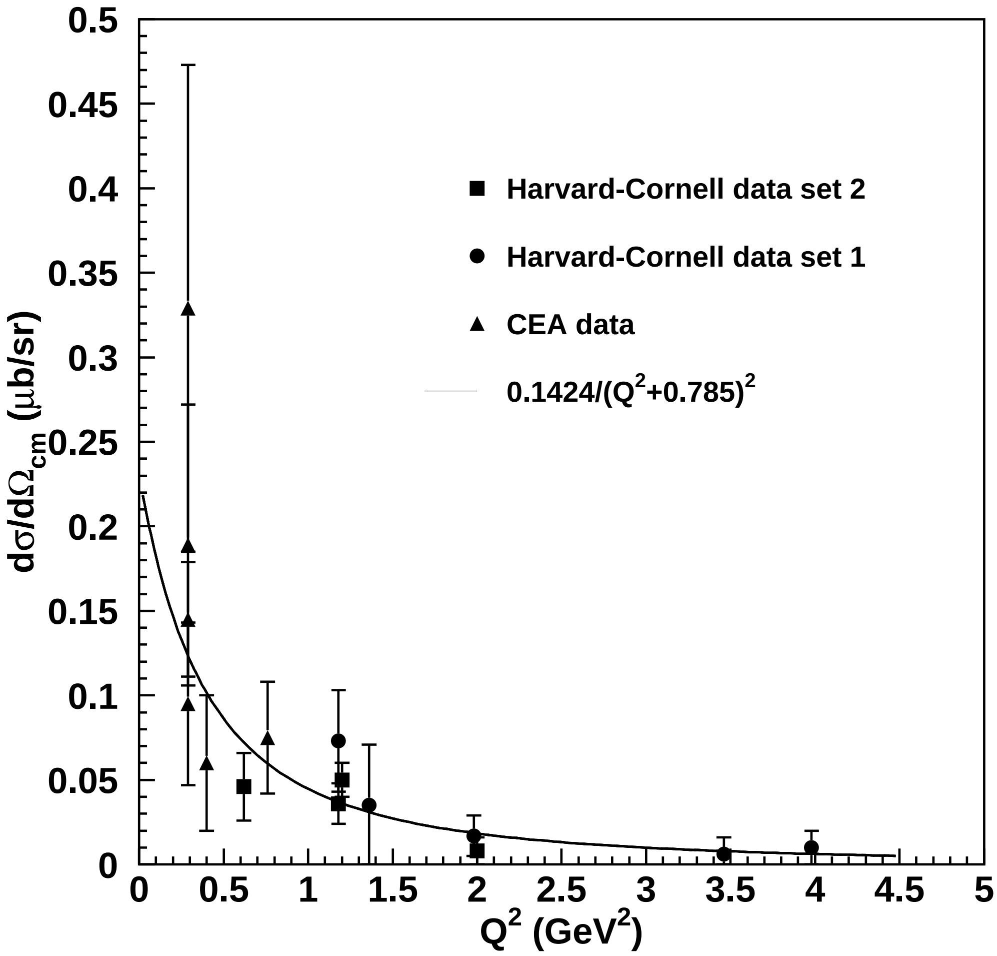

Figure 1.6: Previous data for $p(e,e'K^+)\Sigma^0$. All points are scaled in W to 2.15 GeV as described in the text. From [Beb77].

Table 1.1: Table of unscaled cross sections corresponding to the scaled cross sections shown in Fig. 1.5 and Fig. 1.6. From [Beb77].

W GeV	Q^2 GeV^2	ϵ	$\theta_{qk(cm)}$ deg	$\frac{d\sigma}{d\Omega_{cm}}(K^+\Lambda)$ μb/sr	$\frac{d\sigma}{d\Omega_{cm}}(K^+\Sigma^0)$ μb/sr
		Harvard-Cornell data set 2			
2.17	1.18	0.94	8.0	0.251±0.043	0.073±0.030
2.15	1.98	0.94	9.1	0.193±0.022	0.017±0.012
2.17	3.98	0.88	9.0	0.078±0.015	0.010±0.010
2.85	1.36	0.87	10.4	0.142±0.031	0.024±0.025
2.51	3.46	0.85	10.0	0.097±0.029	0.005±0.008
		Harvard-Cornell data set 1			
2.67	0.62	0.86	7.8	0.267±0.026	0.035±0.015
2.66	1.20	0.86	8.4	0.169±0.012	0.038±0.008
2.66	2.00	0.82	7.5	0.137±0.013	0.006±0.006
2.20	1.18	0.94	7.4	0.272±0.019	0.035±0.012
		CEA data			
2.17	0.18	0.85	5.9	0.553±0.084	
2.17	0.29	0.88	5.9	0.499±0.057	0.094±0.048
2.17	0.40	0.86	5.9	0.398±0.013	0.060±0.040
2.17	0.76	0.81	5.9	0.287±0.019	0.075±0.033
2.17	1.17	0.78	5.9	0.277±0.013	
1.93	0.29	0.93	6.0	0.732±0.019	0.336±0.147
2.10	0.29	0.90	6.0	0.369±0.013	0.192±0.084
2.48	0.29	0.74	6.0	0.350±0.019	0.123±0.029

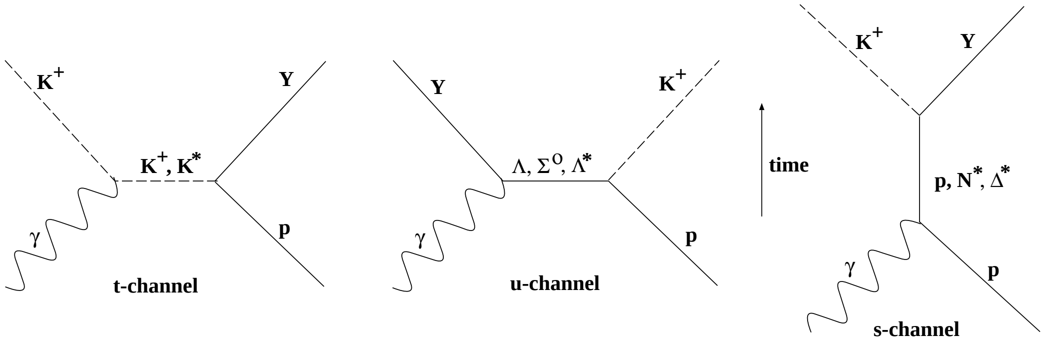

Figure 1.7: Lowest-order Feynman diagrams for p(e,e′K$^+$)Y.

1.2.3 Theoretical Predictions

Tree-level Feynman diagrams describing p(e,e′K$^+$)Y are displayed in Fig. 1.7. Whether the reaction goes through the s, t, or u-channel determines whether the propagator is a baryon (p,N*,Δ*), a strange meson (K$^+$,K*), or a strange baryon (Λ,Σ^0,Λ*). A list of particles used as propagators that are referenced in tables below is presented in Table 1.2. Kaonic form factors and strange coupling constants come into play at the vertices. These numbers become parameters to be varied in a theoretical model for kaon electroproduction. A variety of choices for which diagrams are used in models can be seen in Table 1.3. Due to the differences of each group's theoretical models, a different set of resonances is used by each group to provide a phenomenological fit to the experimental data.

Differences arise not only because of variations in theoretical frameworks, but also due to the poor quality of the experimental data, which in some cases are not

Table 1.2: Table of particle masses. From [Dav96].

Notation	Particle	(I)J^π	Mass (MeV)	Width (MeV)
	p	$1/2^+$	938.27	
	n	$1/2^+$	939.57	
	d	$(1)1/2^+$	1875.63	
	K^+	0^-	493.68	
	Λ	$1/2^+$	1115.68	
	Σ^0	$1/2^+$	1192.64	
	Σ^-	$1/2^+$	1197.45	
K*	K*(892)	1^-	892	50
K1	K1(1270)	1^+	1273	90
N1	N(1440)	$(1)1/2^+$	1440	350
N4	N(1650)	$(0)1/2^-$	1650	150
N6	N(1710)	$(1)1/2^+$	1710	100
N7	N(1720)	$(1)3/2^+$	1720	150
N8	N(1675)	$(2)5/2^-$	1680	150
L1	Λ(1405)	$(0)1/2^-$	1407	50
L3	Λ(1670)	$(0)1/2^-$	1670	35
L5	Λ(1810)	$(1)1/2^+$	1810	150
S1	Σ(1660)	$(1)1/2^+$	1660	100
D1	Δ(1620)	$(0)1/2^-$	1620	150
D2	Δ(1900)	$(0)1/2^-$	1900	200
D3	Δ(1910)	$(1)1/2^+$	1910	250
D4	Δ(1232)	$(1)3/2^+$	1235	131
D7	Δ(1920)	$(1)3/2^+$	1920	200

Table 1.3: Resonances used and extracted values for main coupling constants for theories by AS [Ade90], WJC [Wil92], and MBH [Mar95]. From [Dav96].

Theory	t-channel	u-channel	s-channel	$\frac{g_{K\Lambda N}}{\sqrt{4\pi}}$	$\frac{g_{K\Sigma N}}{\sqrt{4\pi}}$
AS	K*,K1	L3	N1	-4.17±0.75	1.18±0.66
WJC	K*,K1	L1	N4,N6,D1,D2,D3	-2.38	0.27
MBH	K*	–	N4,N6,D2,D3	0.51	0.13

internally self-consistent [Ade90]. For a long time no theory that focussed on the photoproduction kinematic range (W below 2.0 GeV) was able to reproduce the data in the electroproduction kinematic range, and vice versa [Ade88]. Clearly a higher-quality set of data is required. In the meantime, the different theories can generate vastly different values for coupling constants, as can be seen in Tables 1.4 and 1.5. These discrepancies lead to fundamental disagreements as to whether kaon production reactions below W=2.0 GeV are resonance dominated [Ben99] or not [Boc94]. It should be pointed out that the SU(3)-predicted values for $\frac{g_{K\Lambda N}}{\sqrt{4\pi}}$ and $\frac{g_{K\Sigma N}}{\sqrt{4\pi}}$ are -3.70 ± 0.70 and 1.10 ± 0.20, respectively. The fact that a number of the theories have coupling constants outside of these ranges is not necessarily evidence for symmetry breaking. Haberzettl proposes that the proper inclusion of a hadronic form factor at the vertex leads to values for the coupling constants within the SU(3) range, in his case -3.80 and 1.20 [Hab98].

Table 1.4: Coupling constants corresponding to the exchanged particles in the KΛ channels from models AS [Ade90], WJC [Wil92], and SL[Dav96]. From [Dav96].

Particle	Coupling	AS	WJC	SL
Λ	$g_{K\Lambda N}/\sqrt{4\pi}$	-4.17±0.75	-2.38	-3.16±0.01
Σ	$g_{K\Sigma N}/\sqrt{4\pi}$	1.18±0.66	0.27	0.91±0.10
K*	$G_V/4\pi$	-0.43±0.07	-0.16	-0.05±0.01
	$G_V/4\pi$	0.20±0.12	0.08	0.16±0.02
K1	$G_{V1}/4\pi$	-0.10±0.06	0.02	-0.19±0.01
	$G_{T1}/4\pi$	-1.21±0.33	0.17	-0.35±0.03
N1	$G_{N1}/\sqrt{4\pi}$	-1.41±0.60		-0.01±0.12
N4	$G_{N4}/\sqrt{4\pi}$		-0.04	
N6	$G_{N6}/\sqrt{4\pi}$		-0.06	
N7	$G^a_{N7}/4\pi$			-0.04±0.01
	$G^b_{N7}/4\pi$			-0.14±0.04
N8	$G^a_{N8}/4\pi$			-0.63±0.10
	$G^b_{N8}/4\pi$			-0.05±0.56
L1	$G_{L1}/\sqrt{4\pi}$		-0.07	-0.31±0.06
L3	$G_{L3}/\sqrt{4\pi}$	-3.17±0.86		1.18±0.09
L5	$G_{L5}/\sqrt{4\pi}$			-1.25±0.20
S1	$G_{S1}/\sqrt{4\pi}$			-4.96±0.19

Table 1.5: Coupling constants corresponding to the exchanged particles in the KΣ channels from models MBH [Mar95], WJC [Wil92], and SL[Dav96]. From [Dav96].

Particle	Coupling	MBH	WJC	SL
Λ	$g_{K\Lambda N}/\sqrt{4\pi}$	0.51	-2.38	-3.23±0.17
Σ	$g_{K\Sigma N}/\sqrt{4\pi}$	0.13	0.27	0.80±0.10
K*	$G_V/4\pi$	0.05	0.11	0.02±0.01
	$G_V/4\pi$	0.05	-0.14	-0.07±0.02
K1	$G_{V1}/4\pi$		-0.13	-0.05±0.01
	$G_{T1}/4\pi$		0.07	0.23±0.04
N1	$G_{N1}/\sqrt{4\pi}$			-0.95±0.11
N4	$G_{N4}/\sqrt{4\pi}$	0.08	0.09	
N6	$G_{N6}/\sqrt{4\pi}$	0.57	0.47	
N7	$G^a_{N7}/4\pi$			-0.04±0.02
	$G^b_{N7}/4\pi$			-0.53±0.06
N8	$G^a_{N8}/4\pi$			2.02±0.20
	$G^b_{N8}/4\pi$			3.91±0.57
L1	$G_{L1}/\sqrt{4\pi}$		0.46	-0.42±0.03
L3	$G_{L3}/\sqrt{4\pi}$			-0.10±0.09
L5	$G_{L5}/\sqrt{4\pi}$			6.01±0.23
S1	$G_{S1}/\sqrt{4\pi}$			-1.72±0.21
D1	$G_{D1}/\sqrt{4\pi}$		-0.03	
D2	$G_{D2}/\sqrt{4\pi}$	0.07	-0.06	
D3	$G_{D3}/\sqrt{4\pi}$	0.30	-0.51	0.43±0.04
D4	$G^a_{D4}/4\pi$			-0.47±0.06
	$G^b_{D4}/4\pi$			-1.88±0.14
D7	$G^a_{D7}/4\pi$			0.05±0.01
	$G^b_{D7}/4\pi$			0.29±0.04

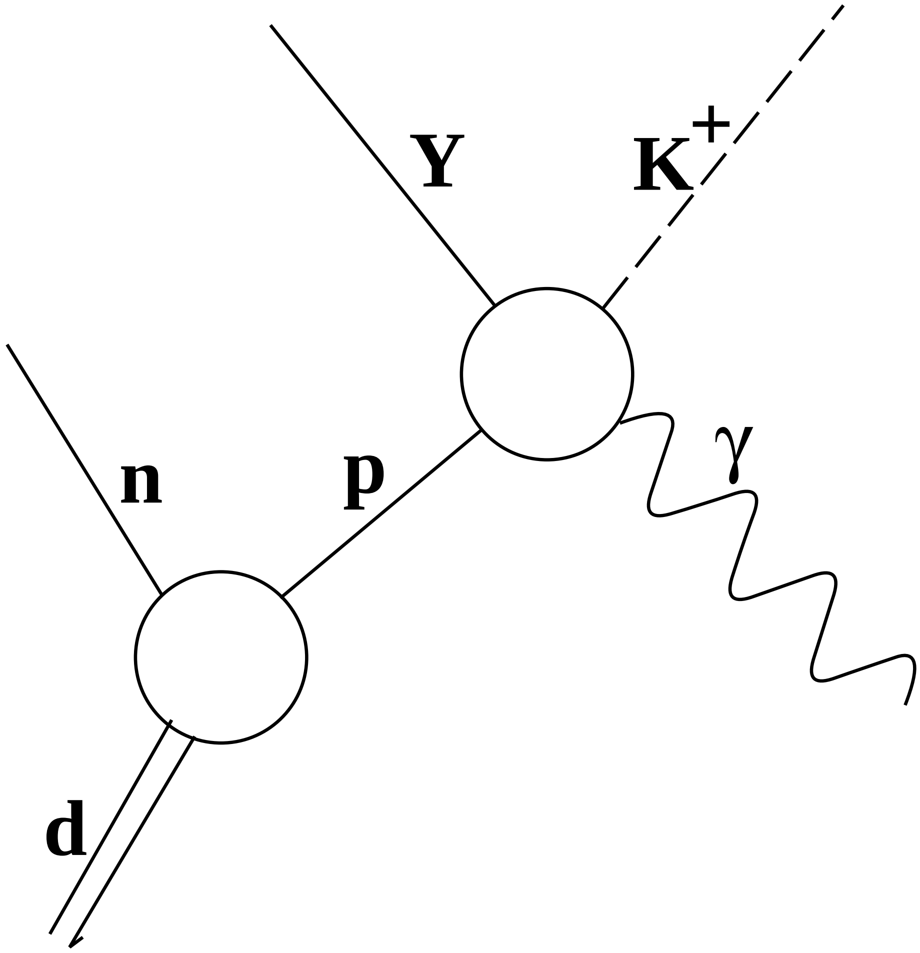

Figure 1.8: Schematic of Feynman diagram for d(e,e′K$^+$)Yn.

1.3 Kaon Electroproduction on Deuterium

1.3.1 Kinematic Formalism

There are three final states that can be accessed in the reaction d(e,e′K$^+$): Λn, Σ^0n, and Σ^-p. The basic diagram describing d(e,e′K$^+$)Yn is shown in Fig. 1.8. In the impulse approximation, we expect the cross sections for Λn and Σ^0n to have the same physics dependences (W, Q^2, $\theta_{qk(cm)}$) as the corresponding Λ and Σ^0 cross sections in hydrogen. However, there are complicating factors. In the rest frame of the deuteron, the initial proton and neutron have equal and opposite momenta (Fermi motion). The distribution of nucleon momenta is given by the deuteron wave function calculated based on the full Bonn potential, which uses the independent particle shell model and includes the contribution of the s- and d-waves [Mac87]. Other potentials could be used, but all of the deuteron wavefunctions agree except at the very high momentum tails.

Besides Fermi motion, there is also the issue as to whether the nucleons are on- or off-shell. The standard way of dealing with the problem is to first assume that the spectator nucleon is on-shell. Now all the particles in the initial (e,d) and final (e',K^+, Y,N) states are on-shell. The initial target nucleon is then off-shell, with mass less than the rest mass of the nucleon. Adelseck describes three different ways of treating the issue [Ade88]:

1) Impulse Approximation: ignore the fact that the target nucleon is off-shell, ignore p-wave contributions in the deuteron wave function

2) conserve energy and momentum at all vertices, assume the target nucleon obeys the Dirac equation, and neglect p-wave contributions: this method has the problem of being internally inconsistent

3) exact description: this method generates non gauge-invariant terms

In the end, off-shell effects account for less than 3% of the total cross-section strength [Ade88]. The approach taken here is to assume the *spectator* nucleon is on-shell when conserving energy and momentum. However, when calculating kinematic quantities such as θ_{cm}, the *target* nucleon is assumed to be on-shell. Invariant mass W is calculated for the target nucleon being both on- and off-shell for comparison purposes. These assumptions are a source of systematic error in the comparison between hydrogen and deuterium cross sections. The basic form of the formula comparing deuterium cross sections to elementary hydrogen cross sections is [Ade88]

$$d\sigma_{deuterium} = d\sigma_{hydrogen}(1 + \beta_n \cos\theta_n)|\Psi(\vec{p}_n)|^2 d^3p_n, \tag{1.11}$$

where Ψ is the deuterium wave function and β_n represents the velocity of the spectator in the lab frame. The effect of this term is expected to be negligible for kaon photoproduction [Li92].

1.3.2 Final-State Interactions

There are a number of possible final-state interactions that can modify the deuterium cross section relative to the hydrogen cross section. Interactions between the kaon and hyperon (K–Y) are already present in hydrogen, so they are ignored. Interactions between the kaon and spectator nucleon (K–N) are considered to be weak due to the small K^+N interaction cross section [Coo61,Dov82], and no studies have been done considering 3-body effects. The dominant final-state interaction will be due to Y–N scattering. The strength of this effect will be a function of the scattering length and the effective range for a given potential, and there are few previous experimental data that can be used to pin these quantities down. The strongest enhancement will be near the threshold for Λ production, and the strength will drop off rapidly as the virtual photon energy increases. The enhancement will also be strongest at forward angles, where the momentum transfer to the baryonic system is minimized. Also, the nucleon being in its lowest momentum state (to avoid suppression by its own wavefunction) enables maximum interaction, so the hyperon has to be headed in the forward direction as well [Ade88]. In general, the smaller the relative momentum between nucleon and hyperon, the greater the chance of interaction. This experiment is expected to show as clear a picture as possible of the strengths of Λ–n, Σ^0–n, and Σ^-–p final-state interactions. Of particular interest is whether a bound Σ^-–p state can be seen.

1.3.3 Previous Data and Theory

Considering the poor resolution of the hydrogen spectra shown in Fig. 1.3, one can imagine how fuzzy the deuterium spectra taken during that same experiment must have looked. Imagine one must, since there has never been a deuterium missing-mass spectrum published before our experiment. The previous measurements for

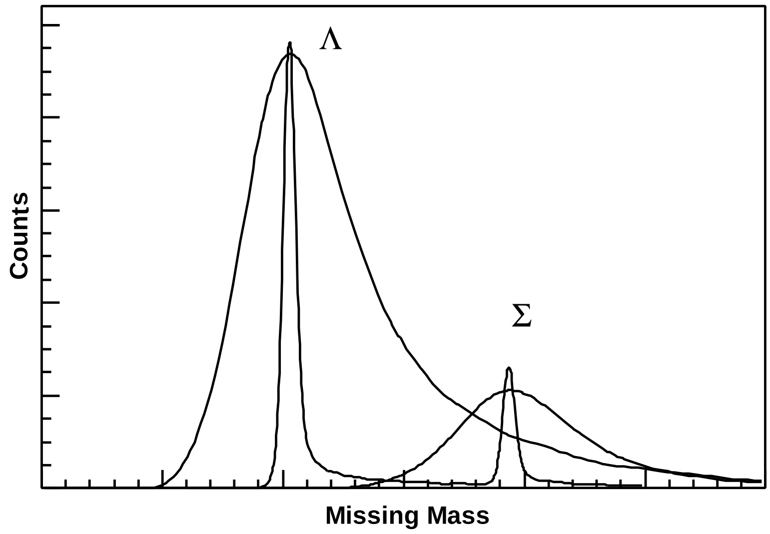

Figure 1.9: Cartoon of effect of Fermi motion on missing-mass spectra. Deuterium peaks overlay their corresponding hydrogen peaks.

d(e,e$'$K$^+$)Σ^-p are listed in Table 1.6. The errors are tremendous because of the low statistics available and the uncertanties in the extraction technique. These uncertainties are partially due to the Fermi-broadening of the missing-mass peaks (see Fig. 1.9 for a cartoon of this effect). In the region of missing mass above the threshold for Σ production, the contribution from Λ production is as great as the contribution from Σ production. To further complicate matters, the difference in masses between the Σ^0 and Σ^- is only 5 MeV, so it is possible to resolve only a combined Σ peak, and not possible to directly measure Σ^0 and Σ^- contributions. If a cross section for Σ^- is desired, the cross section for the Σ^0 needs to be subtracted, which is done by extrapolating from what was learned about Λ and Σ^0 production on hydrogen at the same kinematic settings. The cross sections in Table 1.6 have

Table 1.6: Table of Σ cross sections on hydrogen and deuterium. From [Beb77].

W GeV	Q^2 GeV^2	ϵ	$\theta_{qk(cm)}$ deg	$\frac{d\sigma}{d\Omega_{cm}}(K^+\Sigma)\vert_D / \frac{d\sigma}{d\Omega_{cm}}(K^+\Sigma^0)\vert_H$	$\frac{d\sigma}{d\Omega_{cm}}(K^+\Sigma^0)\vert_H$ μb/sr	$\frac{d\sigma}{d\Omega_{cm}}(K^+\Sigma^-)\vert_D$ μb/sr
2.83	1.29	0.88	10.6	1.60±1.40	0.040±0.029	0.014±0.034
2.16	1.20	0.94	8.4	1.76±0.86	0.073±0.030	0.055±0.063
2.15	3.97	0.88	8.2	1.20±2.51	0.010±0.010	0.002±0.025

error bars of greater than 100% for Σ^- cross sections, and 50–200% for combined Σ cross sections.

In photoproduction experiments, the ratio of Λ cross sections on deuterium and hydrogen was found to be 1.02±0.04±0.05 [Boy71], consistent with a simple absorption model estimate of 0.96. Also, the ratio of Σ cross sections on deuterium to those on hydrogen was found to be 2.37±0.11±0.12 in one experiment and 2.73±0.18 in another [Boy71,Qui79], and both experiments claimed the result they expected to get was 3, corresponding to pure t-channel isospin-1/2 exchange. The ratios in Table 1.6 range from 1.20–1.76, not in good agreement with the photoproduction measurements or with 3. One feature of many of the theoretical models of today is that they do not fit data from charged Σ production, mainly due to its scarcity and poor quality. Consequently, the existing models can have very different predictions for charged Σ production, and can overpredict the above data by factors of 100 or more [Mar95]. One very important benefit of obtaining precision Σ^- cross sections, besides being the first data of this quality of its kind, is that it will place greatly limiting constraints on existing theories.

Chapter 2

Experimental Setup

2.1 CEBA

As mentioned earlier, this experiment has become feasible only due to the construction of a next-generation electron accelerator at TJNAF, CEBA (Continuous Electron Beam Accelerator). The use of superconducting RF (radio frequency) technology gives CEBA an advantage over every existing electron accelerator. The layout of CEBA is in the form of a racetrack, with a pair of LINACs (Linear Accelerators) connected by circulation arcs. The electrons start in the injector, where they are accelerated through a potential to 45 MeV, and are grouped into micro-bunches 0.667 ns apart through chopping and focussing. Since the electrons are ultra-relativistic by the time they are out of the injector, each bunch travels

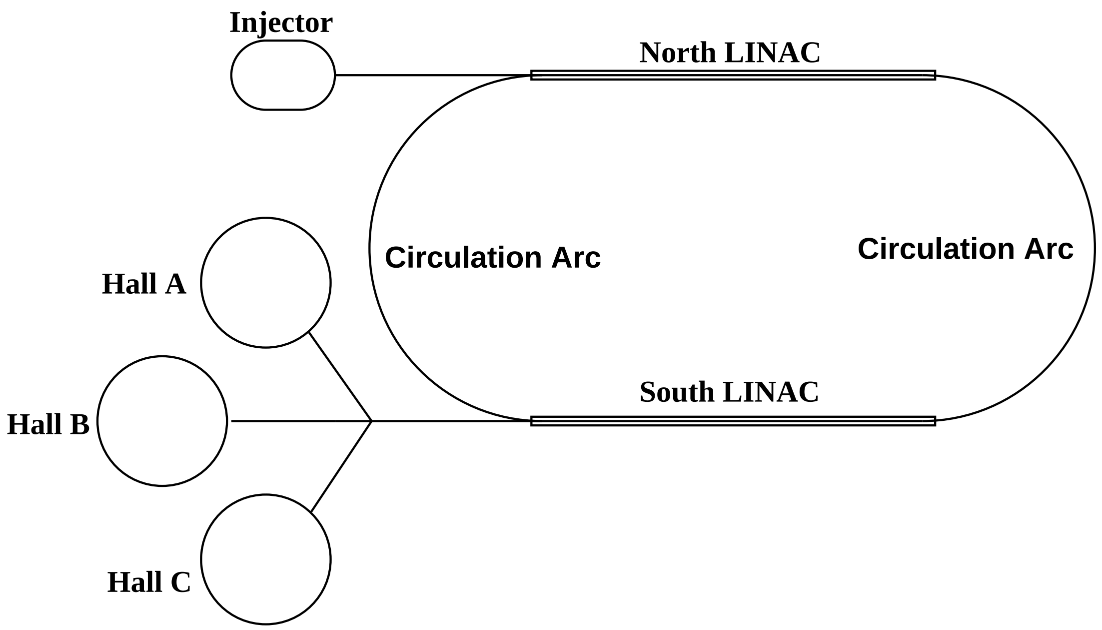

Figure 2.1: Continuous Electron Beam Accelerator

at essentially the speed of light, independent of the energy of the electrons. The maximum current for the accelerator is 200 μA. The electrons then enter the first LINAC region, where they are accelerated at approximately 5 MeV/meter, such that the total energy gain over the region is 400 MeV. The acceleration takes place in a series of superconducting niobium RF cavities cooled to 2 K, where the RF frequency (1.5 GHz) is coupled to the spacing of the micro-bunches. The advantage of having superconducting cavities is that there is no heating of the cavities due to the RF fields, so there is no limit on the duty factor of the beam.

After the first LINAC the electrons are bent around a circulation arc by a series of magnets. They next enter the second LINAC where they are accelerated another

400 MeV. Another circulation arc leads the electrons to the first LINAC, where they can be accelerated another 400 MeV. There are five circulation arcs after the first LINAC and four after the second LINAC, and each arc is configured to transport electrons at a given beam energy from one LINAC to the next. After each pass through a LINAC the electrons are momentum analyzed and sent through the appropriate circulation arc. We are then able to have five sets of electron bunches, all at different energies, being accelerated by the same RF cavities at the same time. The maximum electron energy achievable at 400 MeV/LINAC is therefore 4045 MeV. At the end of the second LINAC, electrons are momentum analyzed such that the electrons that have been accelerated to the desired beam energy can be sent towards the experimental halls rather than back through the set of circulation arcs. The electrons can be divided further down the line to turn into one of the three experimental halls. Each hall is designed to get one-third of the total number of beam bunches, such that the spacing of the bunches as they enter a hall is 2 ns.

2.2 Hall C Arc

The beam is steered through the accelerator with the help of 700 beam diagnostic devices placed at various points throughout its journey. Some of the most im-

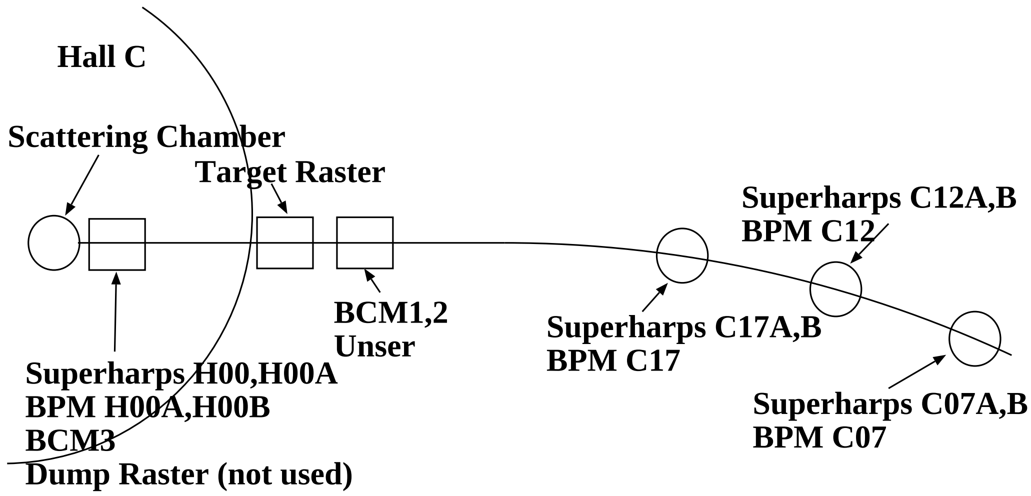

Figure 2.2: Hall C Beamline (not to scale).

portant devices for fine-tuning and calibration of the beam are placed in the final beam arc that leads into the Hall C experimental area (see Fig. 2.2). There are a number of beam position monitors (BPMs) that use a set of four antennas to determine where the beam is located in coordinates transverse to the beam direction. Comparing the beam positions at both ends of the arc allows for a measurement of the drift in beam energy from the nominal one if the beam is dispersively tuned [Kra93]. A better measurement can be done by a trio of Superharps located at the beginning, middle, and end of the arc. Superharps are a fine set of wires that sample the beam intensity as a function of transverse position in the beam pipe [Yan94]. Superharp scans are used to calibrate the BPMs, to make absolute energy measurements, and to study the emittance and dispersion of the beam. Current measurements are performed by an Unser monitor and by beam current monitors

(BCMs). The Unser monitor is a parametric current transformer that can calculate absolute current, but needs to have its zero offset calibrated. The BCMs are tuned RF cavities that measure the RF radiation of the beam, and can provide relative current measurements [Nic96]. Since we are using cryogenic targets, we use rastering magnets that cause an oscillation in the beam position in both the vertical and horizontal planes. Typical raster sizes are on the order of 1 mm. The beam position at the target is monitored by BPMs, so that the rastering can be verified and the central beam position can be monitored and adjusted.

2.3 Target

The electron beam travels through the Hall C beam arc, into the Hall C experimental area through a beam pipe, and then into the scattering chamber where the cryogenic targets are located. The cryotarget is a set of loops through which liquid hydrogen or liquid deuterium flow [Dun97] (see Fig. 2.3). The gases are cooled through heat exchange with liquid helium, the flow is regulated by fans, and the temperature is stabilized by heaters. The target configuration is in the shape of a beer can approximately 4 cm long in the direction of the incoming beam. Temperature is measured by Cernox resistors to a precision of 0.05 K. The nominal temperature and pressure for hydrogen is 19 K and 24 psi, and for deuterium is

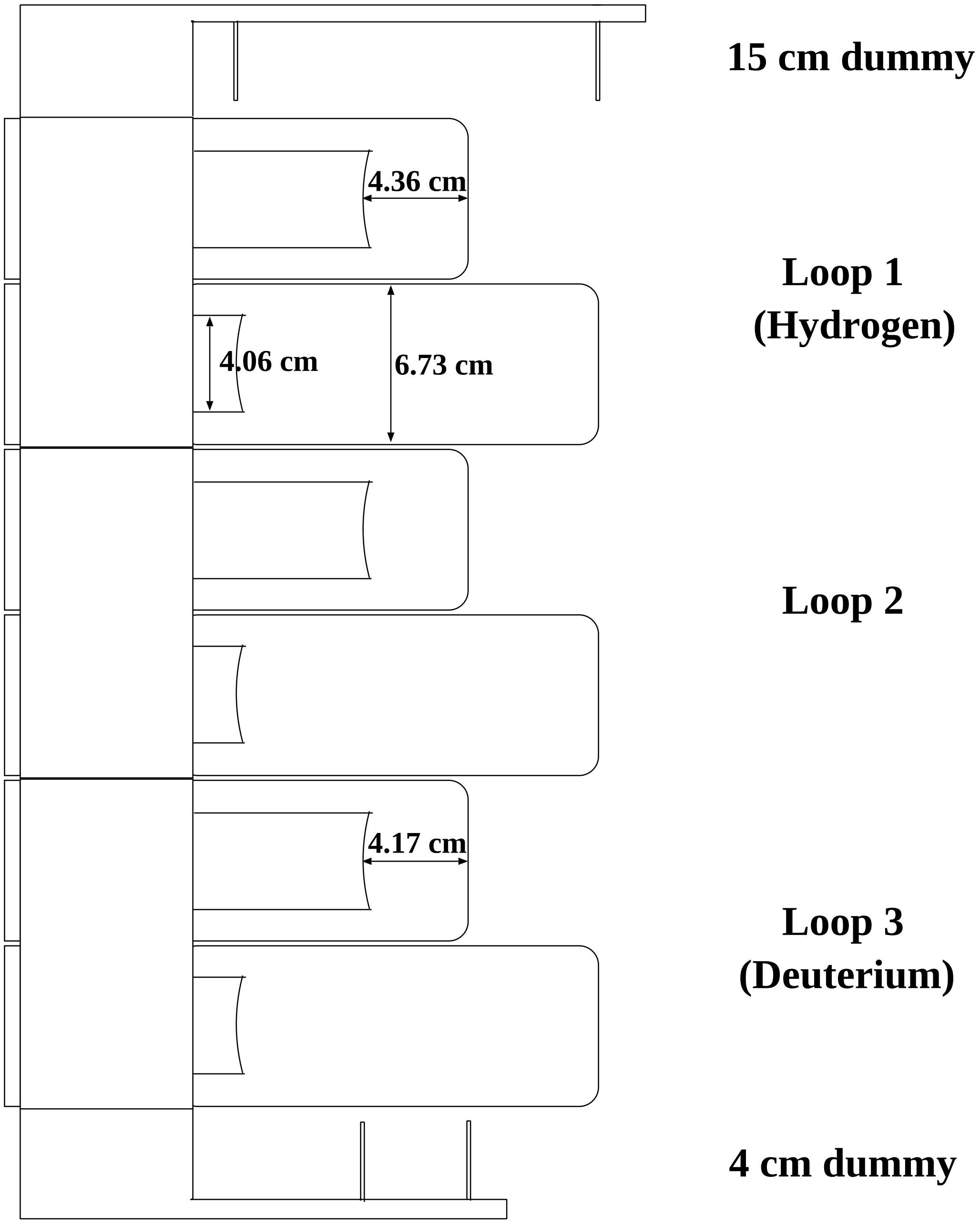

Figure 2.3: Hall C Crytotarget

22 K and 20 psi. Since density of the target material is a function of temperature, the temperature was kept constant by two pairs of heaters, a fast high power heater that matched the heatload of the beam when it was on or off, and a low power heater that adjusted for slow variations in the cooling system. Target temperature was kept stable to 0.1% for the majority of the experiment. Local density fluctuations due to the electron beam were minimized by the rastering of the beam. To calculate the contribution of the walls of the beer cans to the data, empty targets with aluminum walls ten times thicker than those of the cryotargets were included in the target stack. The empty target walls were thicker than the cryotarget walls in order to increase the statistics in empty target runs. Switching from one target to another was done from the counting house, and the temperature and pressure of the targets were continuously monitored.

2.4 Spectrometers

Two magnetic spectrometers were used in this coincidence experiment. Scattered electrons (and pions) were detected in the High Momentum Spectrometer (HMS), and scattered kaons (and pions and protons) were detected in the Short Orbit Spectrometer (SOS) (see Fig. 2.4). Both spectrometers were designed for moderate energy and angular resolution. Both were created to have a large angular acceptance (~7 msr), with the HMS having a moderate momentum acceptance (~16%) and the SOS having a large momentum acceptance (~40%). The HMS is capable of detecting particles with energies up to 7.5 GeV with a long TOF lever arm from target to detector hut (~25 m). The SOS has a momentum cutoff at about 1.8 GeV, and its short length (distance to the last hodoscope plane ~10 m) enables the more efficient detection of decaying particles such as kaons and pions. The HMS has four superconducting magnets, three focussing quadrupoles followed by a momentum-analyzing dipole with a central bend angle of 25 degrees. The SOS has three normal magnets, a horizontally focussing quadrupole followed by two dipole magnets, the first with a central bend of +33 degrees, the second with a central bend of -15 degrees. Both dipoles are in the same yoke, decreasing the optical length of the spectrometer, but the odd shape of the magnets (especially the second dipole) causes the field map to be highly dependent on the fringe fields. Both spectrometers are calibrated for point-to-point tunes, which means that scattering from a point target would be focussed to a point at the focal plane of the spectrometer. Octagonal collimators (tungsten alloy with 10% CuNi, thickness 6.35 cm) are placed before the entrances of the spectrometers in order to better define the solid angle acceptances (see Fig. 2.5). These collimators can be replaced by a set of sieve slits for optics studies. A complete SOS reference manual can be found in [Cum96].

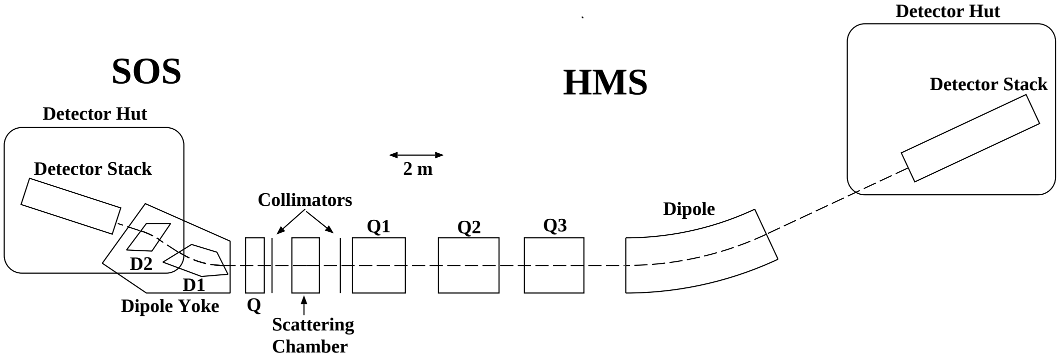

Figure 2.4: Hall C Spectrometers

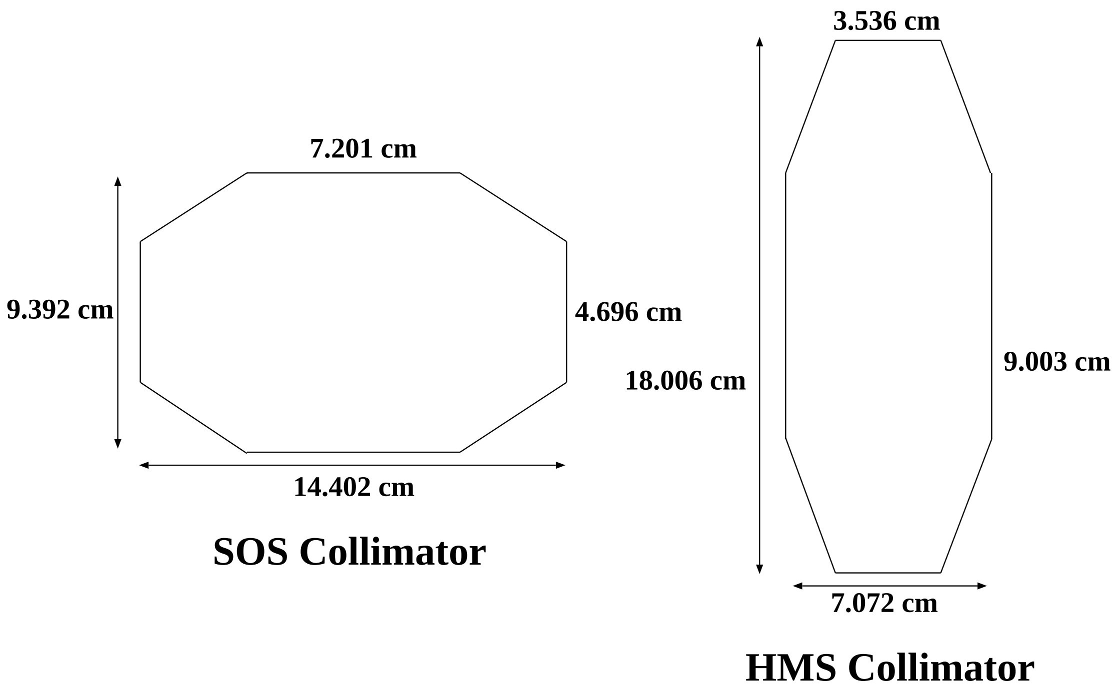

Figure 2.5: HMS and SOS Collimators

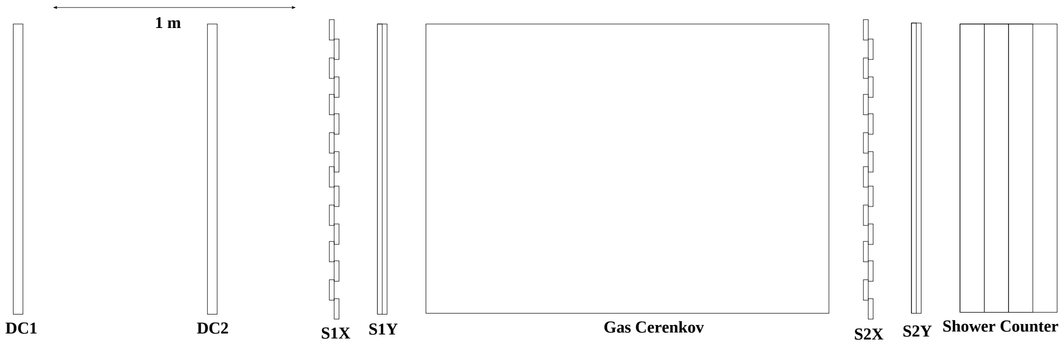

Figure 2.6: HMS Detector Hut

2.5 Detector Huts

The detector packages at the end of the two spectrometers are quite similar (see Figs. 2.6 and 2.7). Two drift chambers are followed by a Čerenkov detector sandwiched by two pairs of hodoscope planes. In the rear sits a shower counter. In the SOS there is an aerogel Čerenkov detector in between the final two hodoscope planes.

2.5.1 Drift Chambers

The drift chambers come first in order to minimize multiple scattering effects, because these chambers define the particle track that we reconstruct to the target in order to know its momentum, initial angles, and initial position. Each drift chamber has six wire planes with multiple orientations in the plane transverse to the optical axis (see Fig. 2.8). Each wire plane has a set of anode wires at ground and a set of potential wires and cathode foils at negative high voltage. The drift

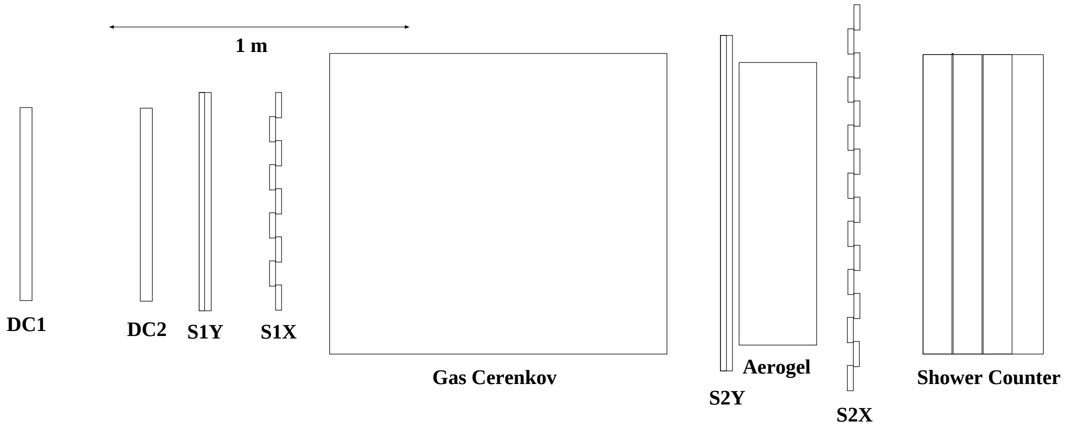

Figure 2.7: SOS Detector Hut

chambers are filled with a 50-50 argon-ethane mixture. A charged particle that passes though a wire plane will ionize a large number of the gas molecules, and the freed electrons will be accelerated towards the nearest anode wire. The wires are separated by 1 cm, so the largest drift distance will be 0.5 cm. The drift distance can be extrapolated from the drift time. Multiple planes with the same orientation offset 0.5 cm from each other are used to eliminate left-right ambiguities. The focal plane of the spectrometer lies near the two drift planes, so that it is a short extrapolation from the drift chamber tracks to focal plane quantities that can be reconstructed into target quantities. The charge collected on each wire is amplified and discriminated at the drift chamber. Drift chamber information is collected by a fastbus Time-to-Digital Converter (TDC) on the spectrometer carriage, and is read out only after a trigger is received from the counting house. For each trigger the previous 4 μs of wire numbers and TDC drift times are collected.

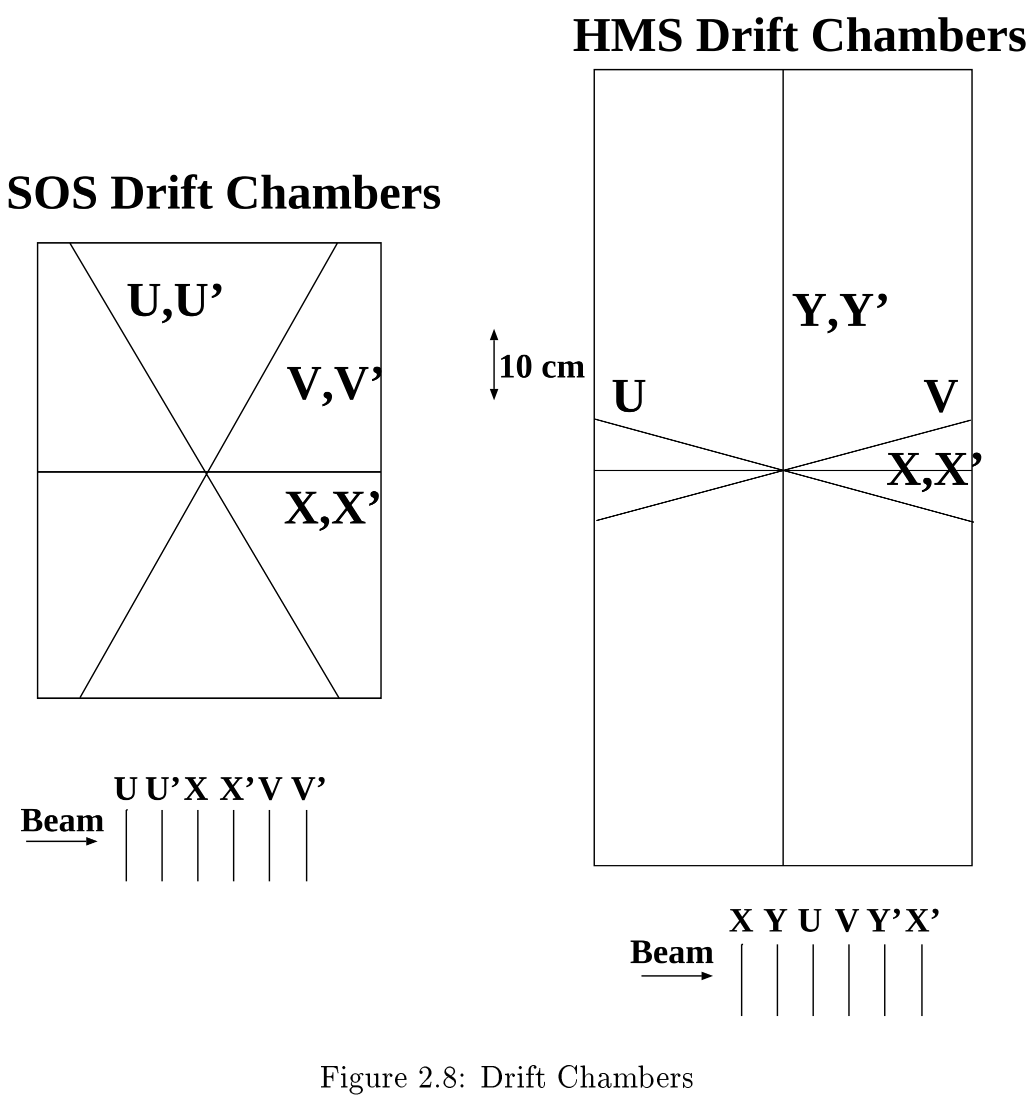

Figure 2.8: Drift Chambers

2.5.2 Hodoscopes

The two sets of hodoscope planes are separated by approximately 2 m. This spacing creates a long lever arm that can be used for time-of-flight (TOF) calculations. The hodoscope planes are a set of light-tight plastic scintillators 1 cm thick. One plane in each pair has the scintillators oriented along the y-axis in order to get an x position measurement, while the other has scintillators oriented along the x-axis to determine a y position. These positions are used to ensure that the hodoscope hits correspond to the chosen focal plane track. The position extrapolated from the track along the length of the scintillator plane is used to make path length corrections that correspond to the time it takes light to propagate to the photomultiplier tubes (PMT) on either end of the scintillator. The scintillators have a 0.5 cm overlap to maximize efficiency. Pulse height corrections can be calibrated for electrons, pions, or protons. The HMS has 32 scintillators 8 cm wide in each x-plane and 20 scintillators 8 cm wide in each y-plane. The SOS has 9 scintillators 4.5 cm wide in each y-plane and 9 scintillators in the front x-plane and 16 scintillators in the back x-plane 7.5 cm wide. Hodoscope information is included in the electronics trigger, and times relative to the trigger as well as the size of the signal are recorded for every scintillator hit.

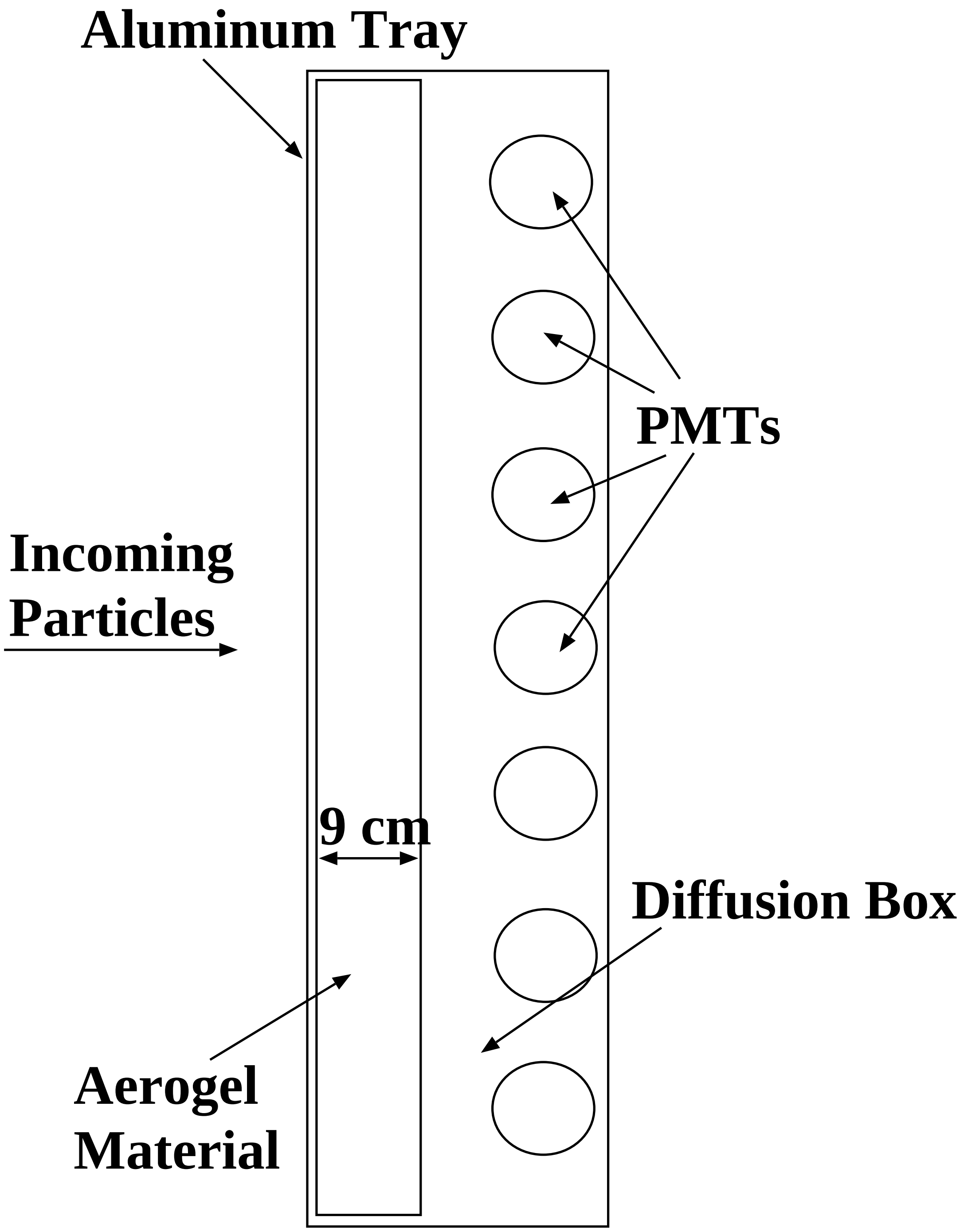

Figure 2.9: SOS Aerogel Čerenkov

2.5.3 Čerenkovs

Čerenkov detectors are used to measure particle velocity thresholds. In a given medium with index of refraction n greater than that of air, Čerenkov light will be radiated at a fixed angle if the velocity of the particle in that medium divided by the speed-of-light is greater than one. In a traditional gas Čerenkov, this light is reflected from mirrors into PMTs that create an electrical signal proportional to the number of initial Čerenkov photons. Our gas Čerenkov in the HMS is 152 cm long, with two mirrors tilted in the vertical direction focussing light into two PMTs. In an aerogel Čerenkov, the aerogel material is surrounded by diffuse reflecting walls, such that the Čerenkov photons reflect off the walls several times before reaching PMTs at either end of the aerogel material (see Fig. 2.9). The aerogel Čerenkov in the SOS has an active area of 0.98 m by 0.39 m with a thickness of 0.09 m. There are seven PMTs at each end of the aerogel material. Gas Čerenkovs are ideal for distinguishing between electrons and hadrons, since the index of refraction can be so close to one that only electrons will have a high enough velocity at the momentum setting of the spectrometer to produce Čerenkov photons. Pions and electrons can be separated using the gas Čerenkov in the HMS. The trigger can be set to require Čerenkov photons above a minimum threshold if one wants to eliminate pions. Aerogel Čerenkovs can be constructed with much higher indices of refraction to allow one to distinguish pions from kaons. The index of refraction in the SOS aerogel Čerenkov (1.034±0.001) is chosen such that pions and positrons would create Čerenkov photons, but kaons and protons would not. The trigger can be set to require that the Čerenkov be below a minimum threshold in order to reject pions and increase the kaon/pion event ratio. The signals from the fourteen PMTs are summed to form two combined signals, A and B. The trigger will not be supressed if either A or B is less than the threshold, which for our experiment corresponds to six photoelectrons. The SOS gas Čerenkov was not used since there was no need to distinguish between pions and positrons.

2.5.4 Shower Counters

The shower counters are a set of four stacks of lead glass blocks 10 cm x 10 cm x 70 cm. High energy electrons traveling through the dense material radiate bremstrahlung photons that in turn create e^+e^- pairs if they are energetic enough. An electromagnetic shower is created, and in the end the Čerenkov photons from the electrons in the shower can be collected and correlated with the total amount of energy deposited in the block. An electron will deposit almost all its energy into the shower counter, whereas a pion will deposit only a small fraction of its energy. The shower counter is therefore best used to help distinguish between pions and electrons, and is useful in our experiment in the HMS. Since electrons will deposit most of their energy in the first two planes of blocks in the shower counter, the energy deposited in these two planes can be looked at as a sort of pre-radiator. Energy deposited in both the preshower and the shower counter can be used as part of the trigger.

2.6 Trigger

Output from the hodoscopes, shower counters, and Čerenkov detectors travel up from the experimental hall to the counting house in order to be processed and utilized in the trigger. The input of the detectors is always split immediately and sent to an Analog-to-Digital Converter (ADC). The remaining signal is discriminated, with the output going to TDCs and VME scalers. The shower counter output is sent through three separate NIM discriminators, with the preshower input being sent through two discriminators and becoming PRLO and PRHI signals, and the shower input being discriminated and transformed into a SHLO signal. The HMS gas Čerenkov input is sent through a NIM discriminator and produces either a Čerenkov (C) or a Čerenkov-veto ($\overline{\mathrm{C}}$) signal. The SOS aerogel Čerenkov input is split into two sums of signals that are discriminated separately. Both sums have to be above the discriminator threshold in order for the Čerenkov-veto ($\overline{\mathrm{A}}$) signal to be created. The hodoscope inputs are discriminated and then sent to logic modules that create the (SOS) signals S1X (S1X+ AND S1X-), S1Y, S2X, S2Y, S1 (S1X

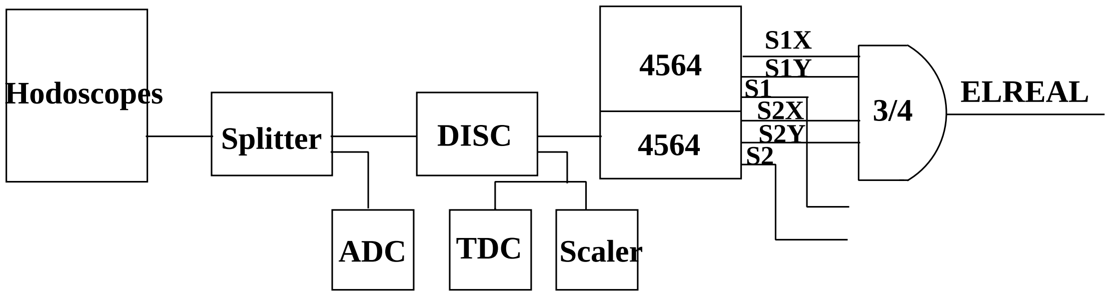

Figure 2.10: HMS Trigger

OR S1Y), and S2. The basic trigger is created by 3/4 of S1X, S1Y, S2X, and S2Y (SCIN). A weaker variant of this signal is S1 AND S2 (STOF). There are two electron triggers that can be created: (2/3 of SCIN, STOF, and PRLO) AND C (ELLO) or 3/3 of SCIN, SHLO, and PRLO (ELHI). ELREAL is created by ELLO OR ELHI. A non-electron trigger PION is formed by SCIN AND $\overline{\mathrm{C}}$. This signal can be prescaled to form PIPRE. A pretrigger is formed by ELREAL OR PIPRE.

The actual trigger that was used during most of the experiment when we were detecting electrons in the HMS and kaons in the SOS only used scintillator and aerogel information. The PION trigger in both the HMS and SOS was simply a prescaled SCIN signal. In the HMS ELREAL was equivalent to SCIN, and in the SOS was equivalent to SCIN AND $\overline{\mathrm{A}}$ (see Figs. 2.10 and 2.11). These signals went into the 8LM logic module, along with pedestal pretriggers and Trigger Supervisor (TS) Go (run has started), EN1 (run has started, data taking enabled), and BUSY (run has started, data taking disabled). The 8LM produces the PRETRIG and

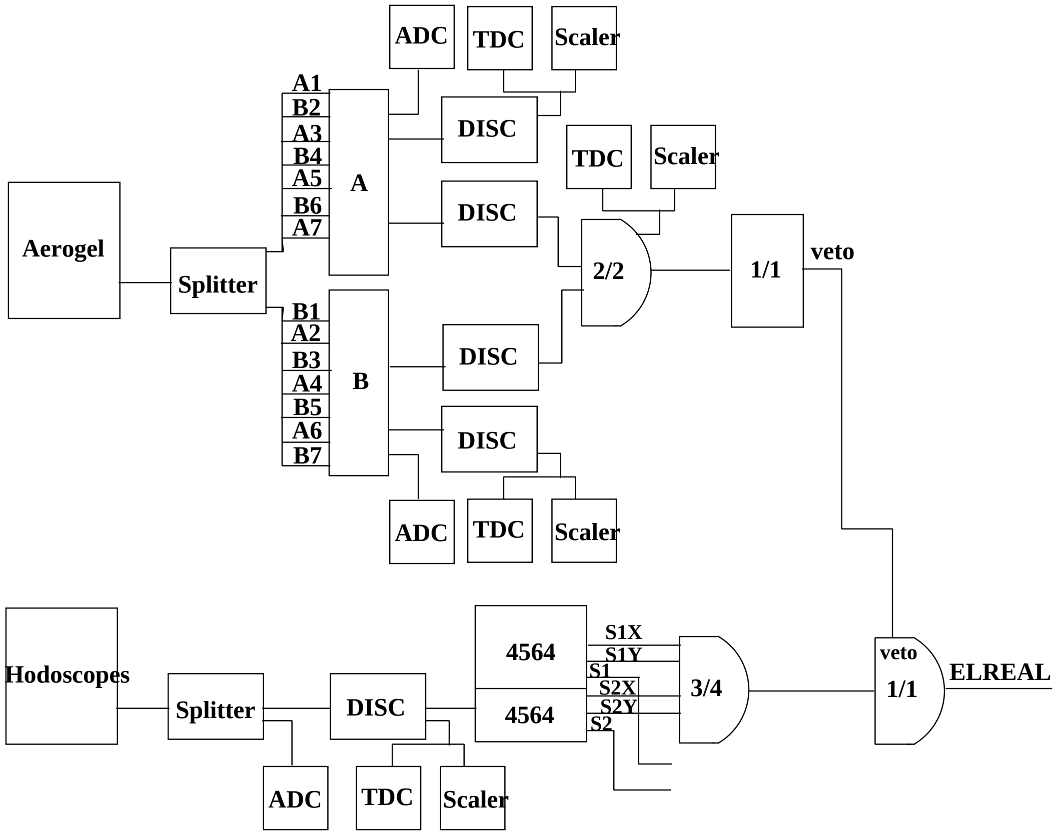

Figure 2.11: SOS Trigger

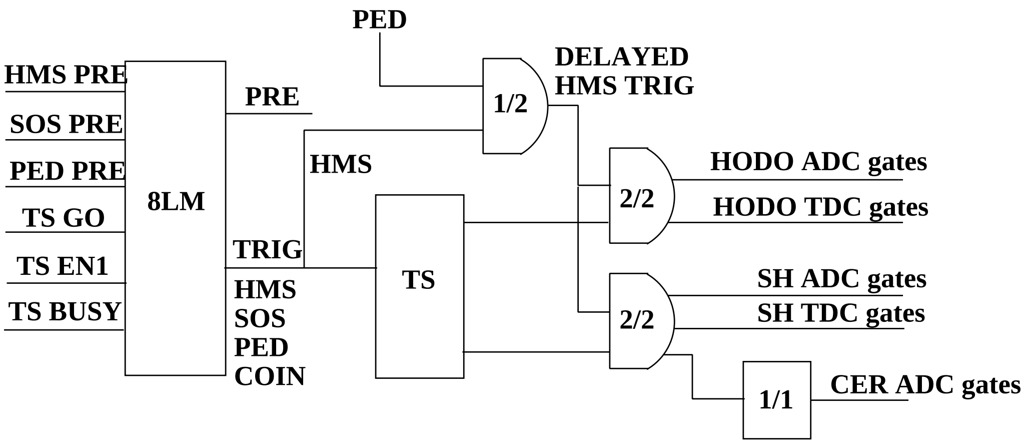

Figure 2.12: Trigger Logic

TRIG signals for HMS, SOS, COIN, and PED. Pedestals are taken only at the beginning of a run for the first 1000 events, so the PED PRETRIG is PED AND GO AND $\overline{\text{EN1}}$. The other PRETRIGs are HMS AND EN1, SOS AND EN1, and HMS AND SOS AND EN1. The TRIGs are the PRETRIGs anded with $\overline{\text{BUSY}}$. These TRIGs go into the TS, and are combined later with a delayed HMS TRIG in order to set the precise timing for the ADC and TDC gates for the hodoscopes, shower counters, and Čerenkovs (see Fig. 2.12). To measure coinicidence timing signals from one spectrometer are used as stops to TDCs started by the other spectrometer.

2.7 CODA

The conversion from a collection of electronic signals to a physics event written to disk is managed by the CEBAF On-line Data Acquisition (CODA) system [Abb95]. Information for each event is temporarily stored in fastbus TDCs and ADCs, and scaler information waits in VME crates. All of these front-end crates are managed by Read Out Controller (ROC) processors. The signal for a valid trigger is sent to the ROCs from the TS, which then read the event data and send event fragments along the Event Builder (EB). The EB checks that the fragments are in good condition, and checks the synchronization of the data stream if running in buffered mode where fragments for 1000 events are read at a time rather than building one event after another. If synchronization has been lost over the past 1000 events, the EB resets the synchronization. The EB then sends the combined fragments for each event on to the Event Recorder, which organizes each event into a standard format and writes it to disk. A fast FDDI network interface connects the various CODA components, and the user controls data acquisition through a GUI interface. During E91–016, integrated event rates ranged up to 1 KHz, corresponding to a data rate on the order of 1 Mbyte/s.

2.8 Experimental Goals

The experimental settings for E91–016 are listed in Table 2.1. Data were obtained on hydrogen and deuterium targets at all settings. Cross sections to be extracted are those for p(e,e$'$K$^+$)Λ, p(e,e$'$K$^+$)Σ^0, d(e,e$'$K$^+$)Λn, and d(e,e$'$K$^+$)Σ. Effects of nuclear transparency and final-state interactions can be investigated by comparing Λ cross sections on hydrogen and deuterium. A cross section for n$_{bound}$(e,e$'$K$^+$)Σ^- can be calculated by subtracting from the combined Σ cross section on deuterium the contribution from Σ^0 as determined from hydrogen data taken at the same setting. Experiment E91-016 took data at Jefferson Lab in Hall C over a series of time periods between August and November 1996. Measurements were made

Table 2.1: List of experimental settings.

E_{beam} GeV	$\theta_{\rm HMS}$ deg	$P_{\rm HMS}$ GeV	$\theta_{\rm SOS}$ deg	$P_{\rm SOS}$ GeV	W GeV	Q^2 GeV^2	setting
3.245	17.19	1.723	17.67	1.077	1.80	0.50	0
3.245	17.19	1.723	22.00	1.077	1.80	0.50	4
3.245	17.19	1.723	26.50	1.077	1.80	0.50	8
3.245	17.19	1.723	30.96	1.077	1.80	0.50	13
3.245	17.19	1.723	17.67	0.929	1.76	0.52	0l
3.245	17.19	1.723	21.94	0.929	1.76	0.52	4l
3.245	17.19	1.723	26.45	0.929	1.76	0.52	8l
3.245	17.19	1.723	31.00	0.929	1.76	0.52	13l
3.245	15.48	1.593	15.45	1.240	1.90	0.38	1
3.245	15.48	1.593	19.92	1.240	1.90	0.38	6
3.245	15.48	1.593	25.00	1.240	1.90	0.38	11
2.445	24.60	0.847	13.42	1.150	1.90	0.38	23
2.445	27.25	0.918	15.48	1.077	1.80	0.50	25
2.445	27.25	0.918	15.48	0.929	1.76	0.52	29

at two different values of Q^2. At the higher Q^2 point, data were taken at two different settings of the SOS central momentum, leading to a set of data with slightly different average Q^2 and W. Data were taken with the SOS at multiple angular positions, from as close as possible to parallel kinematics out to around 50 degrees in the center-of-mass, so that angular dependences can be measured. Data were taken at a lower beam energy to provide points at different values of the virtual-photon polarization ϵ.

Chapter 3

Data Analysis

3.1 Analysis Overview

The procedure for analyzing the raw data and extracting results from the data is discussed in Chapters 3 and 4. First, raw data is converted by the replay software package (referred to as the "engine") into a processed array of target and focal-plane quantities (ntuples) with associated files of scalar information. Next, cuts are applied to the data to eliminate all events that do not have an electron in the HMS and a kaon in the SOS within the missing-mass range of interest, and the relative numbers of real coincidences, random coincidences, and events originating from the target walls are quantified. Normalizations and efficiencies (including efficiencies of the applied cuts) are measured along with estimates of their errors. Finally, the data is compared directly with a sophisticated Monte Carlo simulation that includes decay, radiative corrections, transport through the spectrometers, spectrometer acceptances, and physics weights. From this comparison cross sections can be extracted from the data.

3.2 Replay Engine

The input to the replay engine is a raw set of ADC, TDC, and scalar values from all the detectors in the HMS and SOS huts for each event. The job of the replay engine is to convert these values into information describing the exact character of the particles these data are describing, determining along the way which parts of the data should be kept and which rejected. The engine is focussed on reconstructing the most likely particle track for a given event. The most likely track is generally the one with the lowest chi-squared from the track reconstruction algorithm, and has good scintillator hits along the track from which a velocity divided by the speed-of-light (β) can be calculated. The engine processes raw signals from all of the detector elements into output quantities (such as number of photoelectrons in a Čerenkov detector) that are easily understood (and used for software cuts) by the user in the form of a PAW [Cer95] ntuple. Scalar information is converted into large scalar files that include data concerning hits on individual scintillator planes and efficiencies of detectors. Information from beamline elements such as BCMs, BPMs, and raster positions are included for each event, such that the exact position of the beam on the target can be known (to within an overall offset), and the total integrated charge up to that event can be determined. Scalar quantities from which overall efficiencies can be calculated are also included.

3.2.1 Tracking

The tracking algorithm used by the replay engine is straightforward to describe. In each chamber, a series of space points are chosen based on the wire hits in each of the six planes. Left-right ambiguities (on which side of a wire did a particle pass) are resolved using offsets in parallel sets of planes. Space points in the two chambers are then linked to each other by tracks. The track that has the lowest chi-squared and best connects to hits in other detector elements is chosen as the true track. It is possible to have more than one track for a given event because of more than one particle passing through the detector hut at the same time. It is also possible for no tracks to be found for a given event, since drift chamber information is not involved in the hardware trigger. In a given chamber, wires in five out of six planes must fire in order for space points to be determined. The best reference for the replay engine tracking algorithm is [Van98].

3.2.2 Focal Plane to Target Reconstruction

COSY

Once an event track has been determined, the position of the particle in the spectrometer focal plane can be calculated. Knowledge of the optical properties of the spectrometer allows us to calculate the initial momentum and direction of the particle at the target. The original formulation for particle propagation using TRANSPORT involves a Taylor expansion of the equations of motion for a charged particle in static magnetic fields to second order around the central path trajectory [Bro82]. The only assumption made is that the magnetic field elements have midplane symmetry, such that the magnetic potential is an odd function of the coordinate transverse to the midplane. The transformation between focal-plane quantities x, x', y, y' (labeled as xfp, xpfp, yfp, ypfp, the prime indicates a derivative with respect to the longitudinal coordinate z) and target quantities delta (momentum), x'_{tar}, y'_{tar}, y_{tar} (labeled as delta, xptar, yptar, ytar) can be described by a matrix R_{ij}, where numerous matrix elements are required to be zero to allow for midplane symmetry. Further restrictions on the matrix elements can be made by requiring a point-to-point focus, such that the position of the particle in the focal plane is independent of its initial angle. The current method we use for transport, COSY INFINITY, is an improvement of this technique using differential algebra [Ber90a]. This code allows the creation of Taylor maps for arbitrarily complicated magnetic fields to arbitrary order [Ber90b]. In obtaining the initial set of matrix elements describing the path through the spectrometer, an accurate description of the drift distances and magnetic components is required. For the HMS, simple models for the superconducting quadrupoles and dipole are used. For the SOS, a field mapping of the magnets is used by COSY. The Monte Carlo simulation described below uses the output of COSY to transport the particle from the target to the focal plane and back again to the target.

Reconstruction Matrix Elements

To optimize the data reconstruction the COSY matrix has to be adjusted from the theoretical prediction. Data taken with a sieve slit between the target and spectrometer are used to better match the reconstructed angles with the true angles. The procedure is outlined in [Ass97]. After COSY is used to get an initial set of matrix elements, the data are mapped to the sieve slit, and the hole closest to each particle is determined, fixing the true angle. Comparing reconstructed to true angle event by event is used to obtain an optimized design matrix using the singular value decomposition method. The design matrix multiplies a function of the focal plane coordinates in order to reproduce the optimized target values, and solving for this matrix is generally an overdetermined problem. New reconstruction matrix elements are generated using Gaussian backward substitutions. The process is then repeated, hopefully leading to a convergent optimization. As in the theoretical method described above, certain matrix elements are not permitted to vary in order to maintain midplane symmetry and point-to-point focus properties. Optimization for momentum reconstruction and target position also took place using slanted target runs and extended target delta scan runs. Reconstruction matrix elements for both the SOS and the HMS were generated in this manner based on data taken during experiments E91–016 and E93–018. These matrix elements are the ones used in the replay engine.

3.2.3 Time of Flight

The determination of the velocity of the particle uses the time it takes the particle to travel the several-meter distance from the first to the last scintillator plane. Random scintillator hits (and times) are eliminated by requiring the scintillator paddle hit to be on the track, with allowance for slop due to resolution issues and multiple scattering. The slop size used is an extra half of a scintillator paddle in the S1 planes, and a whole extra paddle in the S2 planes. Pulse-height corrections are made to the hit time, since different particles evoke different scintillator responses depending on whether they are minimum ionizing or not. Also, the time it takes light to travel from the interaction point to the positive and negative ends of the scintillator paddle is factored in. The timing parameters and offsets are calibrated using a high statistics data sample of a known particle (so the correct beta is known beforehand).

During E91–016 there was a problem with the TDC that was in charge of the S2X data from the SOS. Approximately one-tenth of these TDC values were flawed in one of two systematic ways: the corresponding times were offset by a discrete amount (around 3–6 ns), or the times were offset in a manner describing a continuous tail (see Fig. 3.1). There were variations between groups of runs: sometimes the positive and negative times would be offset by the same amount, sometimes one of the times would be correct while the other would have an offset. This flakiness manifested itself in the beta spectra of our particles, as shadows and tails would be seen in any two-dimensional plot of beta versus delta or coincidence time. The claim that the problem was a hardware one was verified when the TDC was replaced during E93–018 and the problem disappeared (Fig. 3.1, run 11989). The problem reappeared in a different manner after run 11990 when lightning caused a power outage in the electronics room (Fig. 3.1, run 12010).

Since beta is an important quantity for the particle identification cuts, it was necessary to create a software algorithm to deal with this flakiness. Upper and lower limits were placed on the raw scintillator times. These limits did not cut any particle accepted in the spectrometer, but acted as a cutoff for particle times

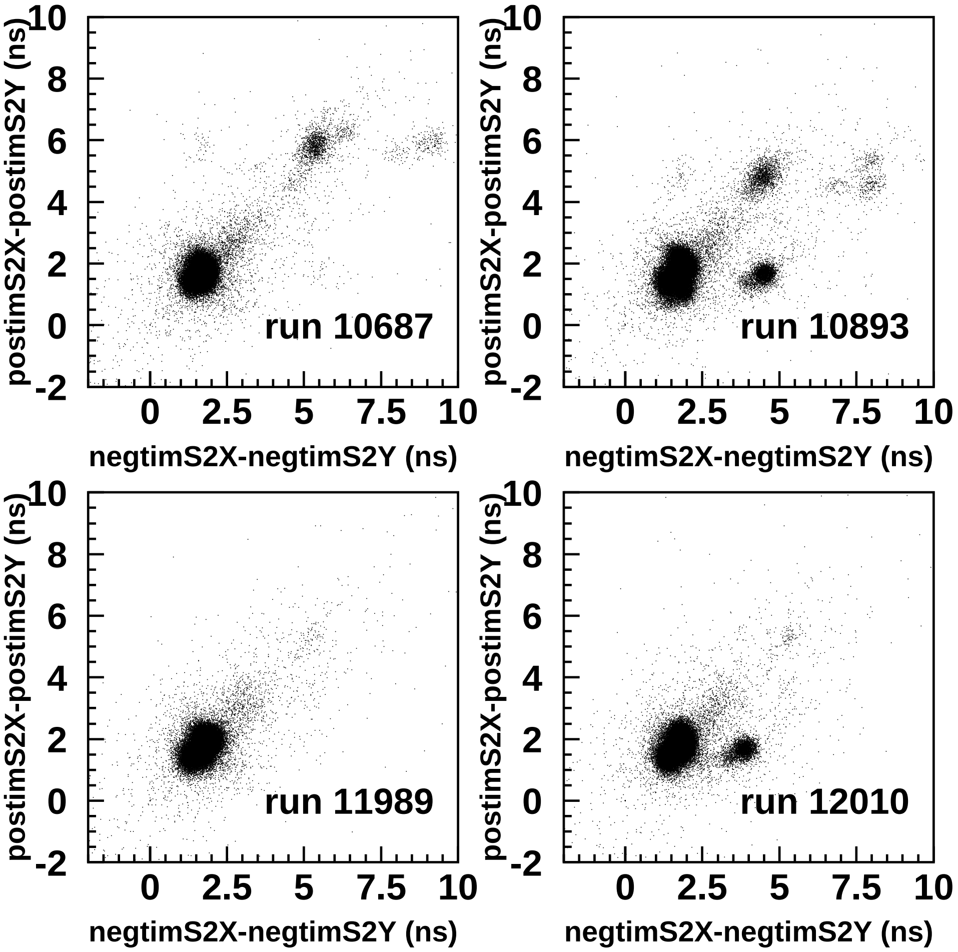

Figure 3.1: Scintillator time differences between SOS planes S2X and S2Y for four different runs. No particle ID cuts have been placed on the data: there are only loose cuts on SOS delta, beta, and coincidence time. The S2X TDC was replaced before run 11393 during experiment E93–018. Additional E91–016 data was taken from runs 11921–12017. A lightning strike during run 11990 led to a reoccurrence of S2X TDC problems that can be seen in the plot corresponding to run 12010.

that were too slow due to the TDC adding extra time. Also, cuts were put on the time difference between the S2Y and S2X planes, since this difference is almost independent of particle type due to the short distance between them, and cuts on the shadows and tails can be made with a high degree of certainty. Positive and negative scintillator times were separately investigated, and any time that did not pass the cuts was thrown out. In this manner, the shadows and tails were significantly reduced without increasing the number of particles that did not have enough timing information to calculate a beta.

3.3 Raw Data

3.3.1 Randoms

Electron beam bunches are separated from one another by 2.004 ns. As can be seen in Fig. 3.2, this bunch separation leads to a series of peaks in coincidence time that are separated by 2.004 ns. Since the coincidence time calculation is calibrated for kaons, there is no beta dependence in the coincidence time peaks for kaons. Real coincident kaons can be seen at 0 ns. There are also a series of random peaks made up of coincidences between uncorrelated electrons and kaons. Random coincidences can occur within the same coincidence time window as the real coincidences, and this random contribution needs to be subtracted from the

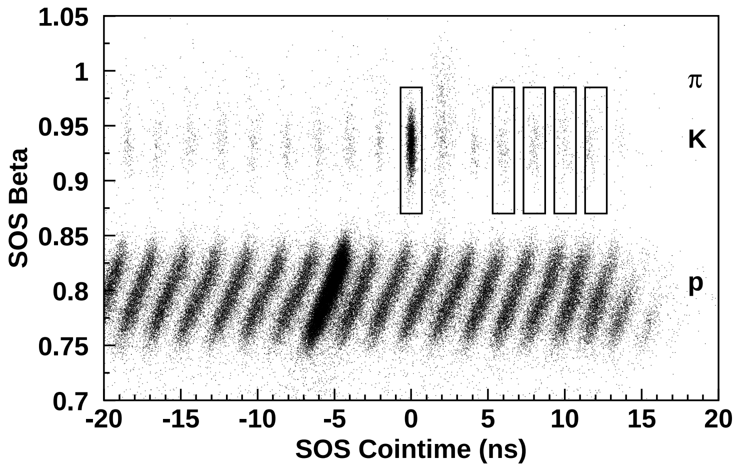

Figure 3.2: Real and random cuts in coincidence time. Data have a tight missing-mass cut around the Λ peak and an aerogel cut to eliminate most of the pions.

true yield. To do this subtraction the average number of random counts over a series of random peaks is calculated. Minimizing the contribution from real pions and real protons requires avoiding using random peaks near in coincidence time to these real peaks.

The average of four random peaks as seen in Fig. 3.2 are used to calculate the random contribution. Using different sets of random peaks led to variations in random counts on the order of 2%, which is less than the statistical error, so only the statistical error is used when subtracting from the reals. Random events are approximately 1.5% of the total number of events in a tight window around the Λ peak for hydrogen (6.5% of the total integrated from 1.10–1.22 GeV for hydrogen). For deuterium, the random contribution is on the order of 15% of the total yield. Random subtractions need to be performed when measuring cut efficiencies as described below. Since the cut efficiencies should be the same for hydrogen and deuterium, the uncertainty due to low random statistics can be minimized by performing the random subtraction in a narrow region around the Λ peak in hydrogen, and using the same random-subtracted cut efficiencies for hydrogen and deuterium at the same setting.

3.3.2 Empty ("Dummy") Target

At one end of the cryogenic target stack there are two aluminum walls approximately 4 cm apart (referred to as the dummy target) that are used to study the contribution of the aluminum walls in the target cells to the data. The total thickness of the dummy target walls is around ten times thicker than that of the hydrogen and deuterium cells, so that the same statistics can be generated in one-tenth the running time. Dummy target runs are normalized to the liquid target runs by total charge and total aluminum thickness. The dummy contribution, with a random dummy subtraction, is subtracted from the data. The error in the subtraction is only statistical since the dummy statistics are generally quite few. The contribution of the dummy target to the real peak is less than the contribution from randoms. In Fig. 3.3 the relative strengths of reals, randoms, dummy, and dummy randoms can be seen. At this setting the ratio of dummy to random is 0.5

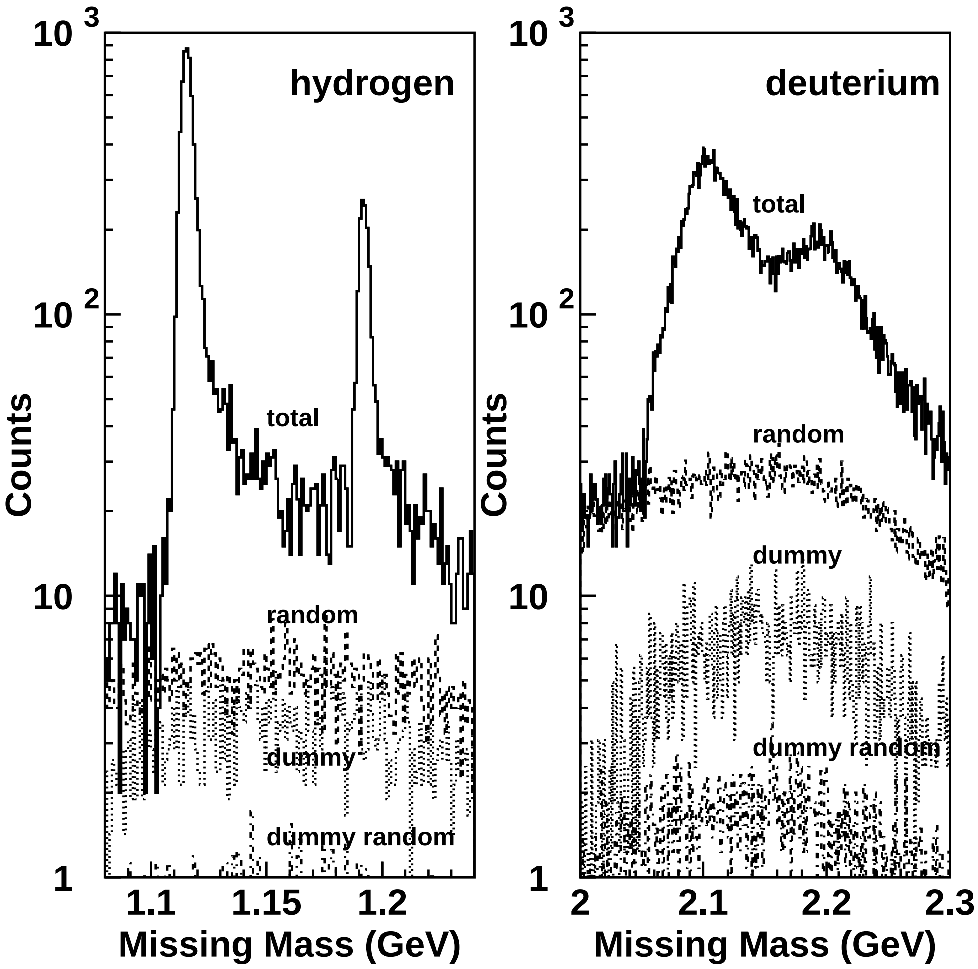

Figure 3.3: Random and dummy subtraction on hydrogen and deuterium. Curves represent raw yield, random contribution, dummy contribution, and dummy randoms. The relative contributions in hydrogen and deuterium can be seen in this side-by-side comparison. Note the logarithmic vertical axis.

for hydrogen and 0.2 for deuterium. The quality of the subtraction can be seen by looking at the elimination of the excess counts below threshold.

3.4 Efficiencies/Normalizations

3.4.1 Tracking Efficiency

As mentioned above, wire chamber information is not a part of the trigger, so having a good trigger is no guarantee that there is any good tracking information. The methodology and most complete statistical data on the tracking efficiency calculation can be found in [Van98]. The basic concept is to measure an efficiency for tracks that appear to pass through the center of the spectrometer as determined by the scintillator hits. A central set of paddles is chosen in each plane to correspond to the "sweet spot". If four out of four scintillator planes have hits, and all the hits are in the sweet spot, then this event is considered to have traveled through the center of the spectrometer. The tracking efficiency is calculated by dividing into this number the number of these events that have good tracks. This ratio is referred to as the fiducial tracking efficiency, and is generally on the order of 90%. This method has not been tested directly for kaons due to low statistics and particle ID issues. Also, there is no straightforward way of measuring the tracking efficiency outside of the sweet spot, as it becomes complicated to determine whether a track that went through a random set of hodoscope planes would have passed through the active area of the drift chambers. The error in fiducial tracking efficiencies in both spectrometers has been assigned as $\pm 1.5\%$.

3.4.2 Hodoscope Efficiency

The inefficiency of any given hodoscope paddle is on the order of 1%. This is measured by comparing how many events have hits in three out of four scintillator planes as opposed to four out of four. The probability that for a given event more than one scintillator plane will not record a particle passing through it is quite small. Even taking into account the problems with the SOS S2X TDC, the total three out of four efficiency (equivalent to the trigger efficiency) for both spectrometers is effectively 100%, with an error of less than 0.1%.

3.4.3 Electronic Dead Time

The windows for the logic modules were set to 30 ns. If signals for two events arrived at the module within that time, the second event was not processed. The number of triggers lost due to this timing window was measured by comparing the number of triggers when using 30 ns, 60 ns, and 120 ns windows. The number of triggers lost in 30 ns was defined to be the difference in the number of triggers between 120 ns and 60 ns divided by 2. This difference was divided by the number of triggers using the 30 ns window to obtain an electronic dead time. Electronic dead times for each spectrometer were typically less than 1%.

3.4.4 Coincidence Blocking

A random single event which arrives at the trigger supervisor just before a coincidence event can lead to a mistiming in the coincidence time logic. This mistiming causes the coincidence time for that event to be offset by a significant amount, consequently falling outside of any coincidence time cuts. The amount of coincidence blocking is dependent on the random event rate, and is therefore higher for deuterium than for hydrogen. The average percentage of good events lost due to coincidence blocking is 2.8% for hydrogen and 3.8% for deuterium, with uncertainties on both numbers of 0.5%.

3.4.5 Computer Dead Time

An event can be recorded only if the trigger electronics are not already busy with another event. The time it takes the trigger to process an event is approximately 400 μs, which corresponds to an event rate of 2.5 kHz. In general, the data rates during E91–016 were limited to below 1 kHz, which still led to significant dead time. Computer live times can be calculated by taking the number of triggers (SOS, for example) AND EN1 AND $\overline{\text{BUSY}}$ and dividing by SOS AND EN1

(SOSTRIG/SOSPRE). The dead time is one minus the live time. The calculated dead times for the SOS, HMS, and COIN triggers are identical [Gee96]. Dead times are decreased by running data acquisition in buffered mode, which was the case during most of E91–016. In buffered mode events could be stored in a buffer while another event was being processed. The major concern in using buffered mode is the loss of synchronicity where some TDC readouts in one event are attached to a different event. Synchronicity was checked every thousand events and reset if necessary. Events lost due to sync errors are for most production running a small fraction of the total. Computer dead times are typically on the order of 10%.

3.4.6 Absorption

Absorption of electrons in the target and the HMS spectrometer is negligible. In contrast, kaons will interact significantly with the materials they pass through in the target and the SOS spectrometer. A list of all materials with their thicknesses, densities, and radiation lengths is given in Tables 3.1 and 3.2. The eikonal approximation of Weise [Wei89] gives the following formula for the kaon interaction cross section with matter,

$$\sigma = (A)(\sigma_{KN})(1 - \frac{3}{8}\frac{\sigma_{KN}}{\pi r_{02}}(1 - B^2)(A^{1/3})), \tag{3.1}$$

where A is the number of nucleons, σ_{KN} is the kaon-nucleon cross section, r_{02} is $(1.2\text{ fm})^2$, and B is the ratio of the real and imaginary parts of the forward kaon-

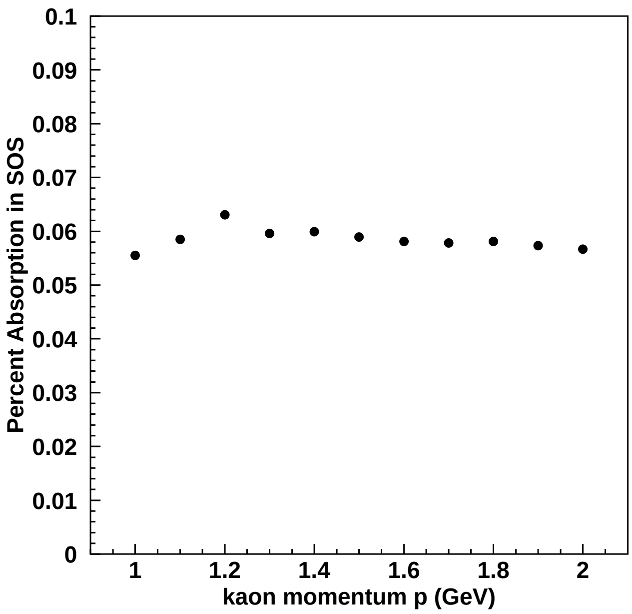

Figure 3.4: Kaon absorption in the SOS. From [Rei98].

nucleon scattering amplitude. Using kaon-proton cross sections from the Particle Data Group [Cas98] and kaon absorption data on carbon [Abr71], a parameterization for B as a function of momentum p is derived [Rei98] to be

$$B = 0.82119 - 0.11274p. \tag{3.2}$$

Kaon absorption data on copper [Abr71] is well-fitted through the use of this formula, validating the general use of the formula. Application to the SOS materials lead to kaon absorption ranging from 5–7%, with the explicit momentum dependence plotted in Fig. 3.4. A single value of absorption for each central value of SOS momentum is used to correct the data yield, and is assigned an error of 1%.

Table 3.1: Table of HMS materials. These table entries are used to calculate electron absorption (negligible) and multiple scattering. The numbers are used in the Monte Carlo simulation.

Material	t (cm)	rho (g/cm^3)	X_0 (g/cm^2)	r.l. (%)	Notes
		Target			
Entrance cap	0.0071	2.70	24.01	0.080	2.8 mil Al
LH2	4.36	0.0723	61.28	0.514	
LD2	4.17	0.1670	122.6	0.568	
Exit cap	0.0137	2.70	24.01	0.155	5 mil Al
Chamber exit	0.0406	2.70	24.01	0.457	16 mil Al
		Spectrometer			
Air	≈15	0.00121	36.66	≈0.050	
Kevlar entrance	0.0381	0.74	55.2	0.051	15 mil Kevlar
Mylar entrance	0.0127	1.39	39.95	0.044	5 mil Mylar
Kevlar exit	0.0381	0.74	55.2	0.051	15 mil Kevlar
Mylar exit	0.0127	1.39	39.95	0.044	5 mil Mylar
		Hut			
Air	≈35	0.00121	36.66	≈0.116	
DC Mylar	0.0102	1.39	39.95	0.036	
Ar/CH_4 gas	21.6	0.00154	≈25.7	≈0.129	
Sense Wires (W)	0.00006	19.3	6.76	0.017	12×25 μm wires
Field Wires (Cu/Be)	0.00212	≈3.5	≈25	≈0.030	12×125 μm wires
Air (to S2Y)	≈210	0.00121	36.66	≈0.693	
S1X	1.067	1.03	43.8	2.510	1.067 for overlap
S1Y	1.067	1.03	43.8	2.510	1.067 for overlap
CER entr (Al)	0.1	2.70	24.01	1.125	
CER gas (Freon)	≈150	0.0025	≈23.7	≈1.582	Density for .5 atm
CER mirror	-	-	-	≈0.5	Carbon/mylar
CER exit (Al)	0.1	2.70	24.01	1.125	
S2X	1.067	1.03	43.8	2.510	1.067 for overlap
S2Y	1.067	1.03	43.8	2.510	1.067 for overlap
Air	≈18	0.00121	36.66	≈0.060	
Calorimeter	40	-	-	≈1600	

Table 3.2: Table of SOS materials. These table entries are used to calculate kaon absorption and multiple scattering. The numbers are used in the Monte Carlo simulation.

Material	t (cm)	rho (g/cm^3)	X_0 (g/cm^2)	r.l. (%)	Notes
			Target		
Entrance cap	0.0071	2.70	24.01	0.080	2.8 mil Al
LH2	4.36	0.0723	61.28	0.514	
LD2	4.17	0.1670	122.6	0.568	
Exit cap	0.0137	2.70	24.01	0.155	5 mil Al
Chamber exit	0.0203	2.70	24.01	0.228	8 mil Al
			Spectrometer		
Air	≈15	0.00121	36.66	≈0.050	
Kevlar entrance	0.0127	0.74	55.2	0.017	5 mil Kevlar
Mylar entrance	0.0076	1.39	39.95	0.027	3 mil Mylar
Kevlar exit	0.0381	0.74	55.2	0.051	15 mil Kevlar
Mylar exit	0.0127	1.39	39.95	0.044	5 mil Kevlar
			Hut		
Air	≈15	0.00121	36.66	≈0.050	
DC Mylar	0.0178	1.39	39.95	0.062	14 planes
Ar/CH_4 gas	7.41	0.00154	≈25.7	≈0.044	
Sense Wires (W)	0.00008	19.3	6.76	0.022	12×30 μm wires
Field Wires (W)	0.00034	19.3	6.76	0.098	12×60 μm wires
Air (to S2X)	≈180	0.00121	36.66	≈0.594	
S1Y	1.098	1.03	43.8	2.582	1.098 for overlap
S1X	1.04	1.03	43.8	2.446	1.04 for overlap
CER entr	0.05	2.70	24.01	0.056	
CER gas (Freon)	≈100	0.0051	≈23.7	≈2.152	Density for 1 atm.
CER mirror	-	-	-	0.5	
CER exit	0.05	2.70	24.01	0.056	
S2Y	1.098	1.03	43.8	2.582	1.098 for overlap
AER entr	0.0625	2.70	24.01	0.70	
AER aerogel	9.0	-	-	≈6	
AER exit	0.0625	2.70	24.01	0.70	
S2X	1.04	1.03	43.8	2.446	1.04 for overlap
Air	≈20	0.00121	36.66	≈0.066	
Calorimeter	40	-	-	≈1600	

3.4.7 Total Charge

Beam current calibration runs were performed to calibrate the BCMs with respect to the Unser monitor. A series of discrete, fixed currents were measured and compared to the BCM response. A global set of data from current calibration runs taken throughout the experiment were used to generate a universal BCM normalization. The error in integrated BCM current is estimated to be 1.5%.

3.4.8 Target

Target Length

Precise length measurements were performed on the target cells at room temperature [Dun97]. An estimate of a 0.4±0.2% contraction of the cells at experimental temperatures gave the lengths of the cold target cells (4.36 cm for hydrogen, 4.17 cm for deuterium). For all angular settings of the spectrometer during E91–016, the entire target could be seen by both spectrometers.

Target Density

At the nominal cryotarget temperatures and pressures, the densities of hydrogen and deuterium are known to within 0.4% and 0.3%, respectively [Dun97]. Limits on the accuracy of the temperature measurement add an additional 0.2% and 0.15% error to the density. Luminosity scans were performed so that target boiling could be measured as a function of beam current and raster amplitude. The results indicate a smooth dependence of boiling on the current: 3.8±0.4%/100 μA/1.0 mm raster [Gus96]. Extrapolating these results to the running conditions of E91–016 (20–30 μA, 0.50–0.63 mm raster) gives a density reduction of 0.55±0.20%.

Target Abundancy

Samples of the gases used in the targets were analyzed to measure purity. The hydrogen sample was found to be 99.8–99.9% pure. The error on hydrogen target abundancy is assigned to be 0.15±0.15%. The deuterium sample was found to contain 1.7% hydrogen in the form of molecular hydrogen and DH. The number of protons is therefore 1.7% higher than what would be seen in a pure deuterium target, and the number of neutrons is 1.7% less. These numbers are added or subtracted to the number of target particles in the analysis, with an error relative to the overall normalization of 0.5%.

3.5 Cut Variables/Cut Efficiences

3.5.1 SOS Aerogel Čerenkov

An aerogel cut is used to eliminate most of the pion events in the SOS without reducing kaon statistics. The efficiency of the aerogel was measured by studying

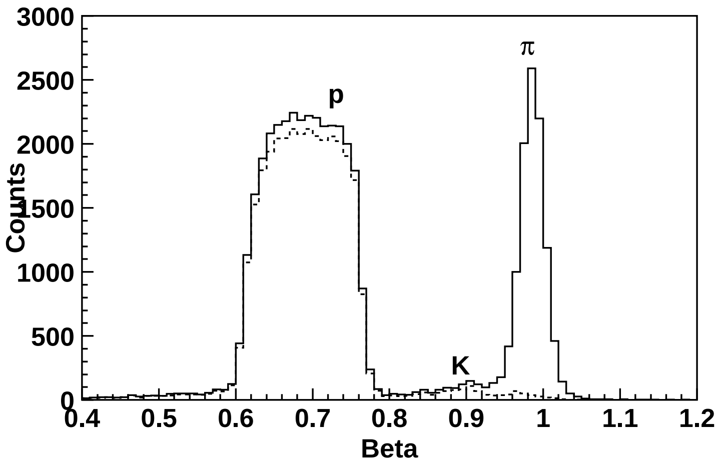

Figure 3.5: Effect of aerogel cut on SOS beta plot (solid line is without aerogel cut, dashed line is with aerogel cut). The only other cuts are on HMS and SOS delta.

pions at low momentum. Pions are a better tool for studying aerogel efficiency than kaons, since pions decay more rarely, and the decay products of the pions (muons) will have distributions in beta that are similar to the original pions since there is not a large mass discrepancy between pions and muons. The aerogel efficiency was measured as a function of number of photoelectrons, and for a threshold value of 2.5 (the cut used in this analysis, see Fig. 3.5 and Fig. 3.6), the efficiency was measured as 96.6±0.3% [Moh98].

Looking at the kaon data, the percentage of events that pass all cuts except the aerogel compared to the number that pass all cuts is less than 96.6%, ranging from 93.4 to 95.6%. As will be seen in Chapter 4, the Monte Carlo simulation

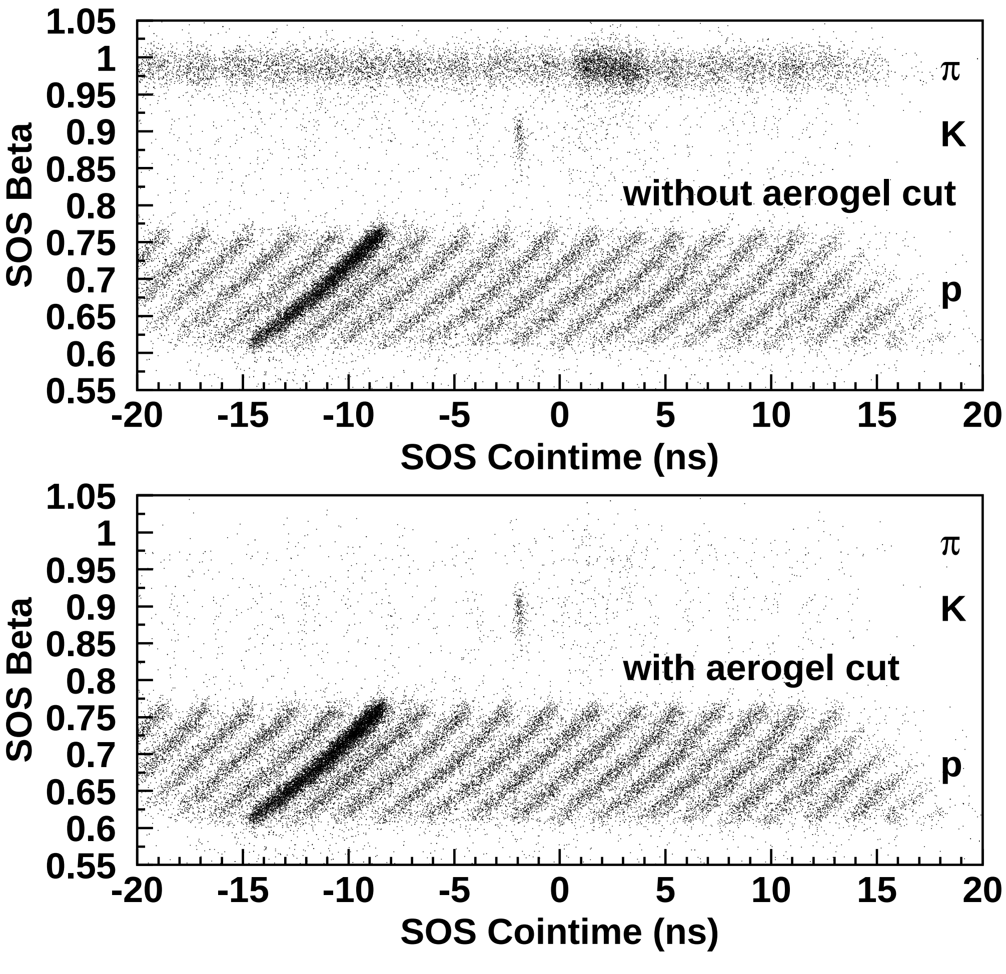

Figure 3.6: Effect of aerogel cut on SOS beta vs. cointime plot. The only other cuts are on HMS and SOS delta.

can be used to calculate a rough estimate of the number of events where a kaon has decayed but the event still passes all cuts except for the aerogel cut. This estimate is complicated by taking into account the number of these events that will be rejected by the hardware aerogel trigger. The simulation predicts as a rough estimate 2.4–3.0% of events due to decay products that will pass all cuts except aerogel. Adding this number to 93.4–95.6% gives us a number quite close to 96.6±0.3%. Consequently, it seems reasonable to use this efficiency in the analysis.

3.5.2 HMS Gas Čerenkov

A cut on the HMS Čerenkov is used to ensure that we are looking at an electron rather than a pion, since at HMS momenta pions and electrons have indistinguishable betas. The efficiency of the cut on the number of photoelectons in the HMS Čerenkov being greater than 2.0 is measured by comparing the number of events that pass all cuts to the number that pass all but the HMS Čerenkov cut. Approximately 0.2% of the good events are lost with this cut. The overall efficiency of this cut is assigned to be 0.998±0.002.

3.5.3 Coincidence Time

Cuts on coincidence time are used to define the real and random peaks as seen in Fig. 3.2. The average full width of a coincidence time peak is less than 400 ps

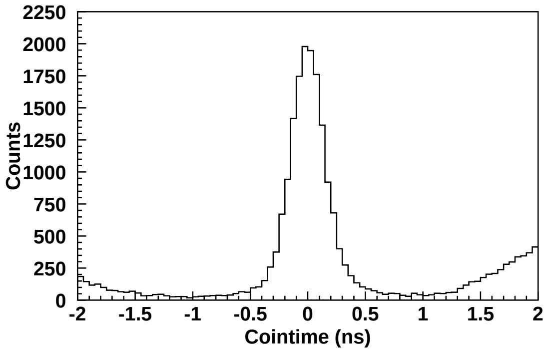

Figure 3.7: Cointime peak for kaons for events with missing mass between 1.08–1.24 GeV (no random subtraction).

(see Fig. 3.7). The window size used for cuts is 1.4 ns. The efficiency of this cut is measured by comparing the number of good events in a 1.4 ns window to the number of good events in a 2.0 ns window. The cut efficiency changes from setting to setting, and ranges from 99.50–99.93% with an error of 0.05–0.25%.

3.5.4 Beta$_p$

The velocity that a kaon would have given a momentum p is labeled β_p and is equal to $p/\sqrt{p^2 + M_K^2}$. This velocity can be compared to β calculated using the scintillator timing information. A histogram of $\beta_p - \beta$ for kaons has a Gaussian distribution centered at 0 and with most events being within a range of ± 0.04 (see Fig. 3.8 and Fig. 3.9). Pions and protons have values for $\beta_p - \beta$ that are typically 0.09 and greater. A cut on $\beta_p - \beta$ is quite valuable for kaon particle identification and effectively eliminates proton and pion contamination. The cut efficiency is

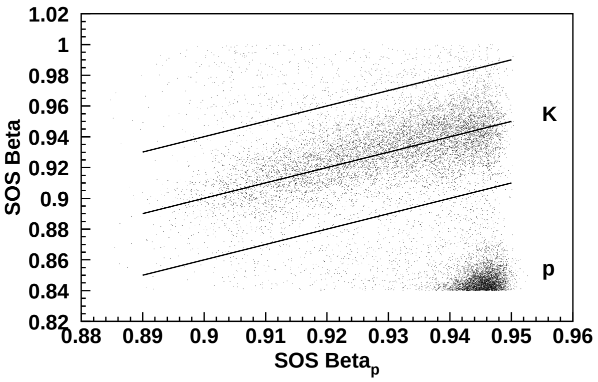

Figure 3.8: Beta$_p$ vs. Beta. A tight cut on missing mass near the Λ peak has been applied, as well as an aerogel cut to eliminate most of the pions. Lines are drawn to indicate $\beta_p - \beta$=0.00, and also $\beta_p - \beta$=$\pm$0.04, the boundaries of the cut.

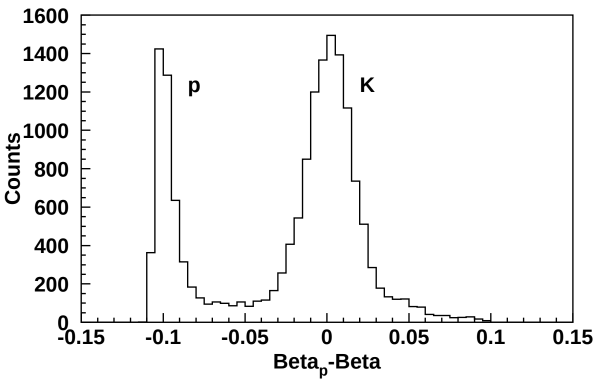

Figure 3.9: Beta$_p$-Beta. A tight cut on missing mass near the Λ peak has been applied, as well as an aerogel cut to eliminate most of the pions.

measured by comparing events that fall into a ± 0.04 window to those that fall into a ± 0.07 window. The setting-to-setting range of values is 96.5–97.9% with an error of 0.25–0.80%.

3.5.5 Beta=0

An event is assigned β=0 when there are not enough recorded scintillator hits, when there are not enough recorded scintillator hits on the track, when there are bad scintillator times extracted from the TDC/ADC outputs, and when the algorithm that calculates β fails. In the HMS very few electrons have β=0, and this inefficiency is estimated at 0.2%$\pm$0.2%. In the SOS there are many more events with β=0 failures. For these events the best way to judge whether they are kaons is to look at the missing mass, since there is no β dependence in that calculation. However, it is impossible to know the exact contribution of real and random protons and pions without using a β_p cut. The cut efficiency is calculated by looking at events that pass all cuts except β_p that have β=0 as compared to the events that pass all cuts. When the random subtraction is performed, the background away from the Λ and Σ^0 peaks is adjusted such that it is equivalent to zero; otherwise, the contribution from non-kaons lowers the background and the mass peaks from their real level. The cut efficiency is measured to be 96.6–98.3%, with an error of 0.2–0.9%.

Chapter 4

Monte Carlo Simulation

A realistic, accurate Monte Carlo simulation is essential in order to be able to understand kaon electroproduction on deuterium. Only by subtracting contributions from Λ and Σ^0 production on the proton can the Σ^- contribution on the neutron be extracted. Acceptances, Fermi motion, physics weighting, radiative corrections, and absolute normalizations for the simulation must all be well-modeled in order to extract interesting and valid results from the data.

The starting point for the formulation of the Monte Carlo simulation (SIMC) is a code written by N. Makins and T.G. O'Neill to study a color transparency (e,e$'$p) experiment at SLAC [Mak94a]. Major portions of the code, including machinery to study phase space as well as elastic and quasi-elastic scattering of electrons on protons, have been retained (and used for calibrations) with only minor modifications.

At the same time, many changes had to be made to include kaon electroproduction and to accurately model Hall C and its spectrometers. An outline description of the basic structure of the simulation code can be found in Appendix A.

4.1 Generation of Vertex Quantities

The simulation first randomly generates the 4-vectors for the outgoing electron and kaon. For each 4-vector three numbers are needed: momentum (delta) and two polar angle variables that define the direction of the particle: dtheta and phi. The electron 4-vector is determined, and two angle variables are added for the outgoing kaon, each variable being generated with a flat distribution over ranges greater than the limits of the spectrometer into which the particle will travel. These five variables make up the denominator of the electroproduction five-fold differential cross section.

For p(e,e$'$K$^+$)Y, the kinematics are now completely determined, and the kaon momentum can be computed. For d(e,e$'$K$^+$)Yn, the 4-vector for the target proton has to be known in order to solve the kinematics. To model the momentum distribution of the proton in the deuteron the Bonn potential (Fig. 4.1) is used. Since the volume integral of the momentum wave function squared is unity, the probability that a nucleon will have momentum less than or equal to P_N is equal to

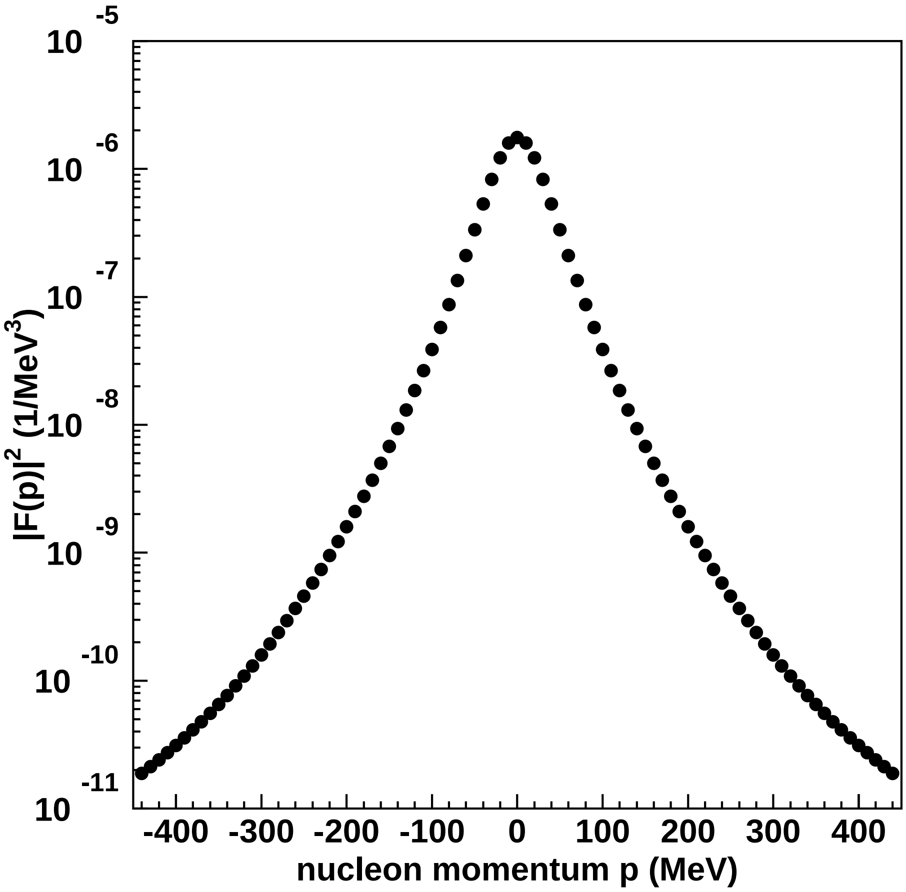

Figure 4.1: Bonn potential momentum wave function $|F(p)|^2$, normalized as seen in Fig. 4.2.

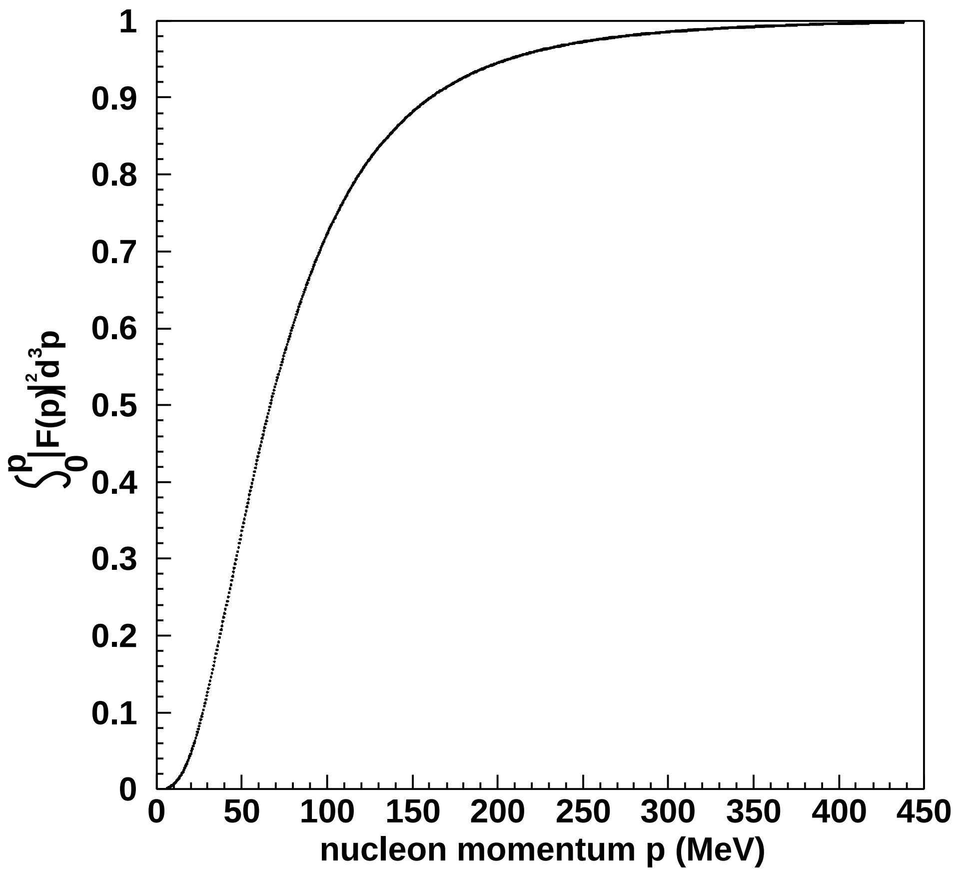

Figure 4.2: Integrated Bonn potential momentum wave function $\int_0^p |F(p)|^2 d^3p$. The integral becomes one near 490 MeV.

the volume integral of the wave function squared over the momentum range from zero to P_N (see Fig. 4.2). To generate the Fermi motion for the initial proton, a random number is compared to the volume integral up to P_N, where P_N ranges from 0.5 to 490 MeV in 0.5 MeV steps. The first P_N for which the integral is greater than the random variable is used as the initial proton momentum. The kinematics for the kaon momentum in the lab frame where the deuteron is at rest can then be determined. If the kinematics cannot be solved due to incompatible random choices for the variables, the event is a failure. If a solution is found, then the electron and the kaon are transported through the spectrometer to see if they pass the spectrometer cuts.

4.2 Transport through the Spectrometers

The vertex position in the extended liquid target is chosen at random along the beam direction, and the x and y positions are chosen to fit the distribution of the actual beam position (including offsets and rastering) for the set of data being modeled. The path through each spectrometer is determined by a set of matrix elements that transport the particle through the magnet elements to the detector hut. The matrix elements are derived from the COSY INFINITY transport program described above. In the SOS, the matrix elements are sequential (go from

A$\rightarrow$D using matrices that transport from A$\rightarrow$B, B$\rightarrow$C, and C$\rightarrow$D) and based on a magnetic field mapping. In the HMS, the matrix elements are forward (go from A$\rightarrow$D using matrices that transport from A$\rightarrow$B, A$\rightarrow$C, and A$\rightarrow$D) and are calculated assuming the quadrupoles and dipoles are simple magnets that can be well-modeled by COSY. Apertures of the collimator, the magnets, and the detector elements are included in the model, and particles that go outside one of these apertures are thrown out.

Multiple scattering can take place anywhere in the spectrometer: in the target, at vacuum windows, in air, on drift chamber wires, or in scintillator paddles. The simulation calculates multiple scattering at all of these places. For a realistic model of drift chamber resolution, the position of the particle in each chamber plane is smeared with a Gaussian of width equal to the measured wire chamber resolutions. To fit the measured wire chamber resolutions two Gaussians are needed, with one Gaussian three times as broad and with about seven times less strength than the other (see Fig. 4.3). The source of the broader Gaussian is non-optimal tracking for events with more than six hits in a drift chamber. In the simulation, this effect is modeled by increasing the smearing factor for the percentage of data events with more than six hits. If the particle makes it through all the required detector elements for our hardware trigger and software particle ID (in the HMS, to the third scintillator plane; in the SOS, to the aerogel detector), the event is considered to

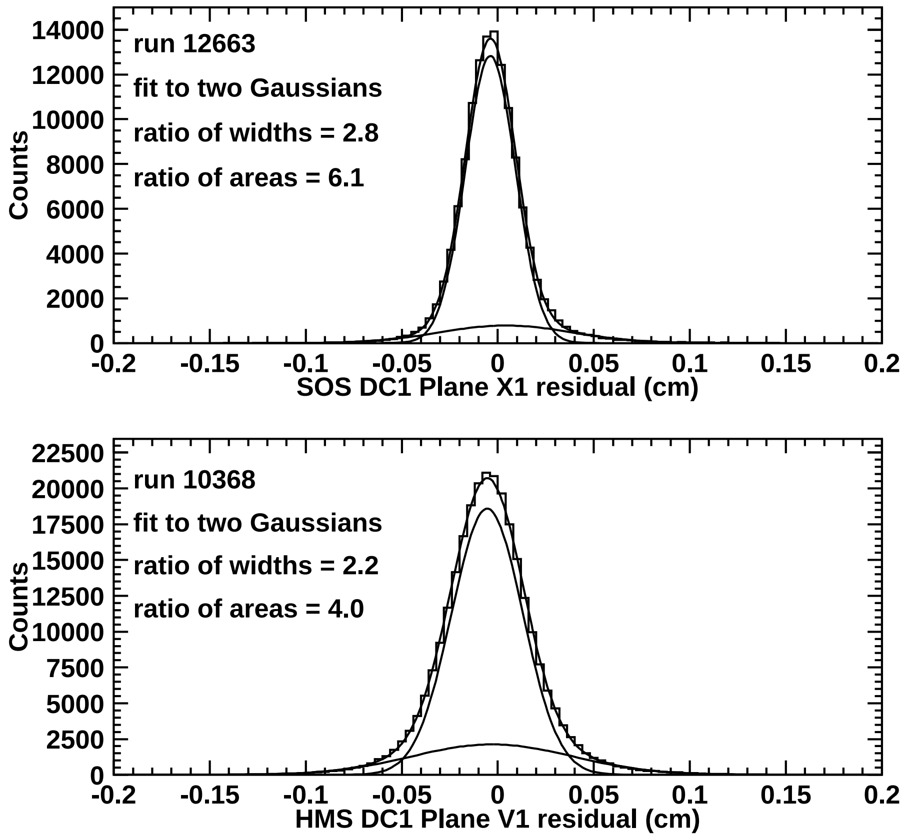

Figure 4.3: Wire chamber resolutions for electrons fitted to the sum of two Gaussians. The two fit Gaussians and their sum are plotted. The ratios listed are the ratios of one fit Gaussian to the other. In these examples the relative widths are smaller and the relative strengths are larger than what is used in the simulation.

have made it through the detector, and focal plane quantities are computed based on the smeared wire chamber positions. The focal plane quantities are then used to calculate the reconstructed event quantities at the target. The reconstruction matrix elements are an inversion of the forward matrix elements used to transport from the target to the focal plane.

4.3 Physics Cross Section Weight

If the electron and the kaon make it through the spectrometers and pass loose momentum and angle cuts, a physics cross section weight can be assigned. The extraction of a cross-section parameterization from the data will be discussed in Chapter 5. Using this parameterization, a cross section in the center-of-mass of the virtual photon and target nucleon $\frac{d\sigma}{d\Omega_K^*}$ for each event is calculated as a function of the invariant mass W. This number is converted through multiplication by a Jacobian and a virtual-photon flux to the five-fold differential cross section $\frac{d\sigma}{dE_e d\Omega_e d\Omega_K}$. Also, a correction factor for decay is calculated by evaluating the pathlength of the kaon through the SOS from the target to the aerogel detector 9.8 m away. Based on uncertainties in the total pathlength and the distance through the aerogel required to create a threshold number of photoelectrons, the error in this decay correction factor is assigned to be 0.9%. The cross section weight is multiplied by the probability that the kaon would not have decayed before the aerogel detector.

4.4 Decay Corrections

Monte Carlo simulation studies are done to determine whether any kaons that decay before the aerogel would be counted as good kaons based on the behavior of the kaon's decay products (see Table 4.1 for the dominant decay channels). Decay along the flight path of the kaon through the spectrometer is modeled by looking at the path in discrete steps. At each step the probability of decay over that step can be calculated, and if a random number is less than that probability then the kaon has decayed. For the dominant two-body decays $K^+ \rightarrow \mu^+\nu_\mu$ (63.51%) and $K^+ \rightarrow \pi^+\pi^0$ (21.16%) the decay particles' momenta in the decay rest frame is kinematically fixed. For the remainder of the decays (three-body) into charged particles, an average momentum for the decay particle is picked rather than modeling the momentum distribution exactly. Next, a random direction in the rest frame is chosen, and the 4-vector of the particle of interest (π^+ or μ^+) is boosted back into the lab frame. The decay particle is then transported through the remainder of the spectrometer.

If the particle makes it to the aerogel, then three issues need to be addressed. The first is whether the velocity of the particle (known from its momentum) is low enough so that it would not fire the aerogel. The second is whether the beta of the particle (as would be calculated using time-of-flight between the scintillator planes) would correspond to the beta of a kaon based on the cut placed on the data. The third is whether the scintillator hits of the decay particle lie along the track of the particle as calculated in the focal plane, such that there would be enough scintillator hits (three out of four) for the replay software to calculate a non-zero beta. If these conditions are not satisfied the event is rejected. A close look reveals that there is no contribution from kaons that decay before the detector hut. Once in the detector hut, there is only a small percentage of decay particles going in a backwards enough direction in the rest frame to have velocities less than the aerogel threshold. However, the probability for kaon decay is high enough that these events make a contribution. The total contribution of decay products to the total is estimated as $3\%\pm1\%$.

At the same time, the contribution of decay products that satisfy the second and third conditions above but are above the threshold for firing the aerogel can be studied. These events contribute to the measured inefficiency of the aerogel detector. Comparing data runs with aerogel in and out of the trigger reveals that having aerogel in the trigger reduces the number of recorded data events that have more than 2.5 aerogel photoelectrons by a factor of approximately 2.5. Since the simulation assumes that aerogel is not in the trigger, this contribution of decay

Table 4.1: Table of K^+ decay branches. For 2-body decays, p is the rest frame momentum for each decay product. For 3-body decays, p is the maximum momentum for any of the decay products in the rest frame. From [Cas98].

Decay Mode	Branching Ratio	p (MeV)
$\mu^+\nu_\mu$	(63.51±0.18)%	236
$e^+\nu_e$	$(1.55\pm0.07)\times10^{-5}$	247
$\pi^+\pi^0$	(21.16±0.14)%	205
$\pi^+\pi^+\pi^-$	(5.59±0.05)%	125
$\pi^+\pi^0\pi^0$	(1.73±0.04)%	133
$\pi^0\mu^+\nu_\mu$	(3.18±0.08)%	215
$\pi^0 e^+\nu_e$	(4.82±0.06)%	228

products has to be divided by this factor, and the result ranges from 2.4–3.0%. This number is used in determining the aerogel cut efficiency in Chapter 3.

4.5 Radiative Corrections

The Monte Carlo simulation also deals with radiative corrections. The radiative code is mostly identical to the code found in the original version of the simulation, so a detailed description will not be given here (for more details, see [Mak94b],[One94],[Mak98]). Since little work has been done on calculating radiative corrections for p(e,e$'$K$^+$)Y, the approximation calculating the radiative corrections for p(e,e$'$p*) is used, where p* is an offshell proton. In our case, the outgoing proton is quite offshell: it is a kaon. Since the contribution to the ra-

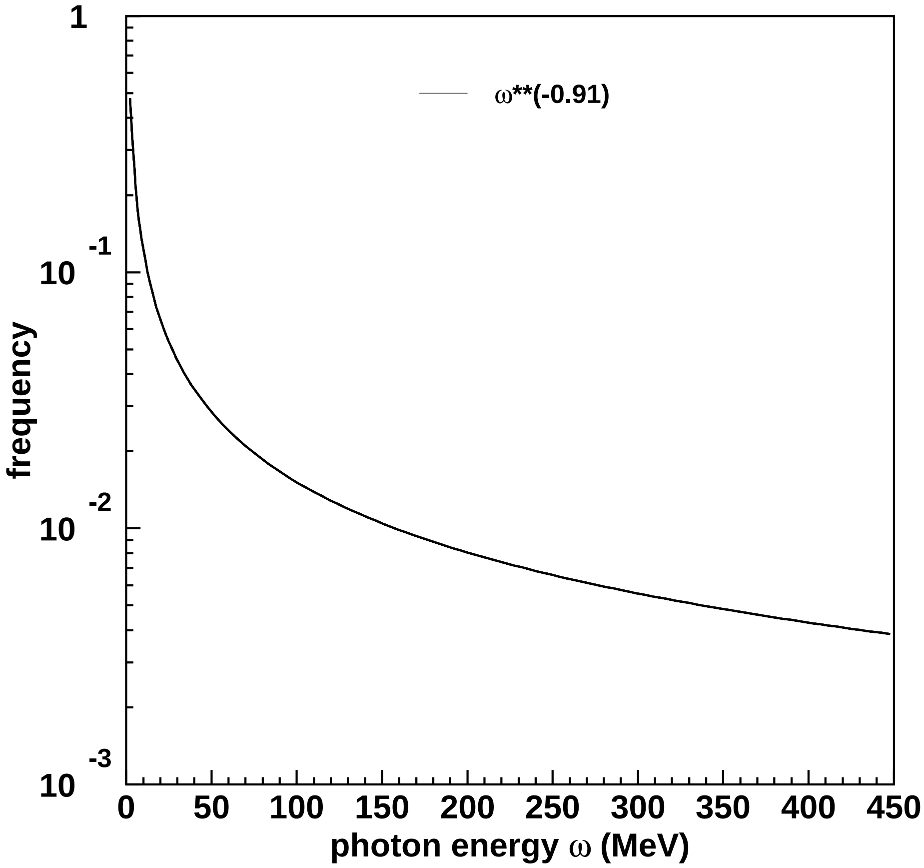

Figure 4.4: Radiated photon distribution for r=0.09, normalized such that the frequency at ω=1 is equal to one.

diative corrections that is directly related to the outgoing hadron should be small, this approximation should suffice. All the contributions to radiative corrections are calculated, both hard and soft (internal and external). The relative probability for radiation in each arm (incoming electron, outgoing electron, and outgoing kaon) is computed, and the radiated photon is assigned to be in a particular arm based on this probability. If the outgoing electron will not fall into the spectrometer delta acceptance without being radiated, the radiated photon is forced to be in that arm, and the event is weighted by the relative probability that the outgoing electron would have radiated. The initial range of outgoing electron momenta thrown is verified to be large enough to include all events that might radiate into the acceptance. However, a range of final electron momenta is not determined such that an individual event would fall into the acceptance, a process that would add another weight to the radiative corrections and would make the calculation of the overall weight much more complicated.

The radiated photon is fixed in direction to be in the same direction as the particle from which it radiated: this assignment is the peaking approximation. The energy of this photon is calculated based on a ω^{r-1} distribution function, where r (a positive number much less than one) is determined by the formulas used for radiative corrections (see Fig. 4.4). If the initial electron radiates, the entire event is reprocessed. If one of the final particles radiate, only the 4-vector for that particle is modified. All photon radiation takes place at the vertex. In the end radiative weights are combined with the physics cross section weight.

4.6 Event Weight

Both the number of successful events and the number of tries are tabulated. Combining the ratio of the successes to tries with the initial five-dimensional generation volume gives the e–K coincidence acceptance of the spectrometers. Including target normalizations as well as the Monte Carlo weights, an overall yield is computed that can be compared with the data. A cross section is extracted from the data by multiplying the average cross section of the Monte Carlo simulation by the scaling factor necessary to match the simulation to the data.

4.7 Elastic and Quasi-elastic Comparison

Initial checks of the simulation are done on (e,e′) and (e,e′p) elastic data. Elastic data are good for calibrations since the incoming electron energy and the scattered electron angle completely determine the kinematics of the reaction. By varying the central momentum of the spectrometers, a comparison between the experimental and simulation acceptance can be made at different positions in the focal plane for different average spectrometer deltas. Single arm (e,e′) data are especially useful for comparing the measured and predicted widths for reconstructed invariant mass, verifying whether the spectrometer resolution of the model agrees well with the data. Also, the strengths of radiative tails can be checked. The results of studies of (e,e′) on hydrogen in both spectrometers show that the invariant mass width and radiative tail strength are the same for the data and for SIMC, and total yields agree to within 2% in the HMS and 4% in the SOS (see Fig. 4.5). Good agreement was also seen in the y-scaling experiment E89–008 that utilized a Monte Carlo simulation virtually identical to the one used here [Arr98].

Analysis of (e,e′p) data is important in determining how well the simulation models the coincidence acceptance of the spectrometers. Due to the correlations between angles and momenta in the two spectrometers, only small bands of phase space can be checked using elastic data. One effect that can be clearly seen looking at (e,e′p) data is the punch-through of protons through the collimator (see Fig. 4.6). The protons lose a fixed amount of energy (∼200 MeV) that corresponds to the amount of energy loss one expects of a proton traveling through 6.3 cm of tungsten. So even if hadrons are not stopped by the collimator, their energy loss is so great that their reconstructed missing mass would be well outside normal cuts, and the conclusion can be made that the collimator truly does define the solid angle acceptance for the spectrometers.

Another effect seen while comparing data and simulation for (e,e′p) is an offset

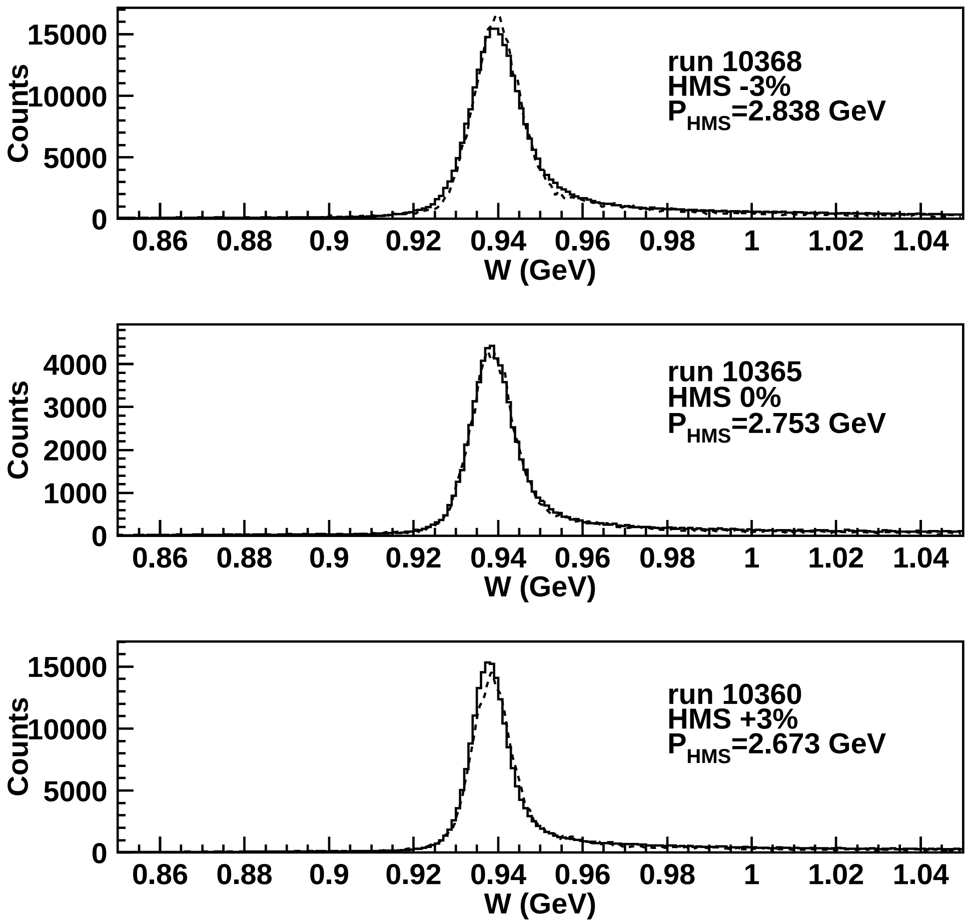

Figure 4.5: Hydrogen (e,e′) Data vs. SIMC. The solid line is the data, and the dotted line is SIMC. No dummy subtraction has been done on the data (∼4% of the total yield). Central momenta have been adjusted by 1.5–3.0 MeV so that the data and simulation peaks coincide. The percentages for the HMS indicate where the data were centered in the focal plane in delta. Note the decrease in resolution width as delta increases.

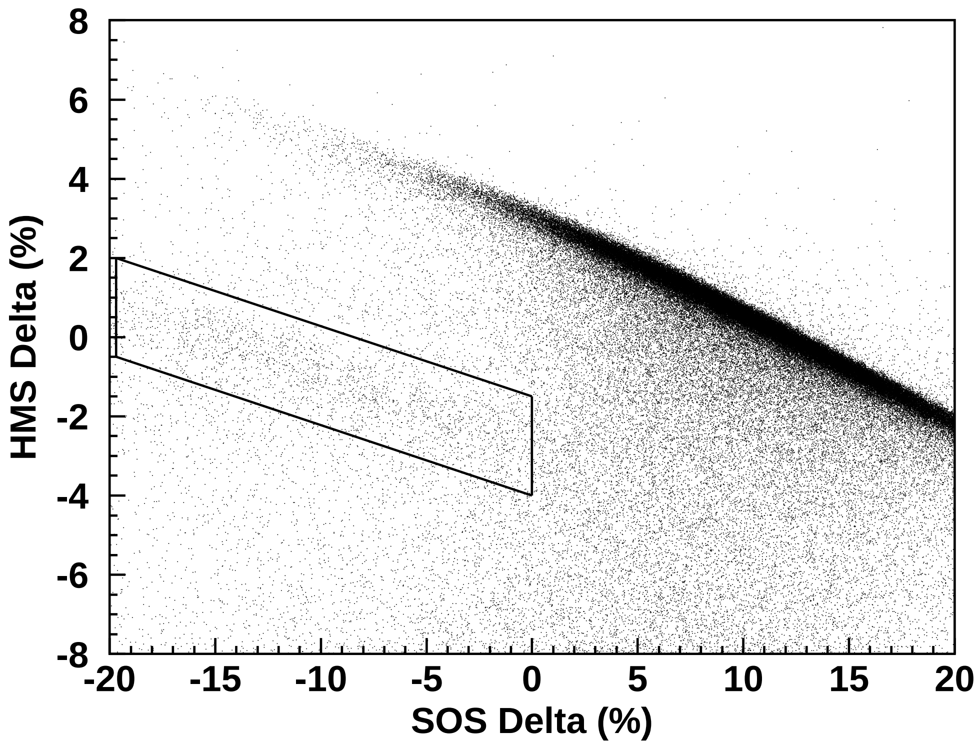

Figure 4.6: Deuterium quasi-elastic SOS (proton) delta vs. HMS (electron) delta with no cuts on the data, where the SOS central momentum is +12% in the elastic scan (0.947 GeV). Proton collimator punch-through can clearly be seen in the shadow band of events to the left of the quasi-elastic peak.

in the beam position on target during two sets of data taking. Elastic scans in the SOS, where data were taken at five different central values of the protons in delta at the focal plane (-12%, -6%, 0%, +6%, and +12%), were performed during running in August and in September, with a three week period with no data taking in between. For both elastic scans the spectrometers were at the same angles and had the same set of central momenta, but qualitative differences in the two sets of data were observed. Shifts were found in all focal plane spectra, most remarkably a shift in the SOS transverse position in the focal plane. Also, a significant shift was seen in the reconstructed y-target position (see Fig. 4.7). This effect also appeared in the kaon data. The simulation modeled the September spectra well, but to reproduce the August data, offsets in both the longitudinal position of the target and the vertical position of the beam had to be applied. Since kaon data taking at some settings took place in both August and September, to maximize statistics data taken during both periods of time were combined and compared with the simulation that well reproduced September data. This method led to some broader data resolutions and possibly some small systematic error near the edges of the spectrometer cuts.

The coincidence missing-mass resolution was not perfectly matched between the data and SIMC. As can be seen in Fig. 4.8, the data resolution is much broader than that of the simulation. The simulation could never be reasonably modified

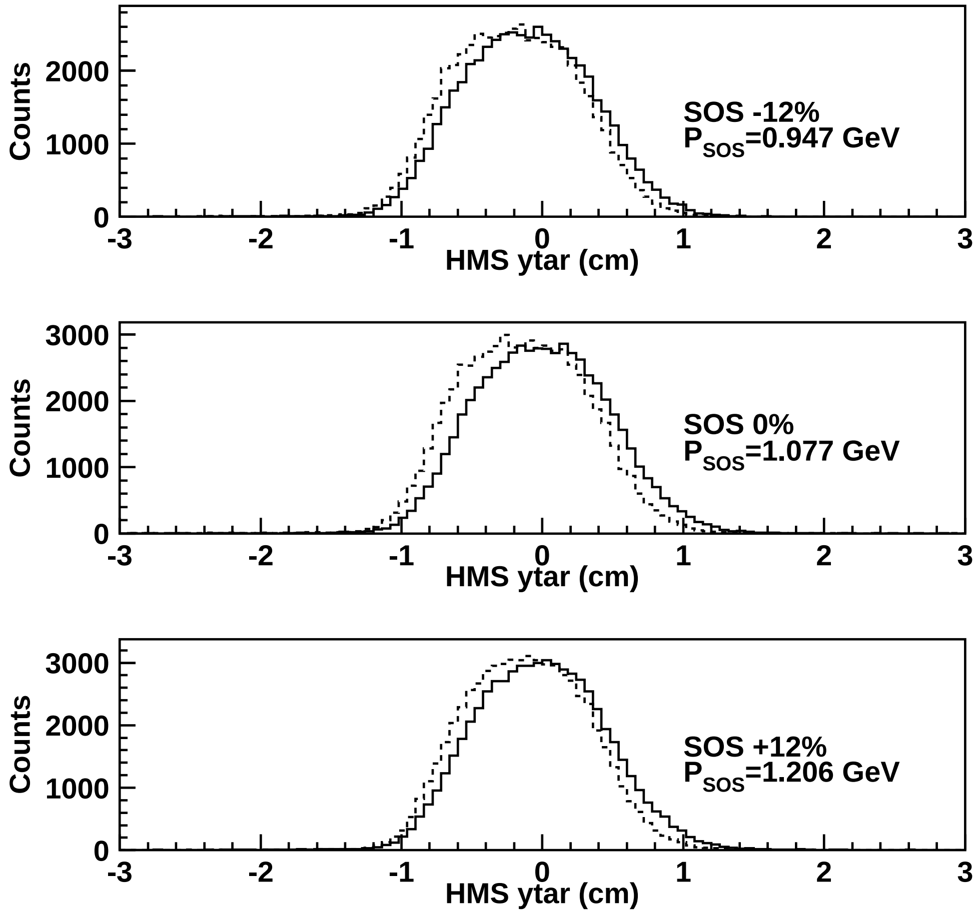

Figure 4.7: Deuterium quasi-elastic August vs. September data. The solid line is August data, and the dotted line is September data. Offsets of 0.10–0.15 cm can be seen.

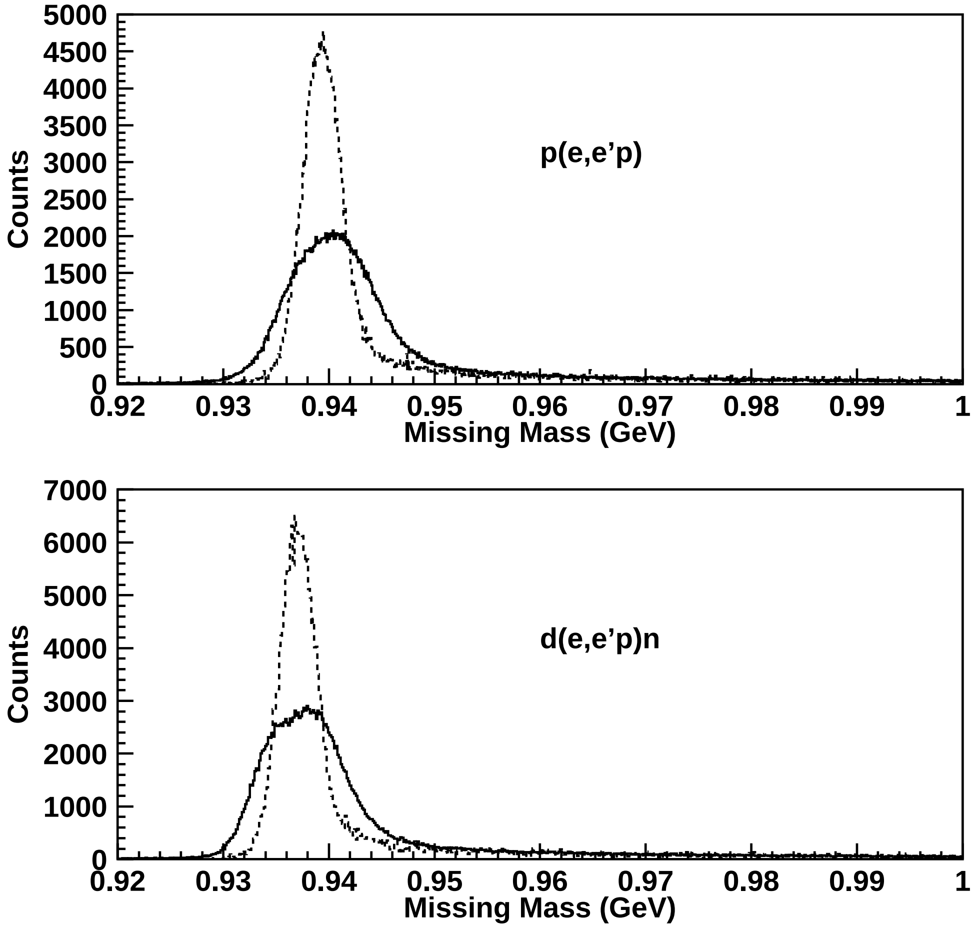

Figure 4.8: Elastic and quasi-elastic data vs. SIMC missing mass. The solid line is the data, and the dotted line is SIMC. Missing mass has been calculated for hydrogen by assigning the target mass to be the mass of the deuteron. Note the difference in reconstructed missing-mass resolution.

to match the coincidence resolution and single-arm resolutions at the same time. A similar missing-mass resolution difference was also seen in the kaon hydrogen data.

Data and simulation were compared for both p(e,e′p) and d(e,e′p)n. The deuterium data tested the procedure for including the deuteron wave function. Agreement between focal plane and reconstructed quantities as seen in Fig. 4.9 and Fig. 4.10 indicate the strong agreement between simulated and real data. To obtain this level of agreement for the reconstructed quantities a number of offsets had to be applied to the data. These offsets indicate problems with the reconstruction matrix elements, as the focal plane quantities are in good agreement with no offsets applied. Offsets were determined in three separate ways: getting information about reconstructed angles using sieve slit data, looking at invariant mass versus reconstructed quantity spectra to remove any dependences, and the direct comparison between data and SIMC reconstructed quantities. Table 4.2 lists the offsets used in this analysis.

The offset most important to the analysis involves ssdelta. The SOS has been found to require offsets in its central momentum for settings away from the one at which the SOS matrix elements were fitted [Gas98]. Showing that the focal plane quantities agree indicates that the problem was not with the SOS field settings, but rather with the matrix elements themselves. At the SOS central momenta

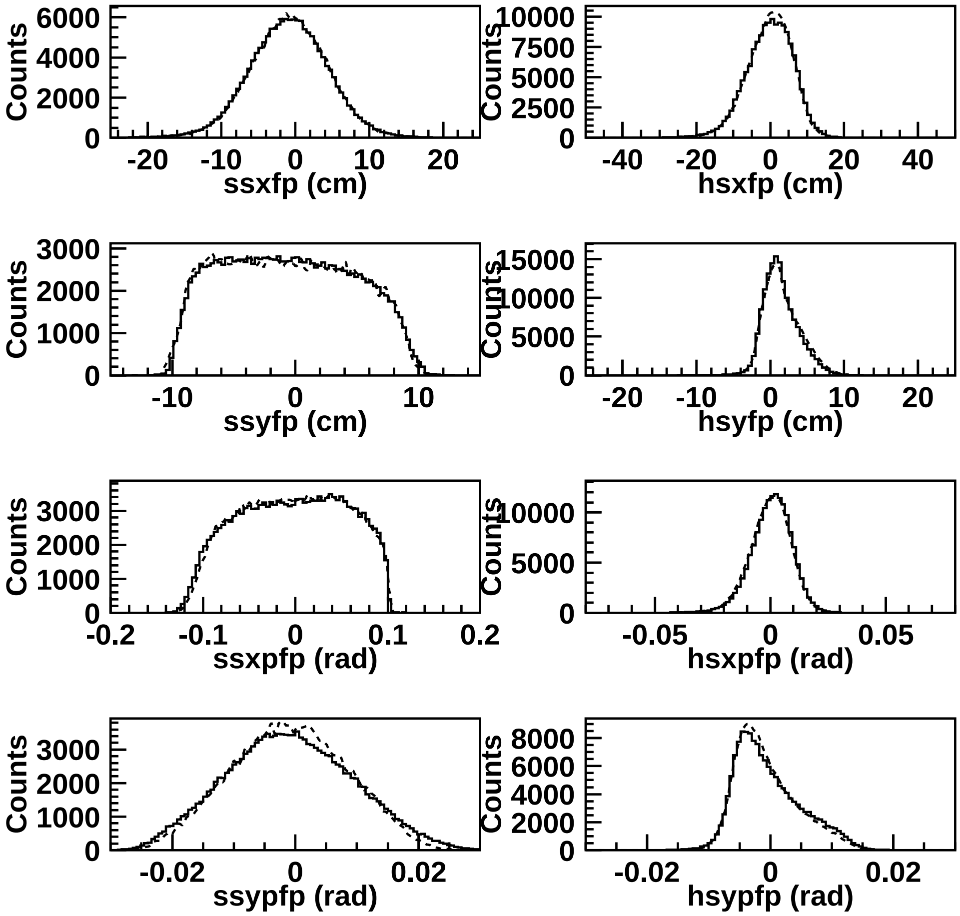

Figure 4.9: Deuterium quasi-elastic data vs. SIMC comparison for focal plane quantities. The solid line is the data, and the dotted line is SIMC. A missing mass cut of 0.9245–0.9545 GeV has been applied, and the SIMC spectra have been normalized to match the data yield.

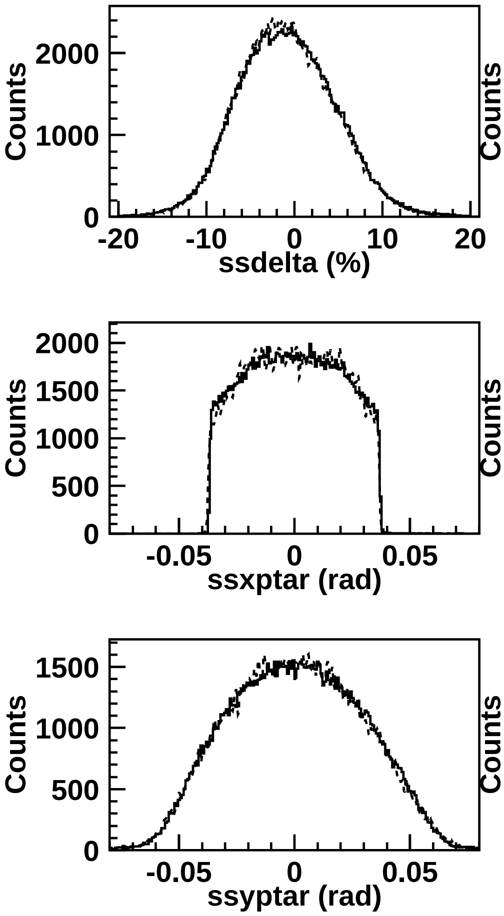

Figure 4.10: Deuterium quasi-elastic data vs. SIMC comparison for reconstructed quantities. The solid line is the data, and the dotted line is SIMC. A missing mass cut of 0.9245–0.9545 GeV has been applied, and the SIMC spectra have been normalized to match the data yield.

Table 4.2: Offsets for reconstructed quantities.

Quantity	Quantity with offsets
hsdelta	hsdelta+4.473×hsxptar
hsxptar	hsxptar-(hsyptar+hsytar/127.7)/20.-0.0006+0.0035
hsyptar	hsyptar+hsxptar/40.-0.0008
ssdelta	ssdelta+0.5
ssxptar	ssxptar+0.00262
ssyptar	ssyptar-0.0003

used in E91–016, the offset is found to be 0.50%.

Even when all HMS and SOS reconstructed quantities, including invariant mass, have good agreement between data and SIMC, in order for the (e,e$'$p) missing-mass peaks to coincide offsets have to be applied to the nominal beam energy (between 3–5 MeV). These offsets could indicate true shifts in the beam energy or spectrometer misalignments relative to each other or to the target. Beam energy measurements performed in the Hall C beam arc have been shown to be unreliable on the order of 1–2 parts per thousand (3–6 MeV) [Mac98]. The procedure used for this analysis is to use the nominal beam energies and make adjustments to align missing-mass spectra. The broad resolution in the (e,e$'$p) data make it unclear exactly what offset should be applied. The data for kaon electroproduction on hydrogen have peaks with very narrow widths, and the shifts required to align data and SIMC missing mass are 1 MeV or less, indicating problems with (e,e$'$p) simulations may not reflect problems that are also seen in (e,e$'$K$^+$) simulations. This observation is taken into account when assigning an uncertainty to the spectrometer acceptances below.

Yields for p(e,e$'$p) and d(e,e$'$p)n were measured for the data and compared to the yields generated by SIMC. The results for the SOS elastic scan are displayed in Fig. 4.11. A comparison of August and September data agreed to better than 2% at all settings, so in the figure only August results are shown. There appears to be a rise in the data/SIMC ratio when the data are at large positive values of delta in the SOS focal plane. This rise could indicate a systematic defect in the simulation, and it could be specific to proton elastic data. The assigned values for the systematic uncertainties in the HMS and SOS acceptances are both 2%. Looking at the other points the data/SIMC ratio is in good agreement with 1.00 for hydrogen. This result was also found using a similar Monte Carlo simulation during the color transparency experiment E91–013 [Dut99]. The data/SIMC ratio for deuterium tracks the value for hydrogen quite closely: the deuterium/hydrogen ratio is 0.95–0.96 at all points except one, and the average value is 0.95. This consistency is a strong indicator that SIMC deals properly with deuterium targets.

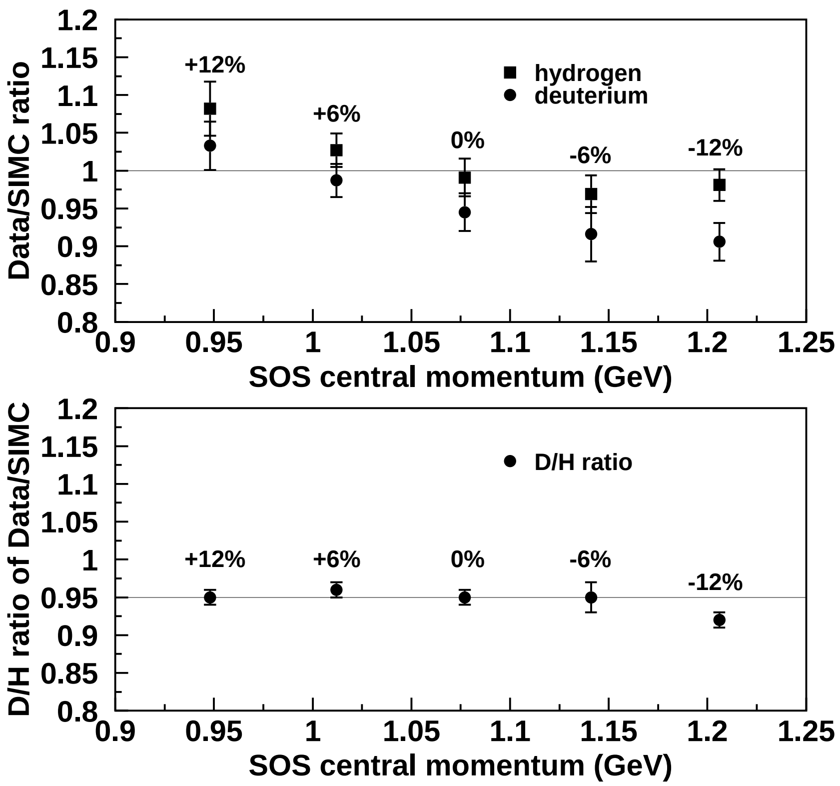

Figure 4.11: Elastic and quasi-elastic data vs. SIMC comparison. The top picture shows the ratios of data/SIMC for the August SOS elastic scan, the percentages indicate the position in delta in the SOS focal plane. Data points are the averages over four sets of cuts: tight or loose cuts on HMS delta, and tight or loose cuts on missing mass. Missing mass has been calculated for hydrogen by assigning the target mass to be the mass of the deuteron. Error bars combine the range of values for the four cuts with the 2% range in data/SIMC ratios for August and September elastic scans. All ratios have been multiplied by a proton absorption factor of 1.05. A line has been drawn corresponding to a ratio of 1. The bottom picture shows the ratios of deuterium/hydrogen data/SIMC values. The error bars indicate the range of values for the four cuts.

4.8 Kaon Comparison

Separate Monte Carlo simulations are run for the reactions p(e,e$'$K$^+$)Λ,Σ^0 and d(e,e$'$K$^+$)Λn,Σ^0n,Σ^-p. For each reaction we calculate the average cross section when all cuts corresponding to the data cuts are applied. The cuts on kaon data are listed in Table 4.3. The cuts on reconstructed angles are meant to eliminate events that are reconstructed outside the acceptance of the spectrometers. For each data run, the coincidence time is shifted such that the kaon coincidence peak is centered at zero, and then the cointime cut is applied. All corrections corresponding to efficiencies, absorption, and total charge are applied to the simulation. The agreement between data and SIMC focal plane and reconstructed quantity distributions can be seen is Fig. 4.12 and Fig. 4.13.

To extract deuterium cross sections, Λ and Σ^0 cross sections on hydrogen must first be extracted. The integrals of the missing-mass peaks from the data and simulation are compared over the range 1.100 to 1.165 GeV. The scaling factor for the Λ is used to calculate the contribution to the Σ^0 peak from 1.180 GeV to 1.230 GeV due to the Λ radiative tail. Once this contribution is subtracted from the Σ^0 data, the integrals of data and SIMC can once again be compared. The average cross sections for the hydrogen data are defined as σ_{H_Λ} and $\sigma_{H_{\Sigma^0}}$.

The deuterium missing-mass spectra are now studied. The assumption is made

Table 4.3: Cuts on kaon production data.

Cuts on both data and SIMC
abs(ssdelta)$<$20. (percent)
abs(hsdelta)$<$8. (percent)
abs(ssxptar)$<$0.04 (mrad, SOS acceptance $\sim \pm 0.037$)
abs(ssyptar)$<$0.07 (mrad, SOS acceptance $\sim \pm 0.056$)
abs(hsxptar)$<$0.08 (mrad, HMS acceptance $\sim \pm 0.070$)
abs(hsyptar)$<$0.04 (mrad, HMS acceptance $\sim \pm 0.028$)
Cuts on data only
abs(cointime)$<$0.7 (ns)
abs($\beta - \beta_p$)$<$0.04 (SOS beta)
saernpe$<$2.5 (number of SOS aerogel photoelectrons)
abs(hsbeta-0.9)$<$0.4 (HMS beta)
hcernpe$>$2. (number of HMS Čerenkov photoelectrons)

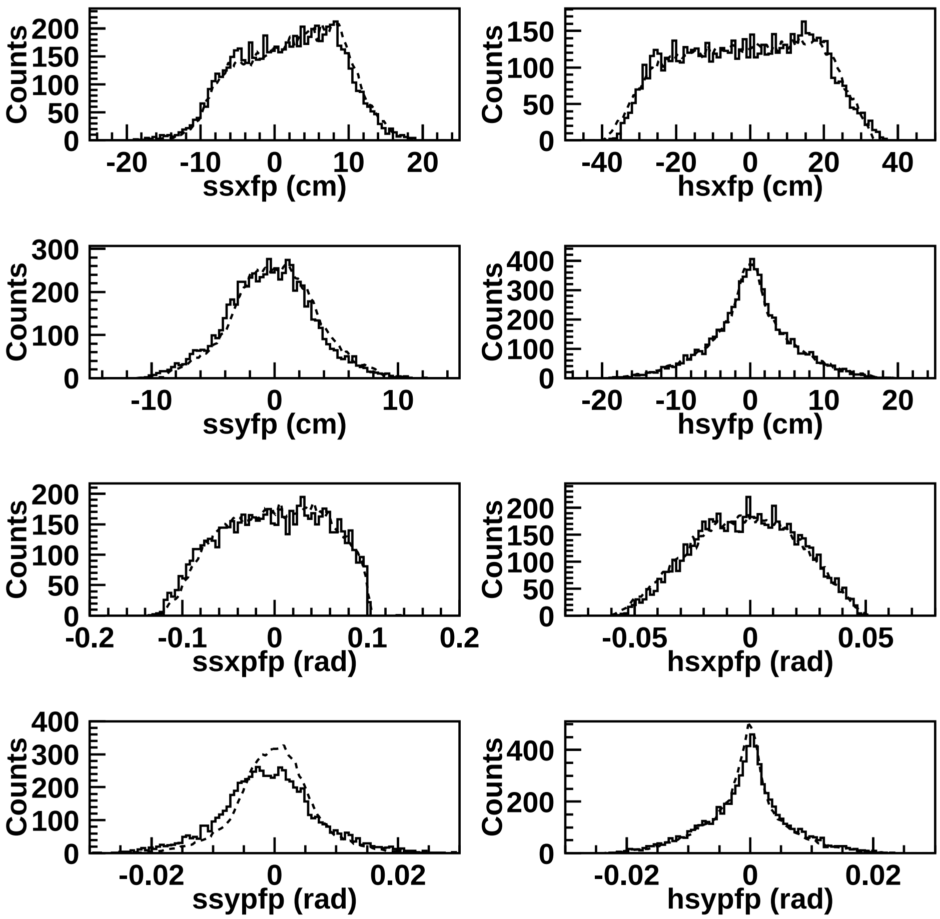

Figure 4.12: Hydrogen Λ production data vs. SIMC comparison for focal plane quantities. The solid line is the data, and the dotted line is SIMC. A missing mass cut of 1.100–1.165 GeV has been applied, and the SIMC spectra have been normalized to match the data yield.

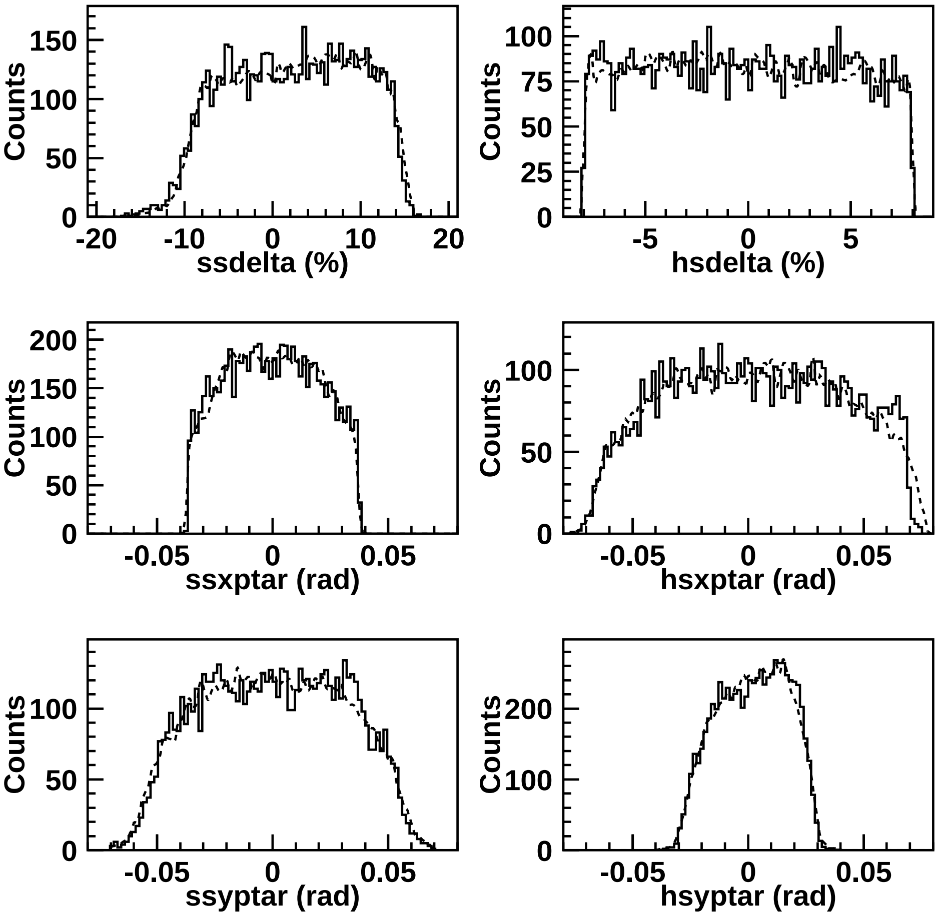

Figure 4.13: Hydrogen Λ production data vs. SIMC comparison for reconstructed quantities. The solid line is the data, and the dotted line is SIMC. A missing mass cut of 1.100–1.165 GeV has been applied, and the SIMC spectra have been normalized to match the data yield.

that $\sigma_{D_\Lambda}/\sigma_{H_\Lambda}$ is equal to $\sigma_{D_{\Sigma^0}}/\sigma_{H_{\Sigma^0}}$. Without this assumption it is impossible to separate the contributions from d(e,e$'$K$^+$)Σ^0n and d(e,e$'$K$^+$)Σ^-p. A two-parameter MINUIT [Cer94] fit of the simulation to the data is performed, with the two parameters being the scaling factors of the Λ and Σ^- simulations. From this fit σ_{D_Λ} and $\sigma_{D_{\Sigma^-}}$ are obtained. At the same time, the Σ^- can temporarily be ignored, and the deuterium data fit to only Λ and Σ^0 simulations. This fit gives a cross section for the combined Σ production. The subtraction of the Σ^0 cross section on hydrogen (scaled by $\sigma_{D_\Lambda}/\sigma_{H_\Lambda}$) leaves a cross section for Σ^- that can be compared to the cross section extracted using Λ and Σ^- fitting.

4.9 Systematic Errors

A summary of the systematic errors for E91–016 is given in Table 4.4. Scale errors are constant for a given setting and target and do not change from run to run. Random errors change from run to run and need to be kept even when taking a ratio of deuterium to hydrogen cross sections at the same experimental setting. Additional systematic errors arise in the extraction of cross sections, as the cross sections depend on the physics model used to weight the data. The cross sections for Λ production on hydrogen and deuterium as well as for Σ^0 production on hydrogen are fairly insensitive to the physics model, and the associated systematic uncertainties are therefore small (0.25–1.2% (average 0.55%) for σ_{H_Λ}, 0.65–3.2% (average 1.7%) for σ_{D_Λ}, and 0.9–6.75% (average 3.2%) for $\sigma_{H_{\Sigma^0}}$, depending on the kinematic setting). However, $\sigma_{D_{\Sigma^-}}$ is highly dependent on the physics model, since the shapes of the deuterium missing-mass spectra are sensitive to the model used, and shifts in the Λ peak change the total number of counts in the Σ peak.

Table 4.4: Systematic errors in E91–016.

Source	Percent Error
Scale Errors (cancel in D/H ratio)	
Kaon absorption	1.0
Target length	0.2
HMS acceptance	2.0
SOS acceptance	2.0
Radiative corrections	0.5 (hard)
	1.0 (off-shell approximation)
Decay length	0.9
Decay products	1.0
Scale Errors (do not cancel in D/H ratio)	
Target abundancy	0.15 (Hydrogen)
	0.50 (Deuterium)
Target density	0.4 (Hydrogen)
(eq. of state)	0.3 (Deuterium)
Random Errors	
Target density	0.28 (Hydrogen)
(temp and raster)	0.25 (Deuterium)
Aerogel efficiency	0.3
HMS Čerenkov efficiency	0.2
HMS tracking efficiency	1.5
SOS tracking efficiency	1.5
HMS beta=0	0.2
SOS beta=0	0.2–0.9
Cointime window	0.05–0.25
Beta-Beta$_p$ window	0.25–0.80
BCM charge	1.5
Coincidence blocking	0.5
Total	4.4–4.6

Chapter 5

Results

5.1 Hydrogen

5.1.1 Missing-Mass Spectra and Cross Sections

Hydrogen (e,e′K$^+$) missing-mass spectra are displayed in Figs. 5.1–5.6. The data have been divided into four groups: W=1.90 GeV, Q^2=0.38 GeV^2 (Figs. 5.1–5.3); W=1.80 GeV, Q^2=0.50 GeV^2 (Fig. 5.4); W=1.76 GeV, Q^2=0.52 GeV^2 (Fig. 5.5); and data taken at E_{beam}=2.445 GeV (Fig. 5.6). The simulations are scaled to the data according to the method described in Chapter 4. Figs. 5.1–5.3 show how the widths of the data and simulation missing-mass peaks converge as the kaon spectrometer is moved farther away from parallel kinematics, as the widths of the data peaks increase more rapidly as a function of spectrometer angle than do

Table 5.1: Ratio of Hydrogen Λ data to SIMC in tail and peak regions (see Fig. 5.1).

setting	tail ratio 1.140–1.165 GeV	peak ratio 1.100–1.140 GeV
0	1.111	0.994
4	1.023	0.998
8	0.998	1.000
13	1.132	0.993
0l	1.045	0.997
4l	1.120	0.991
8l	1.029	0.997
13l	1.263	0.982
1	1.078	0.994
6	1.139	0.991
11	1.122	0.993
23	0.931	1.005
25	1.236	0.986
29	1.010	1.000
Average	1.088	0.994

the simulation peaks. The difference in hydrogen peak widths is irrelevant to the extraction of cross sections.

The simulation well reproduces the shape of the spectra, especially in the radiative tails region. Table 5.1 lists the ratios of data to SIMC in the peak region 1.100–1.140 GeV and in the radiative tail region 1.140–1.165 GeV. The average ratios of 0.994 in the peak region and 1.088 in the tail region demonstrate how well the simulation models the radiative tails. Also, the data and simulation for

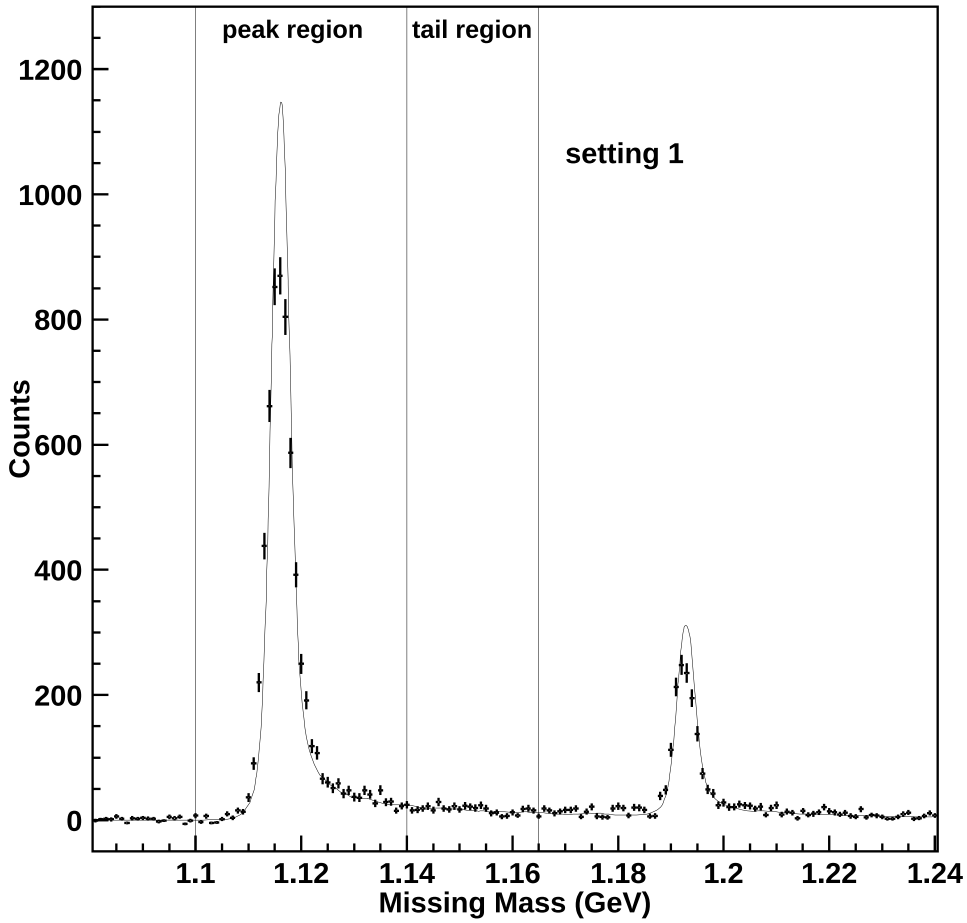

Figure 5.1: Hydrogen (e,e$'$K$^+$) for E_{beam}=3.245 GeV, Q^2=0.38 GeV^2, W=1.90 GeV, $\theta_{\gamma K(lab)}$=1.5°. The simulation is the solid line, the data are the crosses with statistical errors only. The comparison regions for Table 5.1 are delineated.

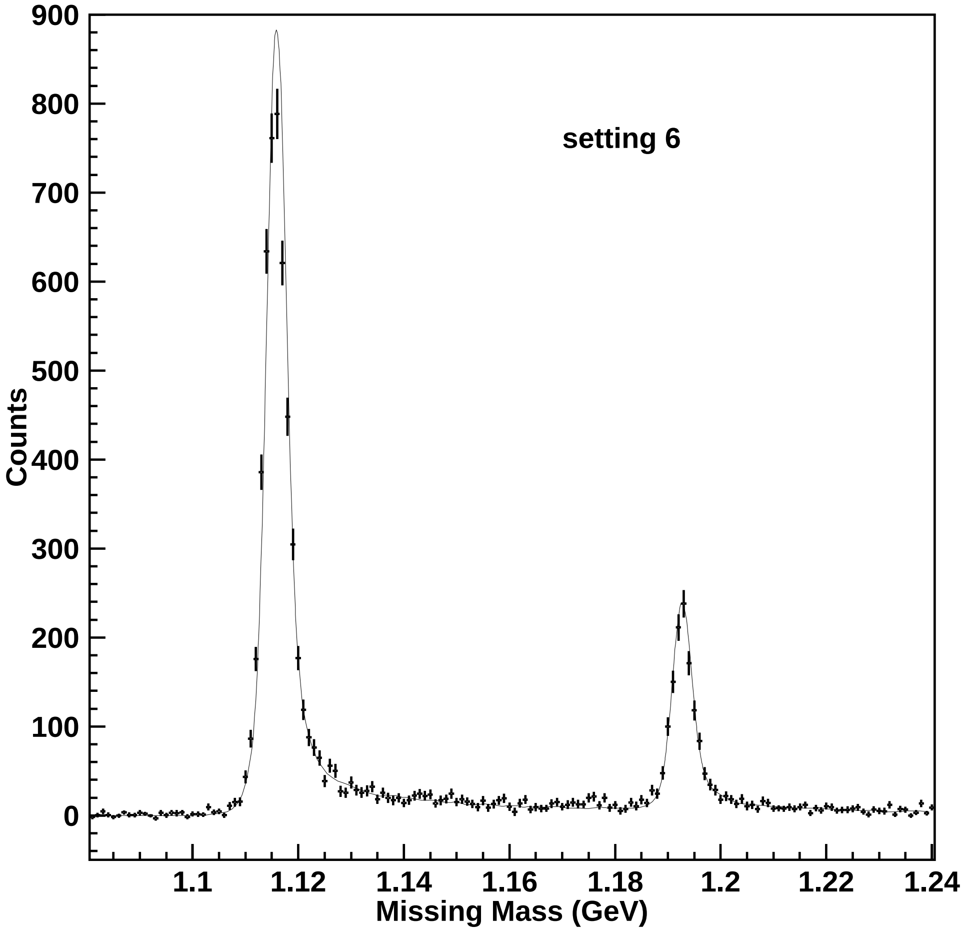

Figure 5.2: Hydrogen (e,e$'$K$^+$) for E_{beam}=3.245 GeV, Q^2=0.38 GeV^2, W=1.90 GeV, $\theta_{\gamma K(lab)}$=6.0°. The simulation is the solid line, the data are the crosses with statistical errors only.

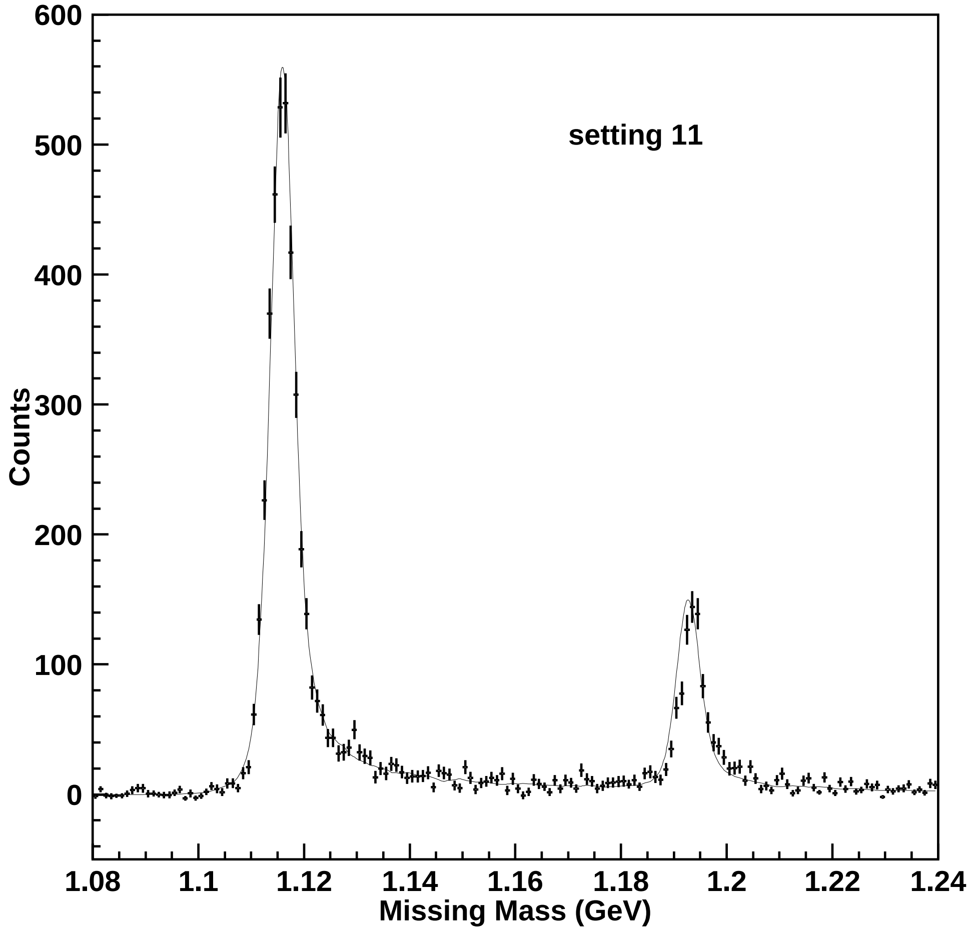

Figure 5.3: Hydrogen (e,e′K$^+$) for E_{beam}=3.245 GeV, Q^2=0.38 GeV^2, W=1.90 GeV, $\theta_{\gamma K(lab)}$=11.0°. The simulation is the solid line, the data are the crosses with statistical errors only.

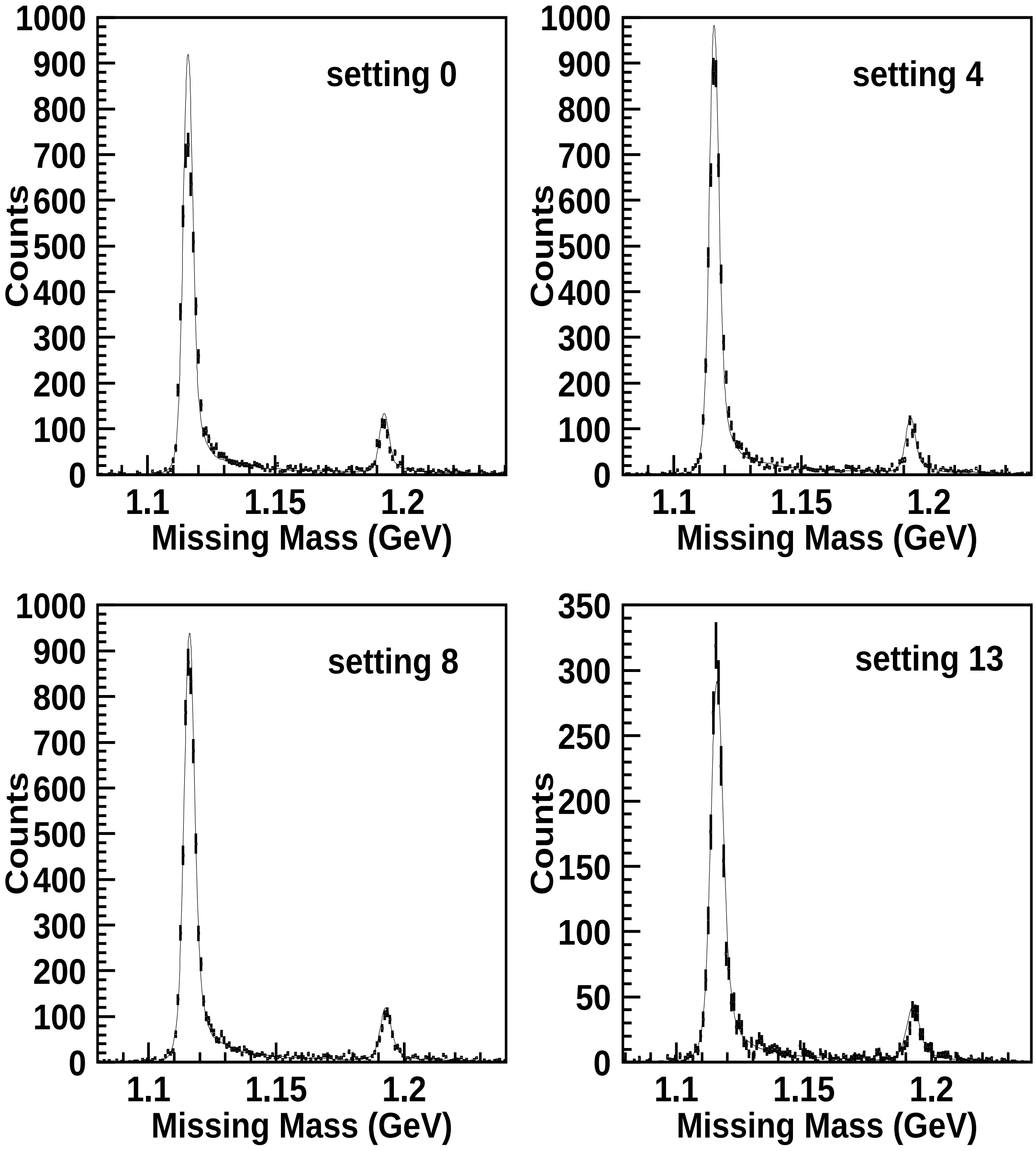

Figure 5.4: Hydrogen (e,e′K$^+$) for E_{beam}=3.245 GeV, Q^2=0.50 GeV^2, W=1.80 GeV, $\theta_{\gamma K(lab)}$=0.0, 4.3, 8.8, 13.3°. The simulation is the solid line, the data are the crosses with statistical errors only.

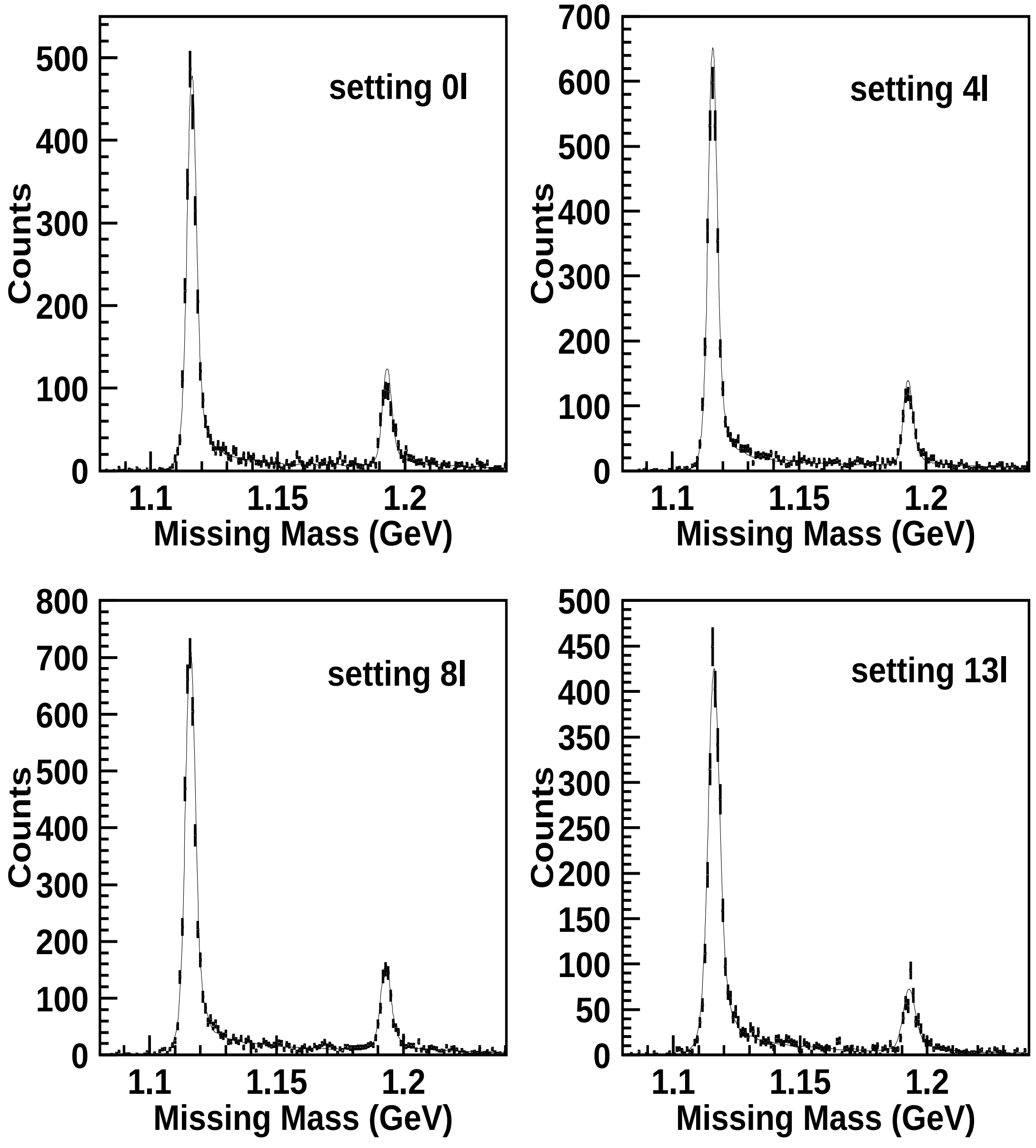

Figure 5.5: Hydrogen (e,e$'$K$^+$) for E_{beam}=3.245 GeV, Q^2=0.52 GeV^2, W=1.76 GeV, $\theta_{\gamma K(lab)}$=0.0, 4.3, 8.8, 13.3°. The simulation is the solid line, the data are the crosses with statistical errors only.

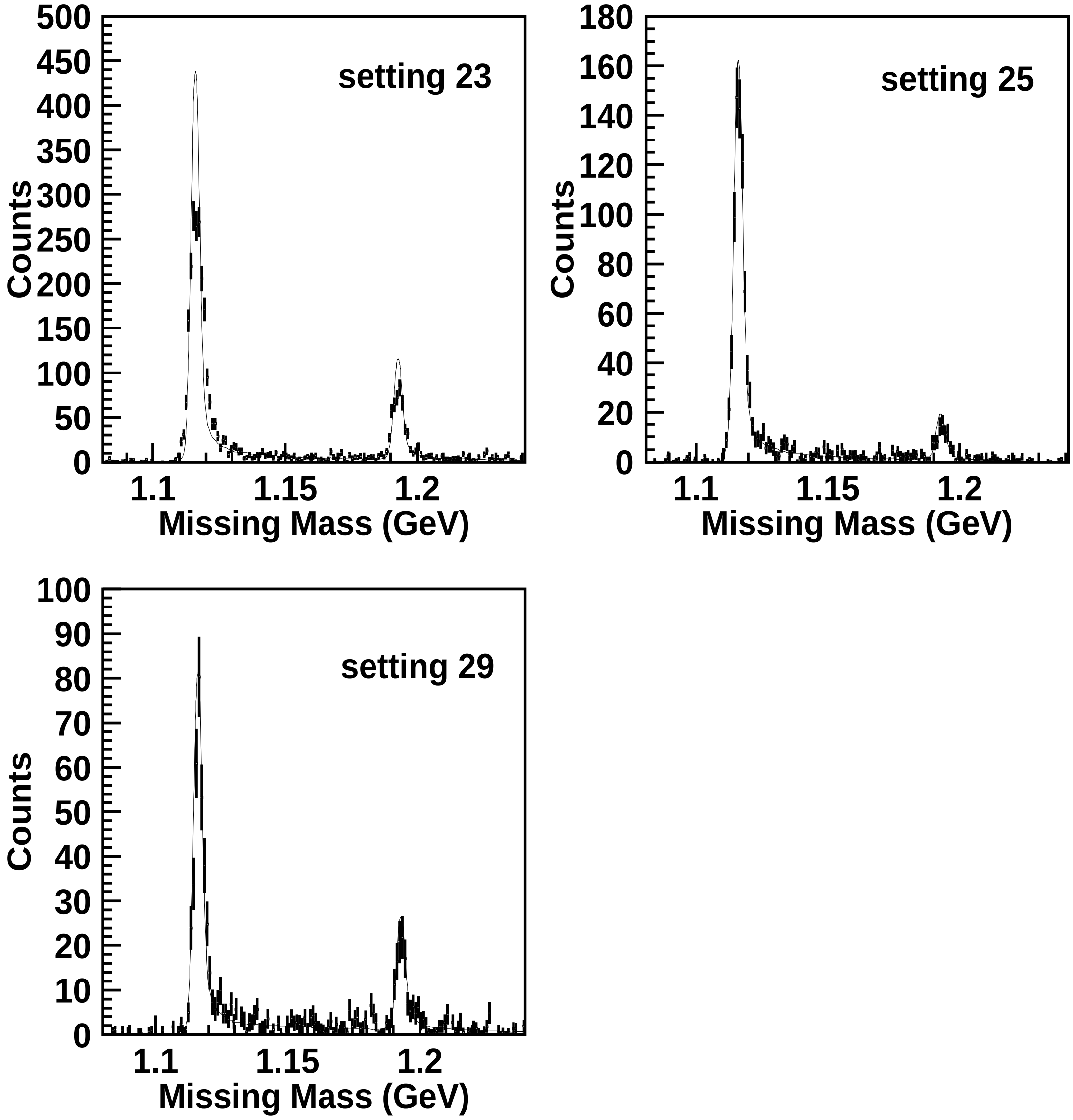

Figure 5.6: Hydrogen (e,e′K$^+$) for E_{beam}=2.445 GeV: Q^2=0.38 GeV^2, W=1.87 GeV, $\theta_{\gamma K(lab)}$=1.5° (setting 23); Q^2=0.50 GeV^2, W=1.80 GeV, $\theta_{\gamma K(lab)}$=1.0° (setting 25); and Q^2=0.52 GeV^2, W=1.78 GeV, $\theta_{\gamma K(lab)}$=1.0° (setting 29). The simulation is the solid line, the data are the crosses with statistical errors only.

all settings coincide on the missing-mass axis to within 1 MeV (in the Figures the data have been shifted by up to 1 MeV, the equivalent of one bin). This agreement is indicative that the energies, momenta, and offsets used in the analysis are accurate.

For each hydrogen setting, cross sections have been obtained for the entire acceptance and for bins in SOS delta. The bins used are -20% to -10%, -10% to 0%, 0% to 10%, and 10% to 20%. For each bin, average values of all kinematic quantities are calculated. The binned cross sections are listed in Tables 5.2–5.4, and the unbinned cross sections in Tables 5.5–5.6. Errors in the cross sections for Λ production are dominated by systematic uncertainties, whereas for Σ^0 production the statistical uncertainties can be as large as the systematic ones. Uncertainties related to using multiple physics cross-section parameterizations are listed in Table 5.7. The parameterizations will be explained below, but the extracted cross sections are independent (to within 1% for Λ production and to within 3% for Σ^0 production for most settings) of the parameterization used in the analysis.

The experimental cross sections for kaon electroproduction on hydrogen can be compared to the previous data shown in Figs. 1.5 and 1.6. The curves fit to the previous data predict a range of cross sections from 0.377–0.412 μb/sr for Λ production and 0.084–0.105 μb/sr for Σ^0 production over the Q^2 range 0.38–0.52 GeV^2. The cross sections at central settings (0l, 0, and 1) range from 0.416–

Table 5.2: Hydrogen Λ cross sections (binned). Angles are between the virtual photon and outgoing kaon. All ϕ distributions are peaked at 180° except the first three 0 settings (peaked at ±35°, ±50°, and ±140°, respectively), the first 4 setting (peaked at ±120°), the three 0l settings (peaked at 0°, ±40°, and ±80°, respectively), and the first 4l setting (peaked at ±150°). Cross sections are in the center-of-mass of the virtual photon-target nucleon system.

set-ting	W GeV	Q^2 GeV^2	θ_{cm} deg	ϵ	$\cos\phi$	$\cos 2\phi$	ϕ-range deg	$d\sigma/d\Omega$ μb/sr
0	1.736	0.542	11.04	0.821	0.589	0.101	-100–100	0.413±0.023
0	1.774	0.516	8.73	0.807	0.249	-0.093	full	0.413±0.021
0	1.824	0.485	8.16	0.788	-0.170	-0.107	full	0.407±0.020
0	1.864	0.461	8.76	0.770	-0.513	0.026	50–310	0.438±0.023
4	1.738	0.534	11.30	0.821	-0.510	-0.065	50–310	0.472±0.025
4	1.777	0.512	13.35	0.806	-0.729	0.242	90–270	0.440±0.022
4	1.828	0.487	16.53	0.786	-0.855	0.515	110–250	0.425±0.021
4	1.867	0.458	18.35	0.768	-0.903	0.652	120–240	0.396±0.022
8	1.743	0.531	23.15	0.819	-0.891	0.613	120–240	0.468±0.024
8	1.788	0.507	25.91	0.801	-0.925	0.722	130–230	0.424±0.021
8	1.841	0.480	29.28	0.779	-0.946	0.796	140–220	0.374±0.018
8	1.872	0.457	28.33	0.765	-0.956	0.830	140–220	0.309±0.023
13	1.759	0.520	36.68	0.813	-0.950	0.810	140–220	0.414±0.024
13	1.812	0.493	39.51	0.792	-0.962	0.850	150–210	0.312±0.017
13	1.857	0.469	40.49	0.772	-0.969	0.876	150–210	0.283±0.018
0l	1.724	0.553	12.87	0.823	0.679	0.197	-100–100	0.434±0.026
0l	1.756	0.522	9.56	0.815	0.415	-0.033	-150–150	0.434±0.023
0l	1.794	0.502	7.88	0.800	0.093	-0.181	full	0.429±0.023
4l	1.727	0.546	11.04	0.823	-0.368	-0.129	50–310	0.493±0.028
4l	1.757	0.519	12.08	0.814	-0.623	0.087	60–300	0.509±0.026
4l	1.800	0.498	14.20	0.799	-0.796	0.360	100–260	0.463±0.024
8l	1.731	0.543	22.86	0.822	-0.872	0.554	120–240	0.494±0.026
8l	1.767	0.517	24.51	0.810	-0.908	0.667	130–230	0.455±0.023
8l	1.813	0.493	27.24	0.792	-0.935	0.758	130–230	0.415±0.021
13l	1.743	0.529	36.35	0.819	-0.944	0.789	140–220	0.451±0.024
13l	1.787	0.509	38.09	0.803	-0.957	0.833	140–220	0.372±0.020
13l	1.836	0.487	40.80	0.781	-0.965	0.862	150–210	0.334±0.019

Table 5.3: Hydrogen Λ cross sections (binned). Angles are between the virtual photon and outgoing kaon. All ϕ distributions are peaked at 180° except the first two 1 settings (±50° and ±110°, respectively), the first 25 setting (flat distribution), and the first 29 setting (0°). Cross sections are in the center-of-mass of the virtual photon-target nucleon system.

set-ting	W GeV	Q^2 GeV^2	θ_{cm} deg	ϵ	$\cos\phi$	$\cos 2\phi$	ϕ-range deg	$d\sigma/d\Omega$ $\mu b/sr$
1	1.831	0.423	8.86	0.798	0.284	-0.084	-120–120	0.408±0.042
1	1.858	0.395	7.64	0.789	-0.047	-0.108	full	0.412±0.020
1	1.914	0.367	8.68	0.761	-0.480	0.041	40–320	0.408±0.020
1	1.955	0.349	9.81	0.739	-0.705	0.240	80–280	0.432±0.022
6	1.831	0.424	13.71	0.798	-0.755	0.282	100–260	0.462±0.040
6	1.862	0.392	15.01	0.787	-0.828	0.445	100–260	0.404±0.020
6	1.922	0.367	18.81	0.756	-0.905	0.662	120–240	0.401±0.019
6	1.960	0.345	19.26	0.736	-0.928	0.733	130–230	0.303±0.020
11	1.839	0.408	27.36	0.797	-0.929	0.737	130–230	0.317±0.020
11	1.879	0.386	29.06	0.777	-0.945	0.790	140–220	0.356±0.017
11	1.936	0.364	31.78	0.747	-0.958	0.838	140–220	0.324±0.017
23	1.836	0.404	6.25	0.602	-0.123	0.105	full	0.420±0.029
23	1.871	0.374	7.00	0.576	-0.439	0.197	full	0.406±0.021
23	1.904	0.348	7.67	0.548	-0.674	0.298	60–300	0.390±0.028
25	1.775	0.521	6.75	0.618	-0.023	0.087	full	0.386±0.027
25	1.820	0.482	7.52	0.588	-0.452	0.188	full	0.384±0.025
29	1.761	0.536	7.05	0.626	0.142	0.086	full	0.439±0.042
29	1.791	0.505	6.41	0.608	-0.209	0.047	full	0.416±0.032

Table 5.4: Hydrogen Σ^0 cross sections (binned). Angles are between the virtual photon and outgoing kaon. All ϕ distributions are peaked at 180° except the first two 0 settings (±100° and ±140°, respectively), the three 0l settings (±70°, ±120°, and ±140°, respectively), the first 4l setting (±130°), and the first 1 setting (±120°). Cross sections are in the center-of-mass of the virtual photon-target nucleon system.

set-ting	W GeV	Q^2 GeV^2	θ_{cm} deg	ϵ	$\cos\phi$	$\cos 2\phi$	ϕ-range deg	$d\sigma/d\Omega$ μb/sr
0	1.808	0.491	8.62	0.796	0.007	-0.164	full	0.074±0.008
0	1.847	0.476	9.09	0.779	-0.343	-0.049	full	0.110±0.009
0	1.875	0.445	9.64	0.767	-0.570	0.097	50–310	0.111±0.011
4	1.812	0.491	16.88	0.795	-0.832	0.449	100–260	0.087±0.009
4	1.851	0.475	19.37	0.776	-0.888	0.607	120–240	0.095±0.008
4	1.882	0.430	19.04	0.765	-0.915	0.694	130–230	0.134±0.016
8	1.825	0.488	30.80	0.789	-0.940	0.773	130–230	0.098±0.009
8	1.860	0.466	31.76	0.772	-0.951	0.815	140–220	0.112±0.009
13	1.843	0.474	44.54	0.779	-0.967	0.869	150–210	0.113±0.011
13	1.868	0.459	42.48	0.768	-0.972	0.888	150–210	0.150±0.017
0l	1.792	0.497	9.33	0.802	0.113	-0.130	full	0.056±0.008
0l	1.826	0.484	8.80	0.787	-0.184	-0.107	full	0.088±0.009
0l	1.863	0.456	9.20	0.772	-0.500	-0.009	50–310	0.105±0.010
4l	1.798	0.502	15.96	0.801	-0.777	0.321	90–270	0.064±0.008
4l	1.833	0.480	17.93	0.785	-0.858	0.519	110–250	0.094±0.010
4l	1.864	0.462	19.63	0.770	-0.905	0.660	120–240	0.112±0.011
8l	1.807	0.499	29.89	0.796	-0.930	0.741	130–230	0.086±0.010
8l	1.847	0.476	31.58	0.779	-0.947	0.798	140–220	0.115±0.012
8l	1.873	0.449	31.32	0.767	-0.958	0.840	140–220	0.134±0.016
13l	1.826	0.490	44.38	0.787	-0.944	0.859	150–210	0.092±0.010
13l	1.861	0.463	43.99	0.771	-0.957	0.879	150–210	0.102±0.011
1	1.871	0.385	7.79	0.784	-0.151	-0.125	full	0.107±0.008
1	1.922	0.364	9.17	0.759	-0.512	0.060	40–320	0.133±0.008
1	1.957	0.346	10.35	0.738	-0.715	0.253	80–280	0.142±0.011
6	1.877	0.385	16.64	0.781	-0.861	0.526	120–240	0.119±0.009
6	1.927	0.363	19.92	0.753	-0.908	0.671	120–240	0.132±0.008
6	1.962	0.342	19.57	0.735	-0.930	0.741	130–230	0.126±0.014
11	1.894	0.380	31.43	0.772	-0.949	0.807	140–220	0.136±0.010
11	1.943	0.356	33.16	0.746	-0.960	0.844	150–210	0.118±0.009
23	1.883	0.365	7.81	0.565	-0.549	0.248	full	0.122±0.010

Table 5.5: Hydrogen Λ cross sections. Angles are between the virtual photon and outgoing kaon. All ϕ distributions are peaked at 180° except the 0 and 29 settings (flat distributions) and the 0l setting (peaked at 0°). Cross sections are in the center-of-mass of the virtual photon-target nucleon system.

set-ting	W GeV	Q^2 GeV^2	θ_{cm} deg	ϵ	$\cos\phi$	$\cos 2\phi$	ϕ-range deg	$d\sigma/d\Omega$ μb/sr
0	1.798	0.500	8.980	0.796	0.014	-0.036	full	0.416±0.020
4	1.794	0.503	14.670	0.797	-0.748	0.324	100–260	0.437±0.020
8	1.796	0.501	26.460	0.796	-0.925	0.725	130–230	0.413±0.019
13	1.801	0.499	38.750	0.794	-0.959	0.842	150–210	0.341±0.017
0l	1.757	0.524	9.790	0.811	0.359	-0.031	full	0.429±0.021
4l	1.757	0.524	12.580	0.811	-0.620	0.129	70–290	0.490±0.023
8l	1.764	0.520	24.690	0.808	-0.906	0.663	130–230	0.454±0.021
13l	1.774	0.515	38.160	0.804	-0.953	0.820	140–220	0.394±0.019
1	1.896	0.376	8.530	0.768	-0.349	0.022	full	0.417±0.019
6	1.894	0.379	17.090	0.768	-0.870	0.565	120–240	0.395±0.018
11	1.893	0.381	29.810	0.769	-0.948	0.801	140–220	0.342±0.016
23	1.866	0.376	6.960	0.576	-0.417	0.195	full	0.406±0.020
25	1.797	0.500	7.190	0.601	-0.258	0.146	full	0.378±0.022
29	1.781	0.516	6.660	0.604	-0.085	0.061	full	0.425±0.029

Table 5.6: Hydrogen Σ^0 cross sections. Angles are between the virtual photon and outgoing kaon. All ϕ distributions are peaked at 180°. Cross sections are in the center-of-mass of the virtual photon-target nucleon system.

set- ting	W GeV	Q^2 GeV^2	θ_{cm} deg	ϵ	$\cos\phi$	$\cos 2\phi$	ϕ-range deg	$d\sigma/d\Omega$ $\mu b/sr$
0	1.836	0.478	9.070	0.781	-0.293	-0.049	full	0.096±0.007
4	1.837	0.477	18.530	0.781	-0.874	0.568	120–240	0.093±0.007
8	1.841	0.475	31.290	0.779	-0.947	0.798	140–220	0.102±0.007
13	1.848	0.471	43.860	0.776	-0.968	0.876	150–210	0.122±0.010
0l	1.815	0.489	9.310	0.789	-0.140	-0.074	full	0.074±0.006
4l	1.817	0.488	17.440	0.789	-0.826	0.457	100–260	0.076±0.006
8l	1.821	0.486	30.600	0.787	-0.939	0.770	140–220	0.092±0.009
13l	1.827	0.483	44.070	0.784	-0.965	0.862	150–210	0.085±0.008
1	1.909	0.369	8.980	0.762	-0.441	0.042	full	0.125±0.007
6	1.910	0.371	18.740	0.761	-0.894	0.628	120–240	0.125±0.007
11	1.916	0.368	32.310	0.758	-0.955	0.826	140–220	0.123±0.008
23	1.870	0.373	7.400	0.574	-0.448	0.204	full	0.109±0.008
25	1.817	0.482	7.940	0.589	-0.446	0.174	full	0.069±0.010
29	1.806	0.493	8.030	0.598	-0.320	0.166	full	0.076±0.011

Table 5.7: Cross section parameterization uncertainties for hydrogen.

setting	Λ error (%)	Σ error (%)
0	0.80	2.20
4	0.55	2.90
8	0.55	3.00
13	0.85	2.75
0l	0.60	2.95
4l	0.40	4.80
8l	0.35	6.75
13l	1.20	4.75
1	0.30	0.90
6	0.25	1.10
11	0.25	3.10
23	0.40	1.80
25	0.30	3.60
29	1.40	5.30

0.429 μb/sr for Λ production and 0.074–0.125 μb/sr for Σ^0 production. The cross sections are certainly consistent in magnitude with the previous data.

Jefferson Lab Experiment E93-018 obtained data during the fall of 1996 (as did this experiment) and had as its goal the extraction of a longitudinal/transverse cross-section separation for kaon electroproduction on hydrogen over a Q^2 range from 0.50–2.00 GeV^2. Data taken at the lowest Q^2 setting had nearly the same set of average values for kinematic quantities as our setting 0. That Λ cross section was found to be around 0.500 μb/sr [Nic98a],[Nic98b], 20% higher than the cross section listed for our experiment in Table 5.5. However, an independent analysis of the E93-018 data [Moh99] has not been able to reproduce the results in [Nic98a], and finds cross sections corresponding with setting 0 that are consistent with the value found here. Also, [Moh99] has looked at the setting 0 data for our experiment and extracted a cross section within 3% of our value. In addition, an independent analysis of the E91-016 data [Cha99a] has found Λ cross sections for hydrogen consistent with the cross sections given here.

5.1.2 Cross-Section Parameterization

The cross sections have also been compared to theoretical predictions based on the SL model [Dav96] discussed in Chapter 1 (note that in all the analysis that follows, the E_{beam}=2.445 GeV settings have not been included unless explicitly stated). In the simulation, each event was assigned a cross-section weight as a function of W, Q^2, and θ_{cm} by interpolating to a table of theoretical cross sections. Data and theory results are displayed in Figs. 5.7 and 5.8. Looking at the Σ^0 data first, there is a fairly good agreement between data and theory, both in overall normalization and dependence on W/Q^2 (meaning W and/or Q^2, not W divided by Q^2). The ratios at the same angle but different W and Q^2 overlap over the entire angular range. This agreement suggests that the SL model does well in describing all but the angular dependence of the Σ^0 data. At the same time, the SL model does a very poor job of predicting the W/Q^2 dependence of Λ cross sections. The dependence of the experimental to theoretical cross-section ratio on W/Q^2 is striking. The angular dependence is also not well modeled. It is not necessarily surprising that the model does poorly considering that there have been no previous electroproduction data in this kinematic region. At the same time, the disagreement is a warning that the cross-section dependences should not be assumed, but rather they need to be extracted from the data.

The binned hydrogen cross sections are used to obtain parameterizations for the cross-section dependence. To compare data points at different kinematic values, cross sections are divided by the phase space factor $p_{k(cm)}/p_{\gamma(cm)}$. This phase space factor is not an exact factor used by theoretical models, since different models include different factors in the amplitudes. For example, the SL model uses the

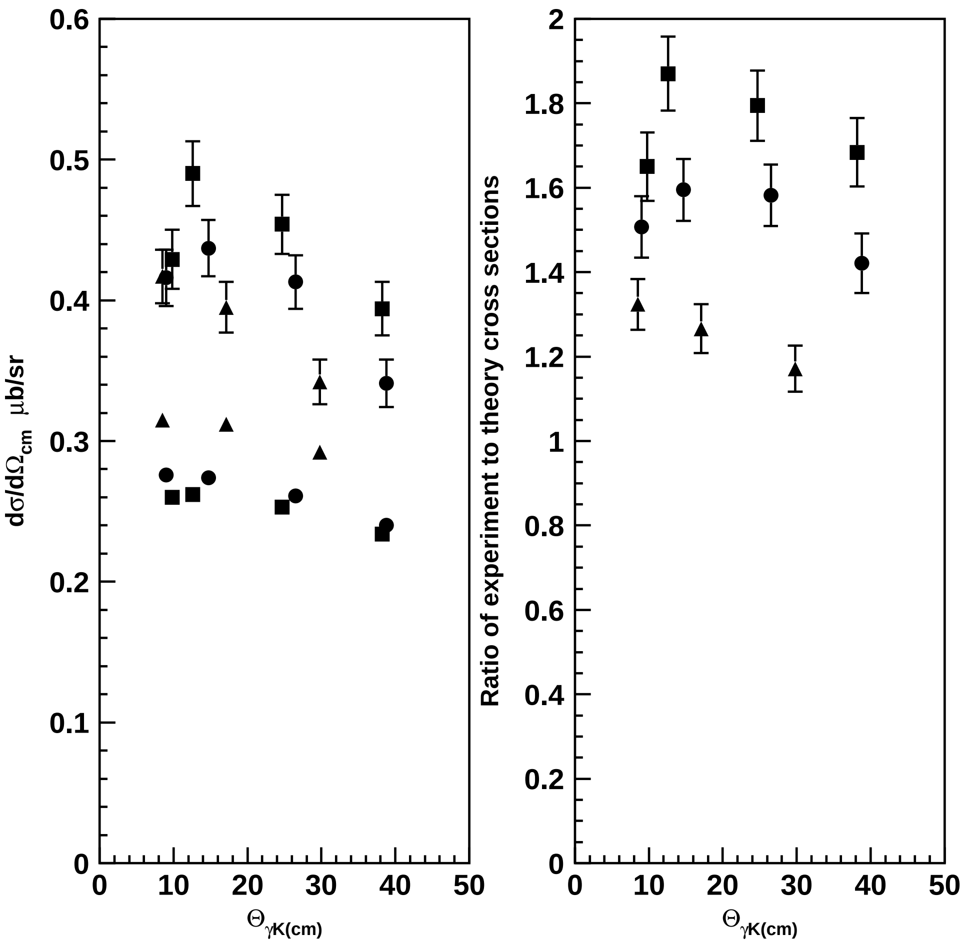

Figure 5.7: Hydrogen (e,e$'$K$^+$)Λ experimental and theoretical cross sections. The experimental points have error bars. Theory is derived from a Saclay model [Dav96]. On the right is the ratio of cross sections, with no error assigned to the theoretical numbers. The symbols used here and in the rest of the paper are triangles for the Q^2=0.38 GeV^2 points (settings 1, 6, 11), circles for the Q^2=0.50 GeV^2 points (settings 0, 4, 8, 13), and squares for the Q^2=0.52 GeV^2 points (settings 0l, 4l, 8l, 13l).

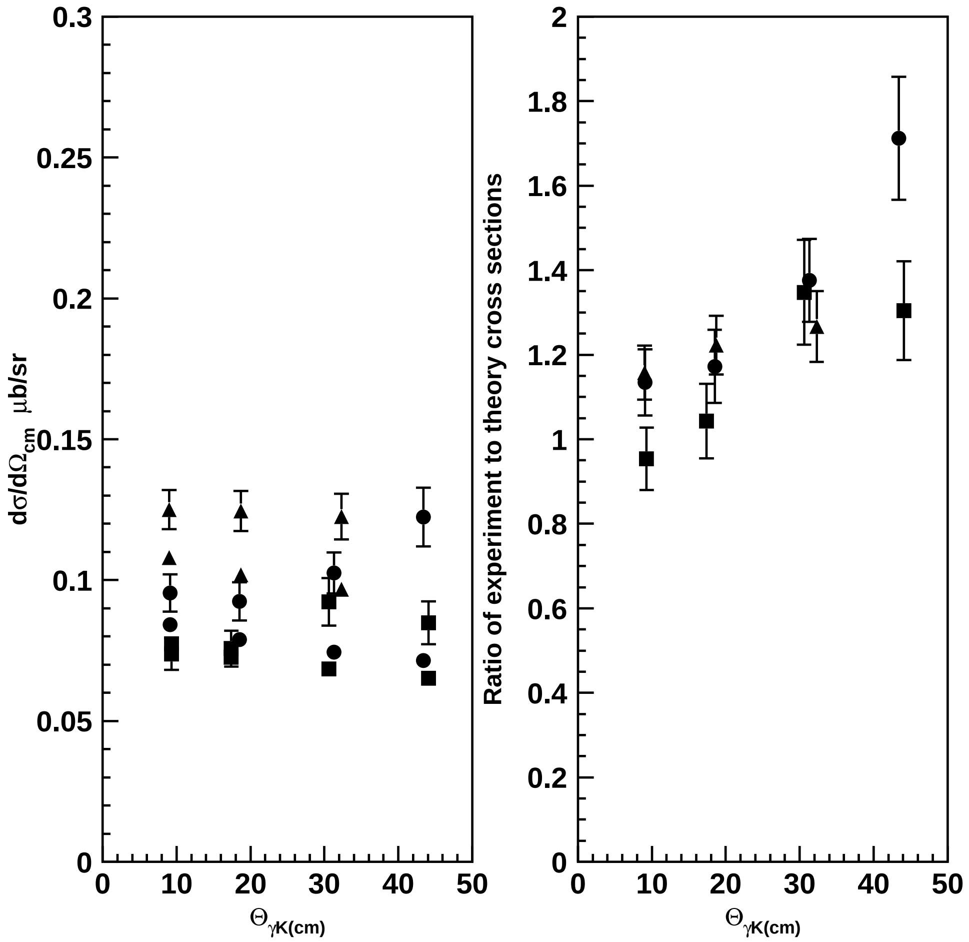

Figure 5.8: Hydrogen (e,e′K$^+$)Σ^0 experimental and theoretical cross sections. The experimental points have error bars. Theory is derived from a Saclay model [Dav96]. On the right is the ratio of cross sections, with no error assigned to the theoretical numbers.

phase space factor [Dav96],

$$\text{phsp} = \frac{p_{k(cm)}(E_p + M_p)(E_Y + M_Y)}{2W(W^2 - M_p^2)}, \tag{5.1}$$

while the WJC model [Wil92] uses

$$\text{phsp} = \frac{p_{k(cm)}}{p_{\gamma(cm)}} \frac{M_p M_Y}{16\pi^2 W^2}. \tag{5.2}$$

The differences between phase space factors are not important when it comes to calculating a parameterization, although certainly one expects that only by using a correct phase space factor will one see correlations between data points at different settings. The results of dividing the data by this factor are seen in Figs. 5.9 and 5.10.

The functional form used to fit the data is the sum of a constant and a term that looks like a resonance. The resonance term was chosen because the nature of the poor agreement of data and theory led to the suspicion that resonances make a significant contribution to the Λ cross section at low W. The fact that the Λ data are well-fitted to a resonance (the $S_{11}(1650)$, width 150 MeV) serves to reinforce that suspicion, although the results of the fit should not be interpreted as the relative contributions of resonant and non-resonant terms. A fit to the full set of data can be seen in the upper left-hand corner of Fig. 5.9. The remaining plots show fits to data points grouped by θ_{cm}, and these fits describe the data much better than the fit to the full set. A large variation in the ratio of resonant multiplicative

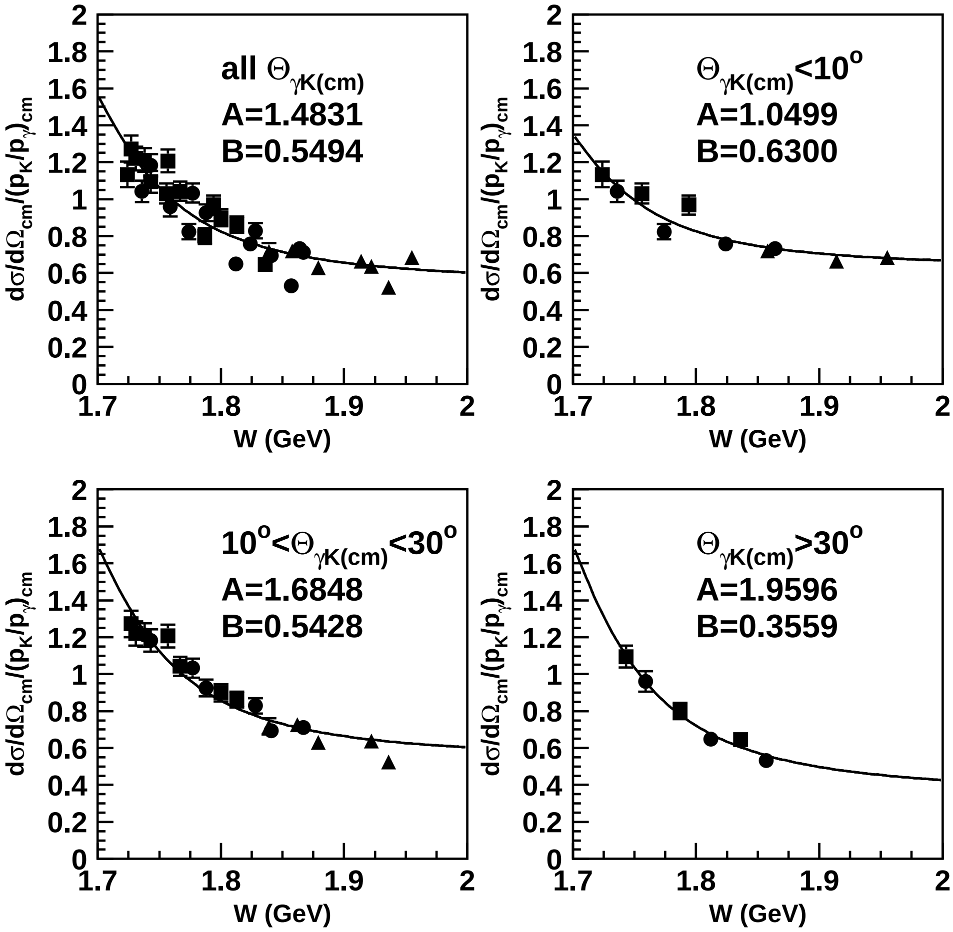

Figure 5.9: Hydrogen (e,e′K$^+$)Λ W–parameterizations. Cross sections have been scaled by $p_{k(cm)}/p_{\gamma(cm)}$. The general form for the parameterization is A(1.65^2)(0.15^2)/((W^2-1.65^2)^2 +(1.65^2)(0.15^2))+B.

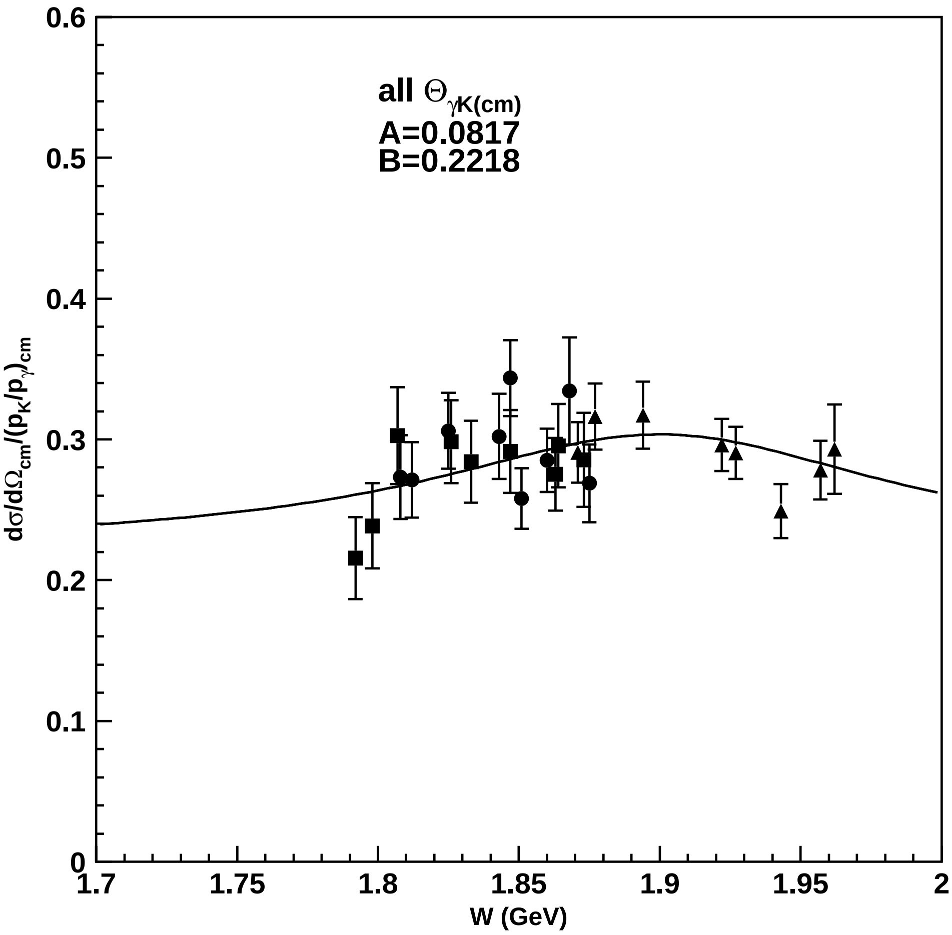

Figure 5.10: Hydrogen (e,e′K$^+$)Σ^0 W–parameterization. Cross sections have been scaled by $p_{k(cm)}/p_{\gamma(cm)}$. The general form for the parameterization is A(1.90^2)(0.20^2)/((W^2-1.90^2)^2 +(1.90^2)(0.20^2))+B.

factor to constant term can be seen as θ_{cm} varies. This variation could be indicative of the t-channel contribution being strongest at small angles, and the s-channel (resonance) contributions becoming more dominant with increasing angle. In the analysis these three fits to the angle-grouped Λ data were used to parameterize the physics cross section. To calculate the uncertainty in cross sections due to the parameterization chosen, cross sections were calculated using the fit to the full set of data as well as using a parameterization where the resonant term was zero, leaving only a constant term. Clearly the Λ data in Fig. 5.9 cannot be well-fitted to a straight line. The fact that the same cross sections are extracted when using just a constant and when using a precise parameterization indicate the robustness of the procedure.

The Σ^0 data was also fitted using this same functional form, in this case using the Δ $S_{31}(1900)$ (width 200 MeV) resonance. The resonant contribution is quite small, and the data could be described reasonably well by fitting the data to a straight line. For the analysis the fit shown in Fig. 5.10 was used. In calculating the parameterization uncertainty, cross sections were calculated using both a constant with no resonant term as well as with linear fits to data points from each individual setting. Once again the use of different parameterizations does not lead to significantly different extracted cross sections.

These parameterizations are used to weight all the events in the simulation.

To extract cross sections the average value of the event parameterization is computed, and that value times the scaling factor needed to match the simulation with the data gives the cross section. The parameterization is not hard-wired into the simulation (instead, it is applied to the ntuple created by SIMC), making it easy to evaluate different parameterizations. There is marked improvement in the agreement of the Λ data and simulation reconstructed quantities using an accurate parameterization, especially for the SOS delta spectra. This improvement is further justification that using this parameterization for the physics cross-section weight is both valid and necessary.

5.1.3 Angular Dependence

To extract a true W-dependence of the Λ and Σ^0 cross sections, more care is required. First, all the angular dependences need to be removed. The three groups of data taken at E_{beam}=3.245 GeV have essentially the same average W and Q^2 for all angular settings. Consequently, differences in cross sections within groups are dependent only on θ_{cm} and ϕ. Fig. 5.11 shows the angular cross-section distributions as a function of $\cos\theta_{cm}$ as well as fits to those points.

The parameterization used [(A+B$\sin\theta\cos\phi$+C$\sin^2\theta\cos 2\phi$)$\cos\theta$] is patterned on the formula for the cross section in terms of the transverse, longitudinal, and interference terms in Chapter 1. It should be noted that the settings closest to 0°

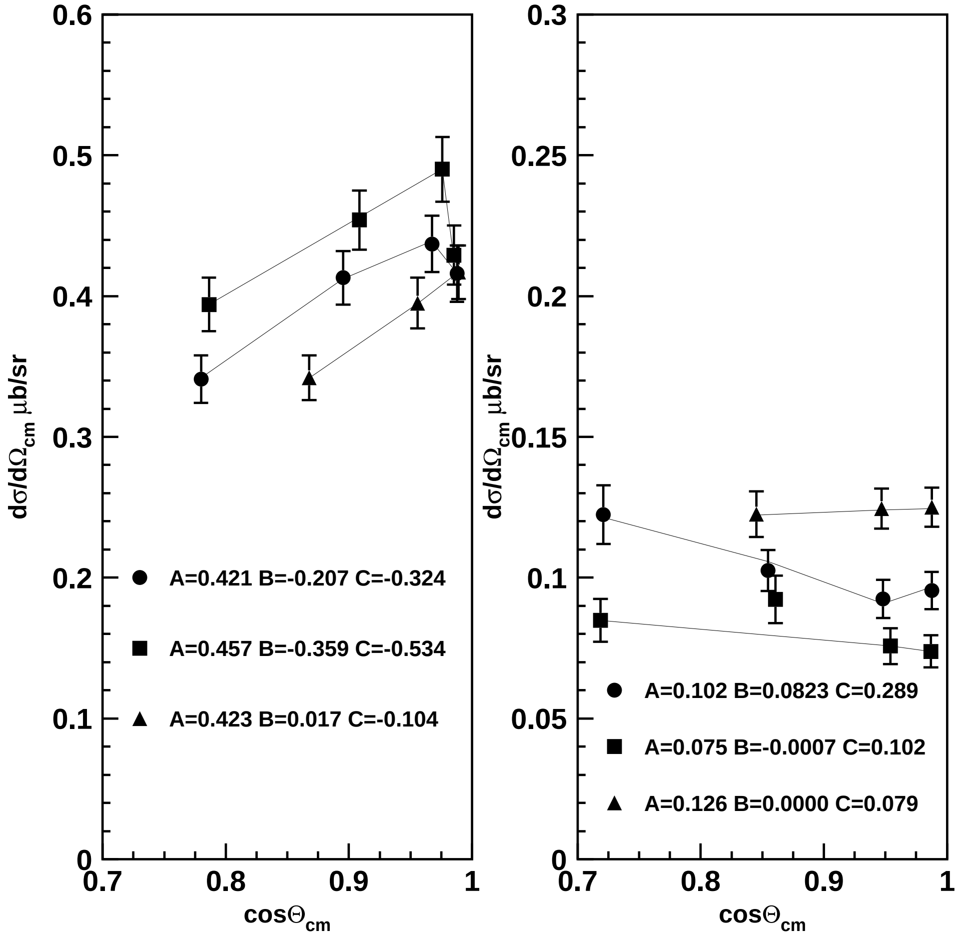

Figure 5.11: Hydrogen (e,e$'$K$^+$)Λ,Σ^0 angular parameterizations. The lines are fitted to the data points using the parameterization (A+B$\sin\theta\cos\phi$+C$\sin^2\theta$ $\cos 2\phi$)$\cos\theta$. The point corresponding to setting 8l has been left out of both fits.

for each group have full coverage in ϕ, while the other angular settings are peaked at 180°. There are no contributions from interference terms when there is full coverage in ϕ. Therefore, the high-Q^2 settings have an increase in Λ cross section from 0 and 0l to 4 and 4l due to the positive contribution of interference terms. The $B\sin\theta\cos\phi$ term must be the dominant interference term at these settings since $\cos\phi$ changes rapidly from 0 to 4, whereas $\cos 2\phi$ has a larger increase from 4 to 8 than from 0 to 4. The total interference strength can be estimated by comparing the cross section to $A\cos\theta$. From setting 0 to setting 4 the interference term contribution is equal to $-0.040\cos\phi$ μb/sr, and from setting 0l to setting 4l the contribution is $-0.063\cos\phi$ μb/sr. The low-Q^2 settings appear to have no significant interference contribution. The implication is that the contribution of interference terms turns on as W goes to 1.80 GeV and below.

The overall trend of the Λ data is for the cross section to decrease steadily with decreasing $\cos\theta_{cm}$, suggesting contributions from p- and/or d-waves. At the same time, the Σ^0 data show a lack of dependence on $\cos\theta_{cm}$, although there is possibly a slight increase in cross section with decreasing $\cos\theta_{cm}$. This flat distribution would indicate the cross section is dominated by s-wave. Of course, this experiment only probes a small range in $\cos\theta_{cm}$, limiting what can be learned in the study of angular dependences about the production mechanisms. The parameterizations of the angular dependences should not be taken too seriously since they are 3-

parameter fits to 3 or 4 data points. However, it is reasonable to believe that these parameterizations are decent fits to the data and can be used to extrapolate to θ_{cm}=0° and cos ϕ=0.

5.1.4 Dependences on W/Q^2

Once the angular dependences are understood only the W and Q^2 dependences remain. Since W and Q^2 are highly correlated an assumption has to be made concerning the nature of one of the dependences in order to reach a conclusion on the other. The assumption made here is that the Q^2 dependence is that derived by Bebek [Beb77] displayed in Figs. 1.5 and 1.6. One reason this assumption is made is because we want to test the assumption Bebek made about the W-dependence of the cross section as mentioned in Chapter 1, $\frac{d\sigma}{d\Omega} = \frac{|p_k^*|}{(W^2-M^2)W}|ME|^2$. Bebek derived his Q^2 dependences after scaling all data points to the same W using $\frac{|p_k^*|}{(W^2-M^2)W}$ as the scaling function. It is therefore appropriate to use Bebek's Q^2 dependences to see if we extract the same W-dependence. The binned data after having been scaled to Q^2=0.50 GeV^2, θ_{cm}=0°, and cos ϕ=0 are shown in Fig. 5.12. The overlap of the different sets of data after applying these scaling factors is a strong argument for the validity of the scaling factors.

The solid curves in this figure are the function $\frac{\mathrm{A}|p_k^*|}{(W^2-M^2)W}$ where A is allowed to vary to fit the data above W=1.81 GeV. For Λ production, A$_\Lambda$=4.1959 GeV$^2\mu$b/sr;

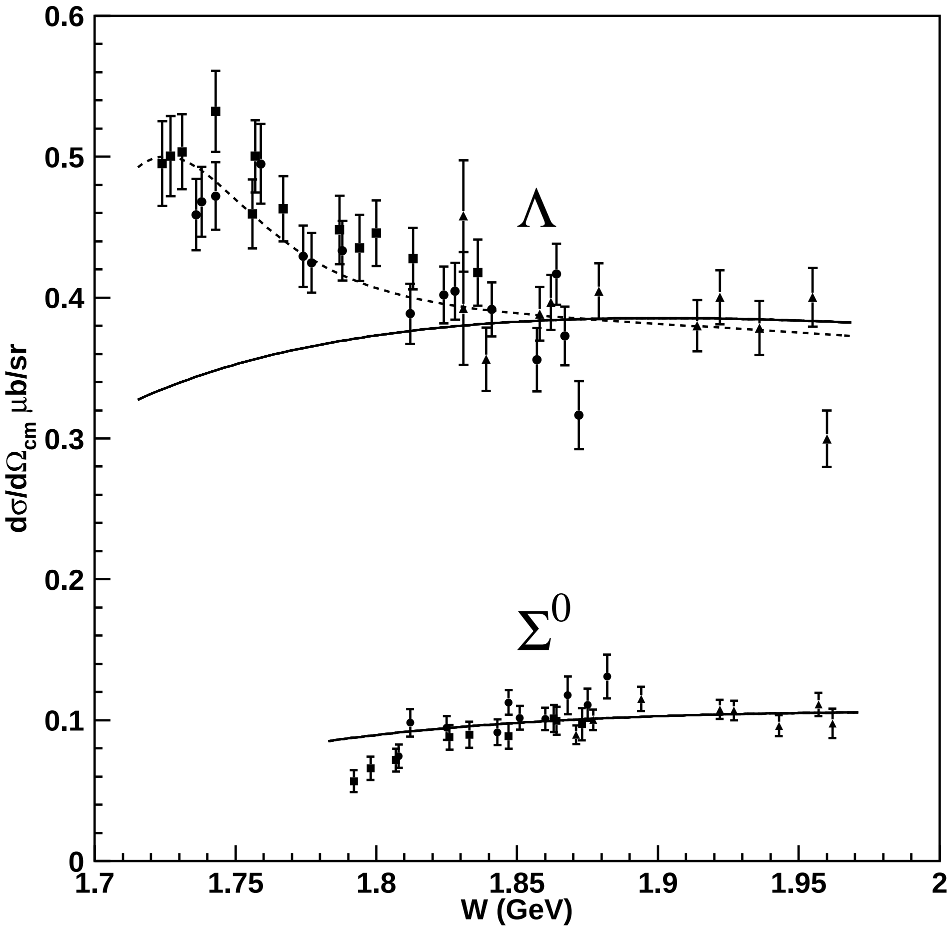

Figure 5.12: W-dependence of Λ and Σ^0 cross sections on hydrogen. The data are scaled in $\theta_{\gamma K(cm)}$, $\phi_{\gamma K}$, and Q^2 as described in the text. The curves are explained in the text. The solid curves are fit to the data above W=1.81 GeV.

for Σ^0 production, A_{Σ^0}=1.3176 GeV$^2\mu$b/sr. These curves fit the data well in this region, but below W=1.81 GeV they can no longer describe the data, neither for Λ nor Σ^0 production. The Λ data have been roughly fitted to the functional form $\frac{A|p_k^*|}{(W^2-M^2)W} + \frac{B(W_R^2)(D_R^2)}{(W^2-W_R^2)^2+(W_R^2)(D_R^2)}$, where A=0.959$A_\Lambda$, B=0.180 GeV$^2\mu$b/sr, W_R=1.72 GeV, and D_R=0.10 GeV (the dotted curve in Fig. 5.12). There are not enough data points below 1.81 GeV to fit a similar curve to the Σ^0 data, and the average W values listed in Table 5.6 are all greater than 1.805 GeV, so the curve fit to the data above 1.81 GeV is used to describe the Σ^0 W-dependence.

The deviations are indicators that kaon electroproduction becomes more complex as threshold and the resonances near threshold are approached. The N* resonances around 1.70 GeV are likely to be making a strong contribution to the Λ cross section below W=1.81 GeV and could also be the cause for what appears to be destructive interference in the Σ^0 cross section over the same W-range. At the same time, the W-dependence suggests that the Δ resonances near 1.90 GeV might not play as strong a role in Σ^0 production as was previously believed. To make further statements about the implications of the hydrogen data is difficult without the assistance of theoretical calculations. This set of data needs to be used to create new phenomenological models that will have new strengths for coupling constants. Perhaps certain theories will be unable to fit the data and will need to be discarded. It is unfortunate that there are not yet theoretical calculations using this data, but in the near future a number of new theoretical analyses will be conducted based on this data.

Once the W-dependence is understood, the data can be looked at as functions of Q^2 or θ_{cm} at a common W (1.85 GeV). The angular dependence data are scaled to Q^2=0.50 GeV^2 as before. In addition, the Λ ϕ-dependence can be dealt with using the interference term contributions previously derived ($-0.063 \cos\phi$ μb/sr for settings 0l, 4l, 8l, and 13l, $-0.040 \cos\phi$ μb/sr for settings 0, 4, 8, and 13, and no contribution for settings 1, 6, and 11), see Fig. 5.13.

The Q^2 data (Fig. 5.14) are scaled to θ_{cm}=0° and $\cos\phi$=0 as before. The dipole parameterizations used to describe the previous data fit this data fairly well. The constants are slightly different than the ones in Figs. 1.5 and 1.6 (2% larger for Λ and 11% smaller for Σ^0), and scaling to W=2.15 GeV using the Bebek formalism [Beb77] would decrease the Λ constant by 7% and increase the Σ^0 constant by 7%.

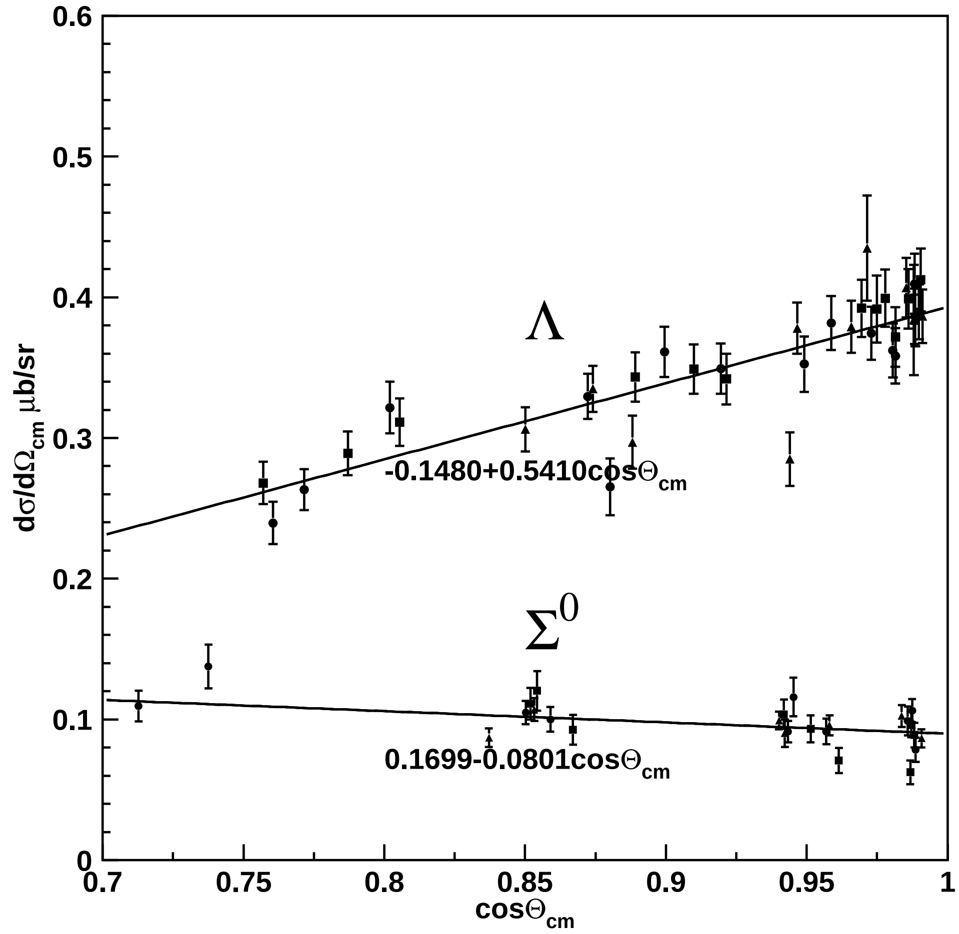

Figure 5.13: Angular dependence of Λ and Σ^0 cross sections on hydrogen. The data are scaled in W, $\phi_{\gamma K}$, and Q^2 as described in the text. The curves are fits to the data.

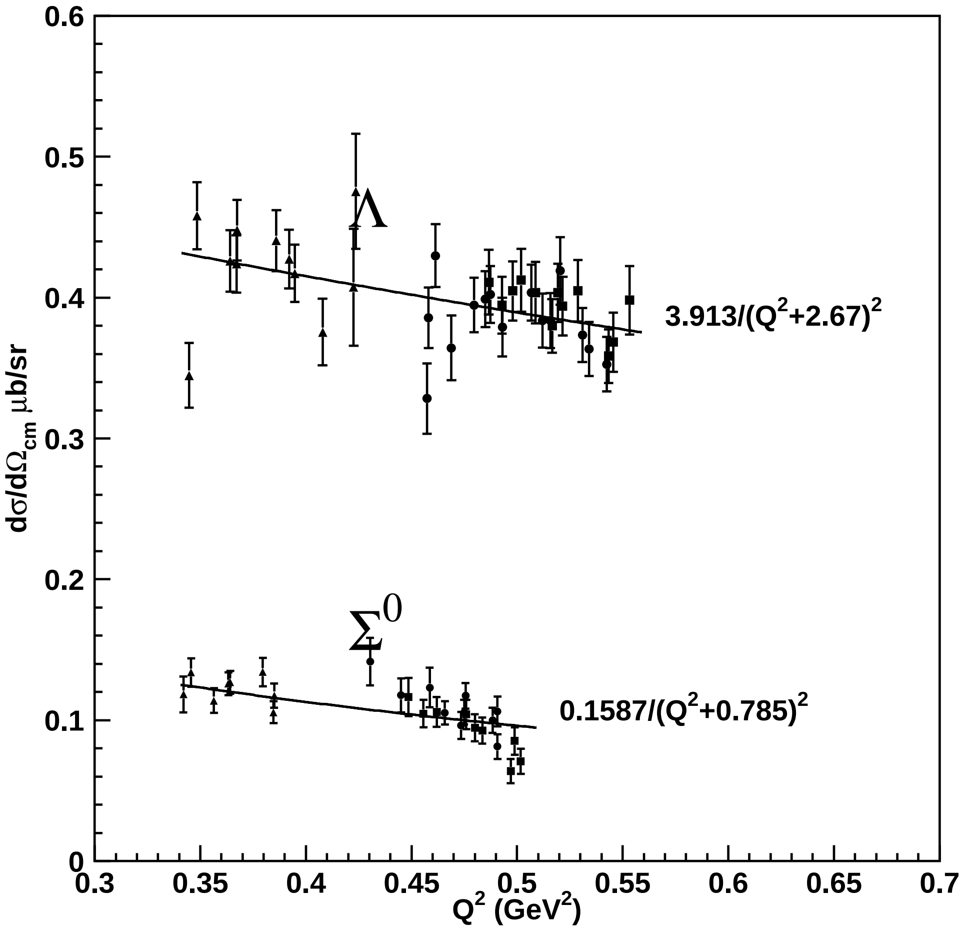

Figure 5.14: Q^2-dependence of Λ and Σ^0 cross sections on hydrogen. The data are scaled in $\theta_{\gamma K(cm)}$, $\phi_{\gamma K}$, and W as described in the text. The curves are fits to the data.

5.2 Deuterium

5.2.1 Missing-Mass Spectra

With an understanding of the hydrogen data, it is now possible to interpret the deuterium data with some degree of confidence. Missing-mass spectra are shown in Figs. 5.15–5.20. The position of the missing-mass peaks move from setting to setting for several reasons. Missing mass is the invariant mass of the residual hyperon-plus-nucleon system. If $\theta_{\gamma K}$ increases, the angle between the hyperon and nucleon will also increase, and the energy of the YN system must also increase. Also, increasing the momentum of the recoil hyperon will also increase the energy of the YN system. A plot of missing-mass peak for the Λ with the target nucleon at rest as a function of the Λ momentum is displayed in Fig. 5.21. In general, hyperon momentum increases as Q^2 increases but decreases as W increases.

Displayed along with the data are MINUIT fits of the simulation. The MINUIT fits determined the scaling factors for the Λ and Σ^- curves that minimized χ^2 over the missing-mass range 2.010–2.290 GeV. The simulation curves were also moved independently along the missing-mass axis until the offsets that corresponded to the minimum χ^2 were found (the Λ and the Σ curves were allowed to have different offsets). Cross-section uncertainties given by the MINUIT fits were on the order of 1% for Λ, 5% for Σ^- at the low-Q^2 settings, 10–20% for Σ^- at the 0, 4, and 8

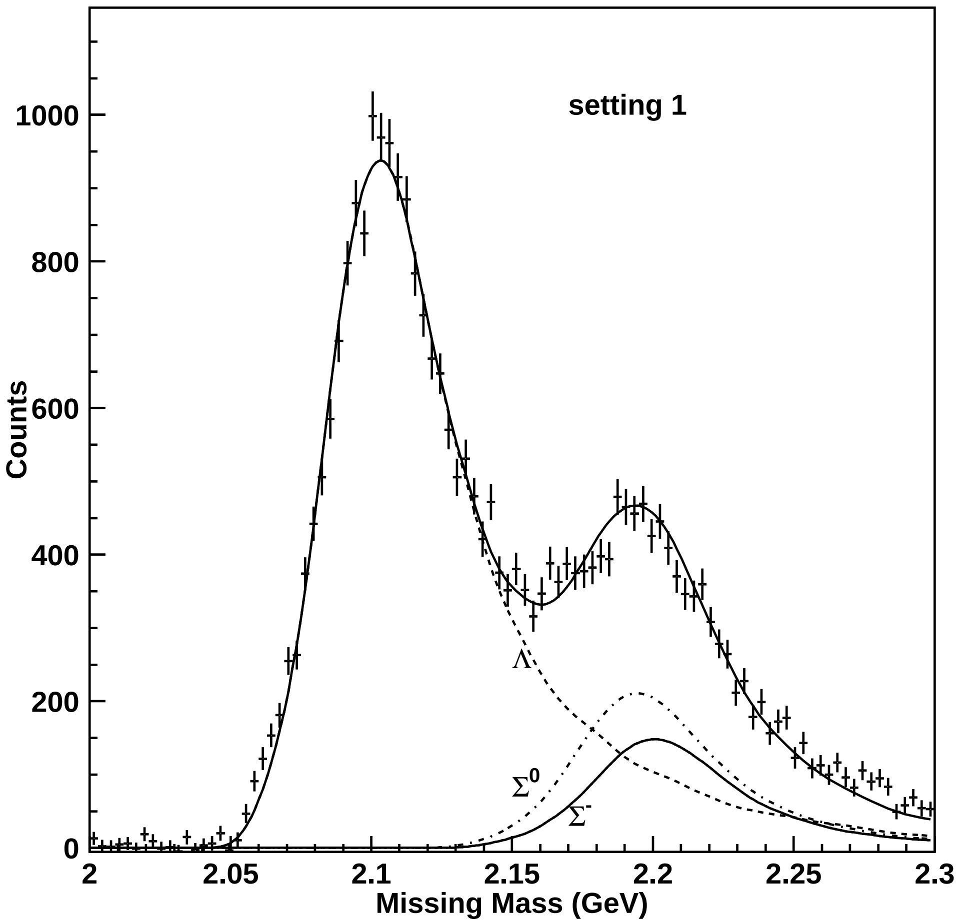

Figure 5.15: Deuterium (e,e′K$^+$) for E$_{beam}$=3.245 GeV, Q^2=0.38 GeV^2, W=1.90 GeV, $\theta_{\gamma K(lab)}$=1.5°. The simulation is the solid lines, the data are the crosses with statistical errors only.

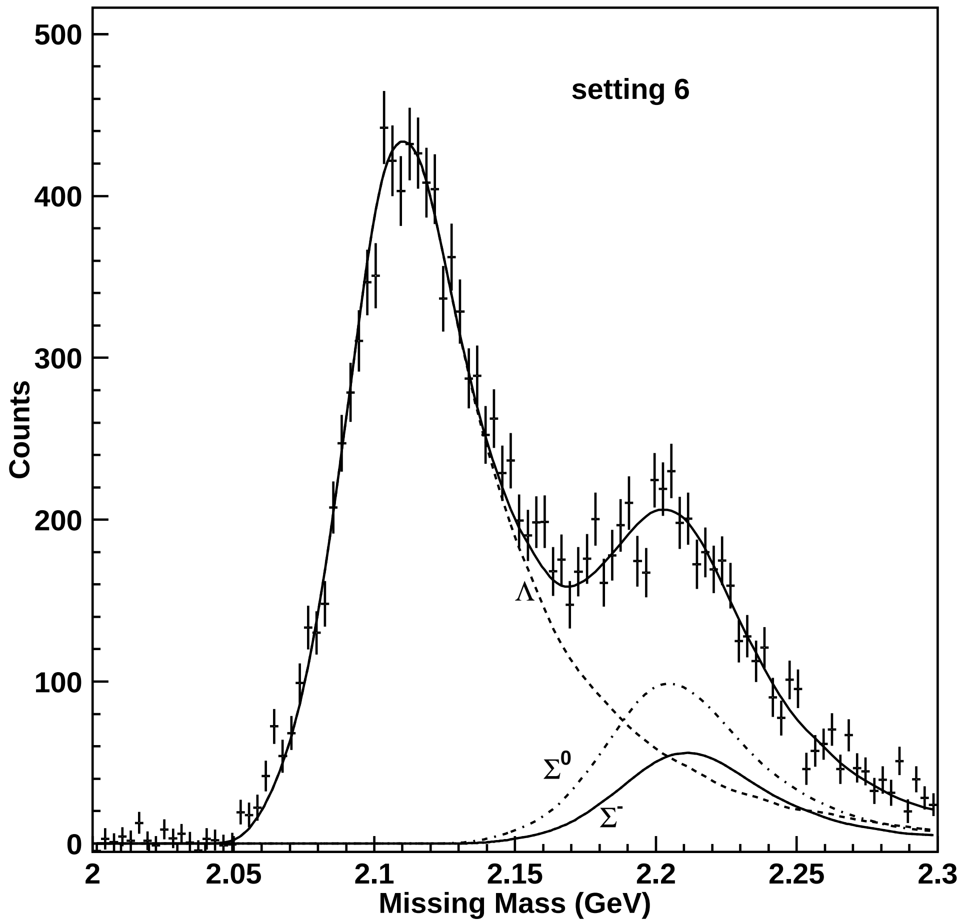

Figure 5.16: Deuterium (e,e′K$^+$) for E_{beam}=3.245 GeV, Q^2=0.38 GeV^2, W=1.90 GeV, $\theta_{\gamma K(lab)}$=6.0°. The simulation is the solid lines, the data are the crosses with statistical errors only.

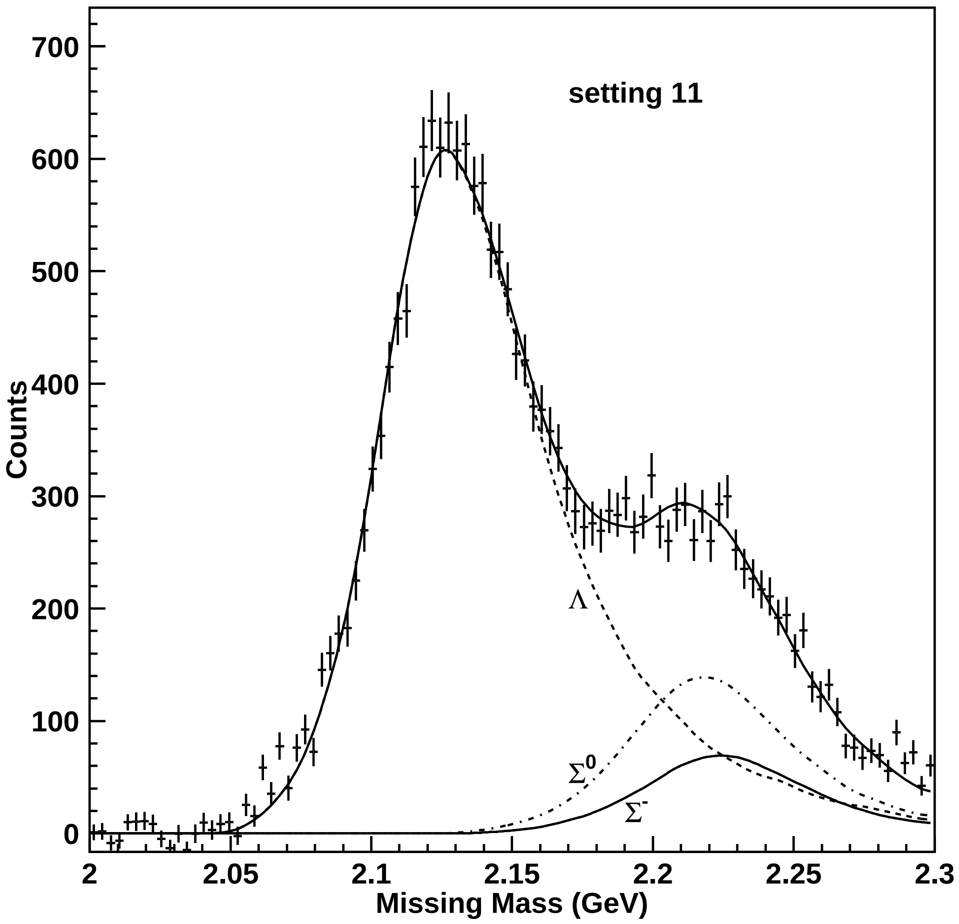

Figure 5.17: Deuterium (e,e′K$^+$) for E_{beam}=3.245 GeV, Q^2=0.38 GeV^2, W=1.90 GeV, $\theta_{\gamma K(lab)}$=11.0°. The simulation is the solid lines, the data are the crosses with statistical errors only.

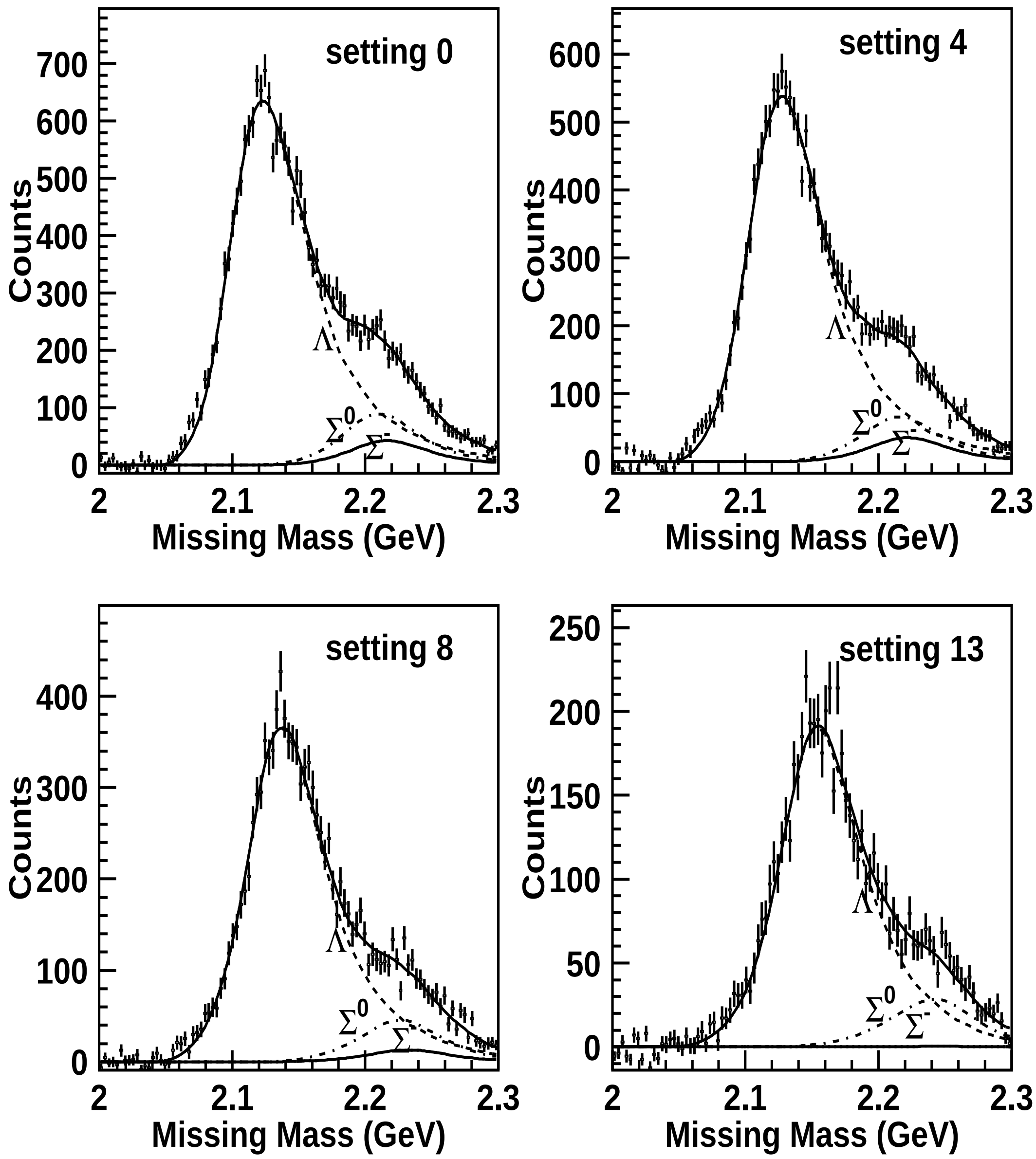

Figure 5.18: Deuterium (e,e$'$K$^+$) for E_{beam}=3.245 GeV, Q^2=0.50 GeV^2, W=1.80 GeV, $\theta_{\gamma K(lab)}$=0.0, 4.3, 8.8, 13.3°. The simulation is the solid lines, the data are the crosses with statistical errors only.

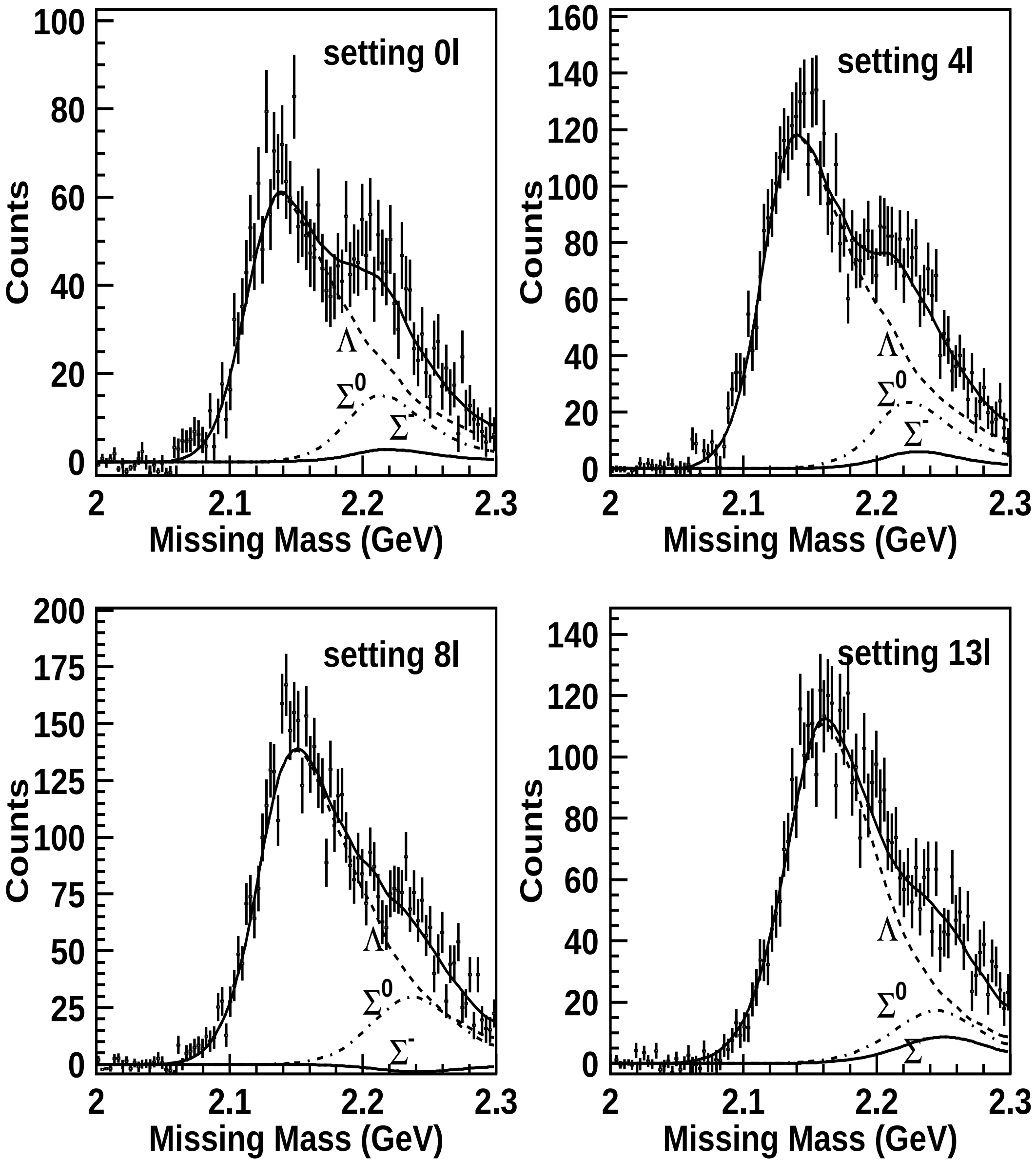

Figure 5.19: Deuterium (e,e′K$^+$) for E_{beam}=3.245 GeV, Q^2=0.52 GeV^2, W=1.76 GeV, $\theta_{\gamma K(lab)}$=0.0, 4.3, 8.8, 13.3°. The simulation is the solid lines, the data are the crosses with statistical errors only.

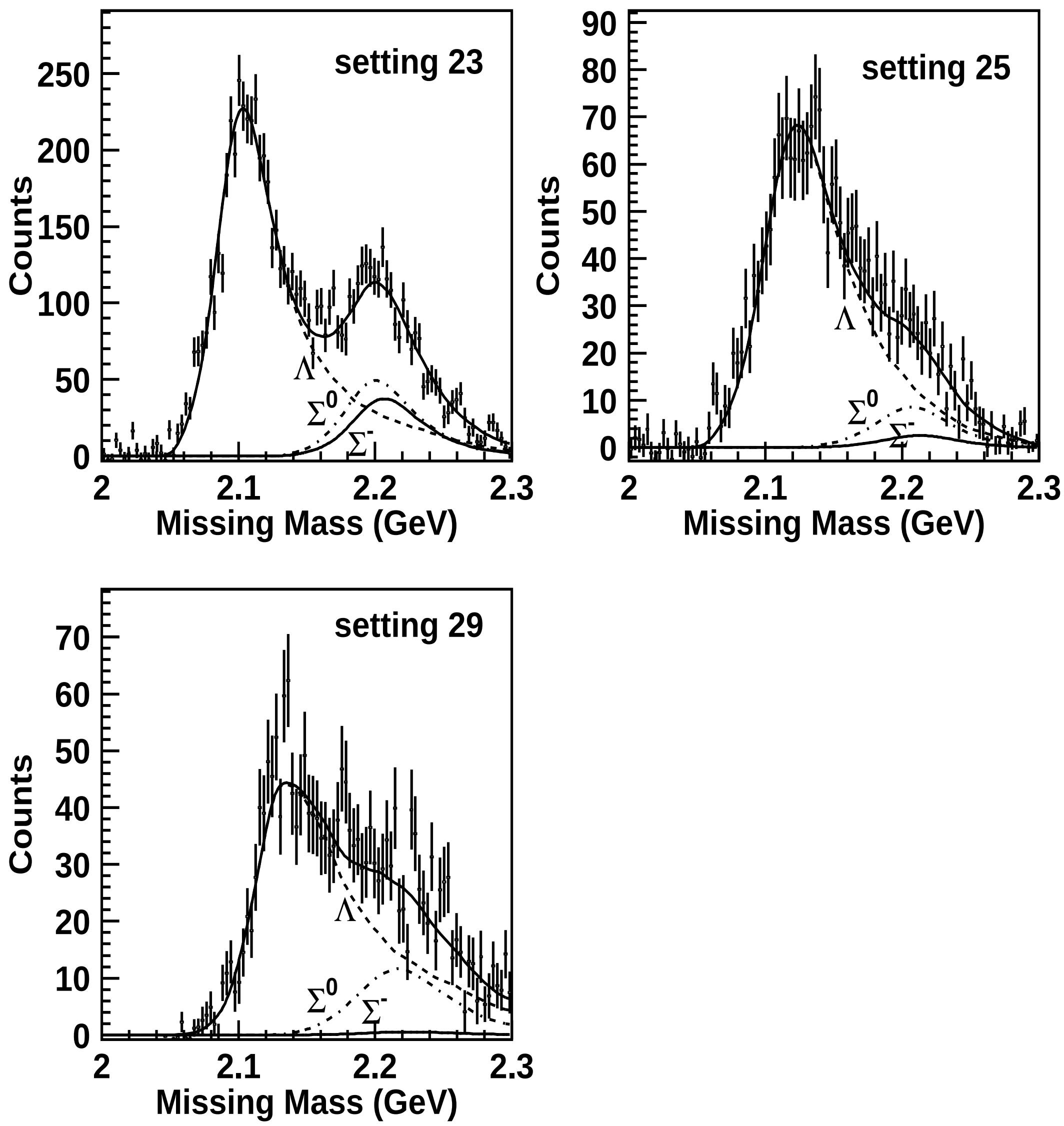

Figure 5.20: Deuterium (e,e′K$^+$) for E_{beam}=2.445 GeV: Q^2=0.38 GeV^2, W=1.87 GeV, $\theta_{\gamma K(lab)}$=1.5° (setting 23); Q^2=0.50 GeV^2, W=1.80 GeV, $\theta_{\gamma K(lab)}$=1.0° (setting 25); and Q^2=0.52 GeV^2, W=1.78 GeV, $\theta_{\gamma K(lab)}$=1.0° (setting 29). The simulation is the solid lines, the data are the crosses with statistical errors only.

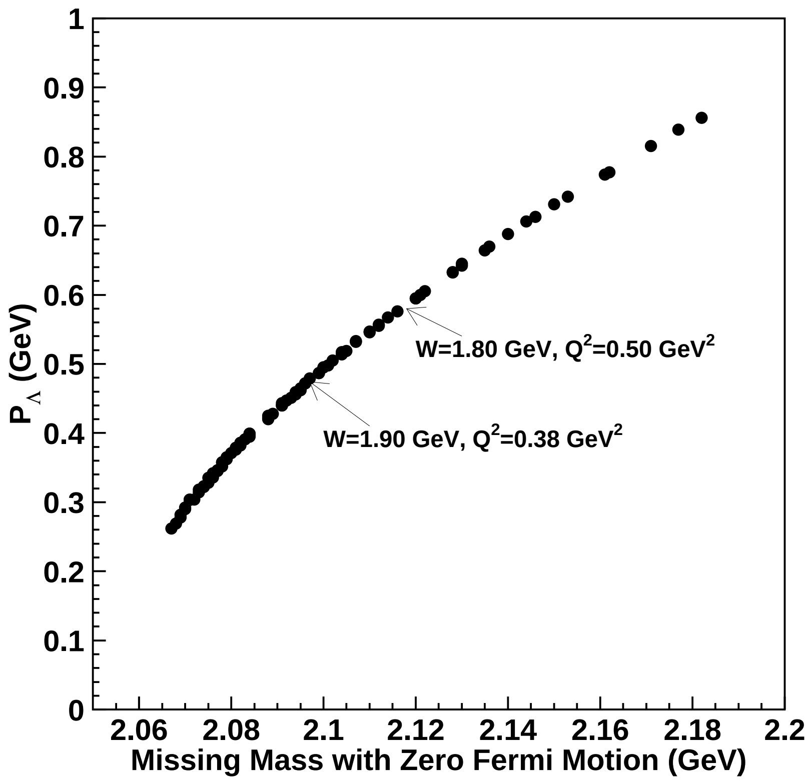

Figure 5.21: Plot of Λ momentum vs. deuterium missing-mass peak. The arrows correspond to the labeled W and Q^2 values at $\theta_{\gamma K}$=0°.

settings, and greater than 25% for the 13, 0l, 4l, 8l, 13l, 25, and 29 settings. The fit errors at these settings are mostly due to the small Σ^- cross sections. If the data are fitted to a Λ and a Σ^0 curve only (looking at combined Σ production), the errors for the Σ^0 fit are 12% or less for all settings.

It is important to remember that the Jacobian in the simulation transforms from the virtual photon-target nucleon center-of-mass frame to the lab frame. Consequently, the cross sections extracted for deuterium are actually cross sections for the proton (neutron for Σ^- production) in deuterium. To avoid confusion with hydrogen cross sections, deuterium cross sections will be labeled as d(e,e$'$K$^+$)YN but should be interpreted as p_{bound}(e,e$'$K$^+$)Y or n_{bound}(e,e$'$K$^+$)Y using the deuteron as a proton or neutron target.

5.2.2 Cross-Section Parameterizations

The offsets depended on the parameterization used for the cross-section weight. Parameterizations that do not describe the data well generally require a large offset such that the simulation coincides with the data (see Fig. 5.22). The dependence of the missing-mass spectrum on the parameterization can be understood by looking at Fig. 5.23. Since missing mass and W are correlated, a parameterization which has larger weights for events below 1.81 GeV will lead to greater strength in the missing-mass spectrum at higher missing masses. The parameterizations used are

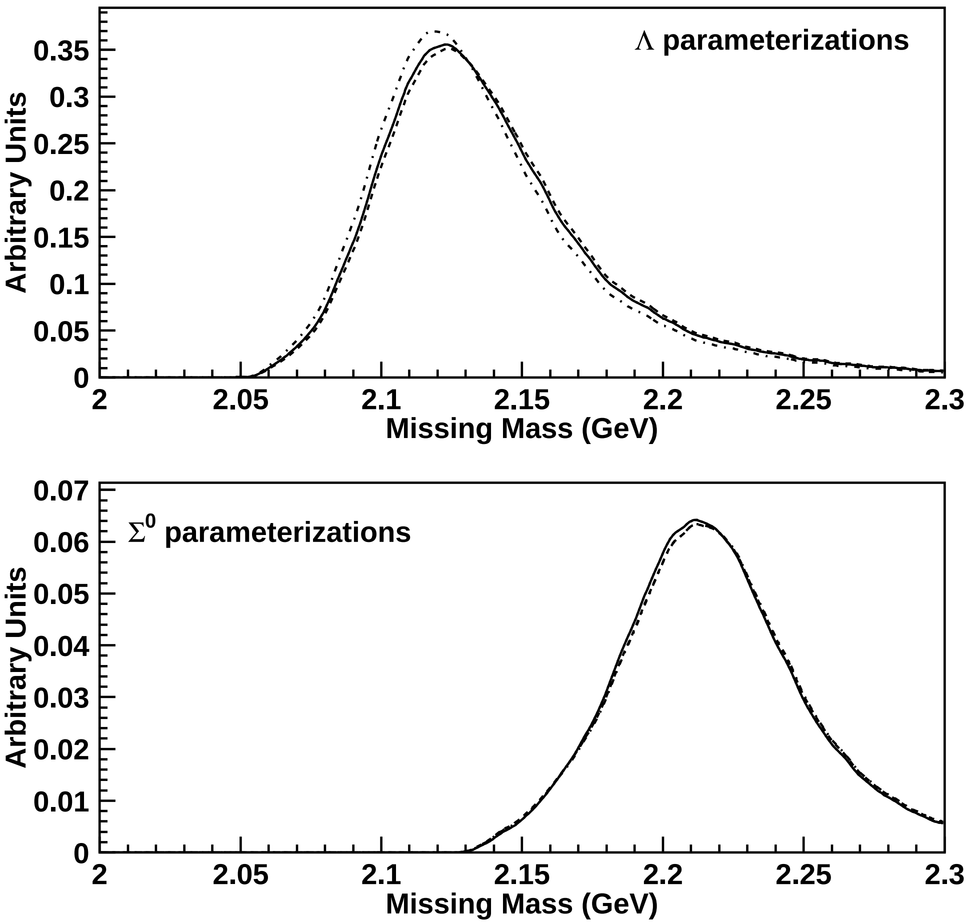

Figure 5.22: Deuterium (e,e$'$K$^+$) SIMC missing-mass spectra for several parameterizations corresponding to setting 0. All spectra have been normalized to have the same total integrals over this missing-mass range. Note that the Σ^0 parameterizations are virtually identical at this setting, but the Λ curve corresponding to a parameterization with a resonant term of zero is significantly different from the other two curves.

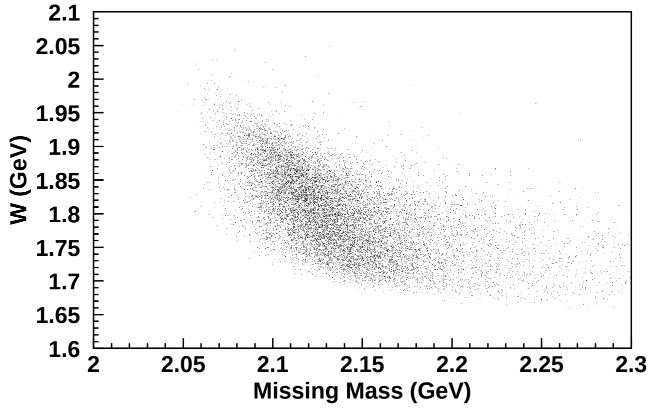

Figure 5.23: Deuterium (e,e$'$K$^+$) W vs. missing mass. Lower values for missing mass are correlated with higher values for W.

the same ones used to analyze the hydrogen data at the same setting. Since the physics dependences of the Σ^- cross section cannot be studied in detail by looking at hydrogen data, it is assumed that the Σ^- parameterization is the same as the Σ^0 parameterization even though the cross-section dependences are likely different for the two final states. It is therefore important to test a number of different parameterizations. Offsets used for the parameterizations used to extract cross sections are generally less than or equal to 3 MeV.

The uncertainties associated with which parameterization is used are once again quite small for Λ production (less than 1.3% for most settings), such that, similar to the hydrogen data, the Λ cross sections are independent of the physics cross-section weight used in the analysis. The errors related to combined Σ production have two components: the errors due to different Λ parameterizations, and the errors due to different Σ parameterizations. The Λ parameterization is important due to the strength of the Λ tail in the Σ missing-mass range. The uncertainties are highly dependent on which group of settings are being studied. The low-Q^2 settings have errors due to Λ parameterization of less than 4% and errors due to Σ parameterization of less than 1%. For settings 0, 4, and 8 the corresponding numbers are 5% and 3%. The other settings range from 6–16% and from 1–10%.

The way in which invariant mass W in the parameterization is calculated is important as well. As mentioned in Chapter 1, there are several ways to consider the off-shell nature for deuterium. In any case, the velocity of the target nucleon has to be taken into account in the computation of W. For data taken at the same setting for different targets the average W is different for each target. In this analysis W is calculated assuming the struck nucleon is on-shell, although the choice of assuming the struck nucleon is off-shell has been evaluated also and is included in the systematic error, and is generally less than 3% for Λ and combined Σ production.

The quality of the fits of the simulation to the data can be seen in both the missing-mass spectra (Figs. 5.15–5.20) and in the subtraction of the simulation from the data (Figs. 5.28–5.30). A comparison of the total number of data and simulation counts over different missing-mass regions is found in Table 5.8. The fits are much worse for the 13, 0l, 4l, 8l, 13l, 25, and 29 settings and could be

Table 5.8: Comparison of deuterium (e,e′K^+) data and SIMC after having fit the simulation to the data.

setting	Λ Data Counts 2.08–2.16 GeV	Λ SIMC Counts 2.08–2.16 GeV	% Diff	Σ Data Counts 2.18–2.24 GeV	Σ SIMC Counts 2.18–2.24 GeV	% Diff
0	12508	12442	0.5	4472	4402	1.6
4	10243	10241	0.0	3788	3702	2.3
8	6423	6360	1.0	2624	2577	1.8
13	2674	2548	4.7	1770	1818	-2.7
0l	1135	1036	8.7	892	816	8.5
4l	2073	1947	6.1	1510	1470	2.6
8l	2184	2023	7.4	1699	1716	-1.0
13l	1328	1294	2.6	1557	1470	5.6
1	17047	17133	-0.5	7210	7469	-3.6
6	8129	8120	0.1	3581	3567	0.4
11	11432	11371	0.5	5509	5523	-0.3
23	4112	4092	0.5	1979	1909	3.7
25	1365	1324	3.1	516	463	11.4
29	810	751	7.9	617	548	12.6

systematically low at some of these settings, but in most cases they agree to better than 10%. The subtractions show no unusual structure in general other than near the Λ threshold at 2.055 GeV and possibly near 2.165 GeV (see below for a further discussion).

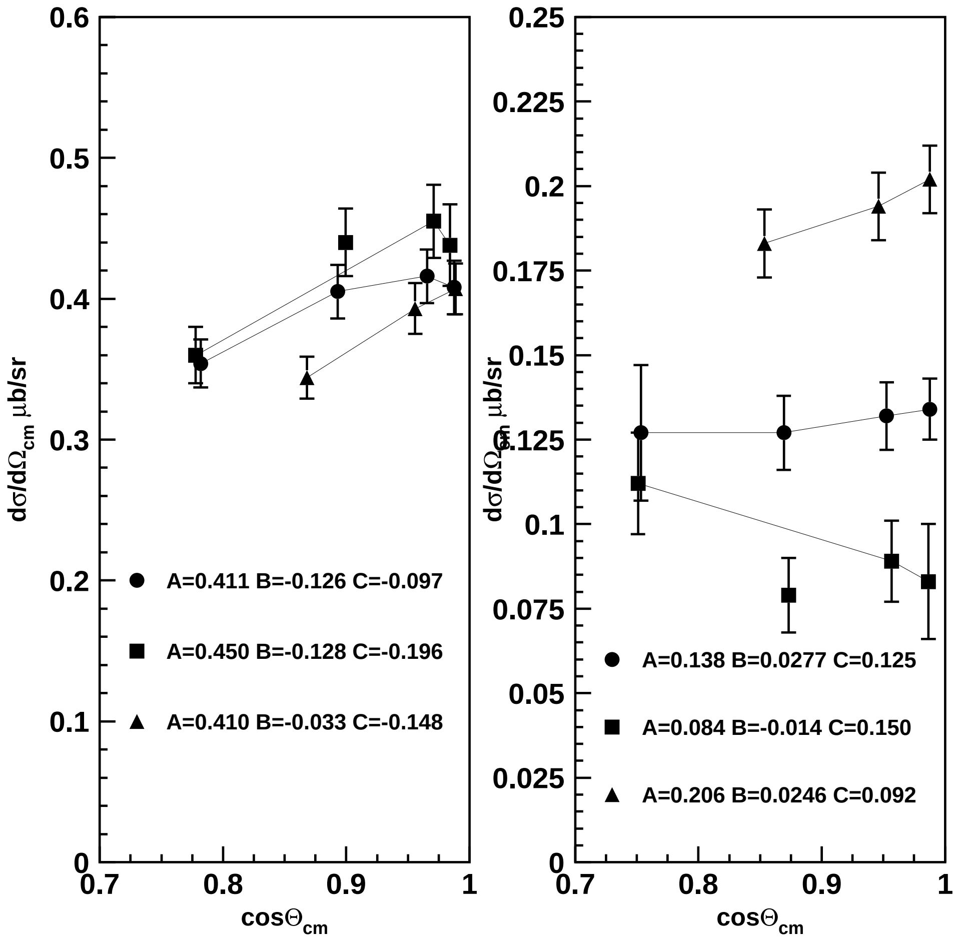

Figure 5.24: Deuterium (e,e′K$^+$)Λn,ΣN angular parameterizations. The lines are fitted to the data points using the parameterization (A+Bsin $\theta \cos\phi$+Csin$^2\theta$ $\cos 2\phi$)cos θ. The point corresponding to setting 8l has been left out of both fits.

5.2.3 Angular Dependence

The angular distributions for the deuterium data are displayed in Fig. 5.24. The angular dependences are almost identical to the ones seen for hydrogen. The contribution of interference terms for Λ production are less drastic than for hydrogen: from both setting 0 to setting 4 and from setting 0l to setting 4l the interference term contribution is equal to $-0.023 \cos\phi$ μb/sr. At the same time, the deuterium data reinforces the implication that the contribution of the interference terms turns on somewhere between 1.80 GeV and 1.90 GeV. The contribution from Σ^- production can be seen by comparing hydrogen Σ^0 and deuterium combined Σ angular distributions. It appears as if the Σ^- angular distribution differs from the Σ^0, a statement that will be looked at more closely below.

5.2.4 Deuterium/Hydrogen Ratio

An important check on the procedure (and an interesting result in its own right) is the comparison of Λ cross sections on hydrogen and deuterium at the same settings. As mentioned above, the average W for hydrogen data for a given setting is not equal to the average W for deuterium data at that same setting. Using the W-dependence derived for hydrogen, deuterium cross sections are extrapolated to the cross sections for the average W of the corresponding hydrogen data. Extrapolated Λ p_{bound} cross sections and the ratios to hydrogen cross sections are

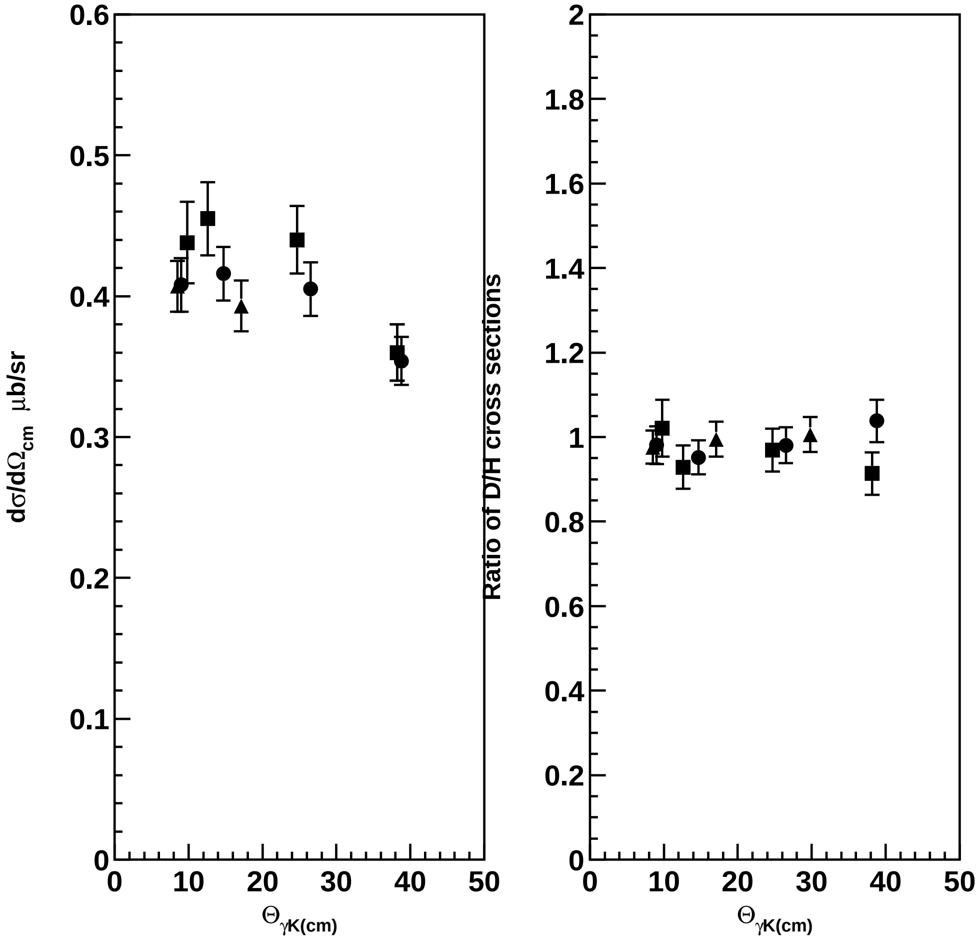

Figure 5.25: Deuterium (e,e$'$K$^+$)Λn experimental cross sections. Deuterium data have been scaled in W to the hydrogen W at the same setting using the W-dependence previously derived. On the right is the ratio of deuterium/hydrogen cross sections. The weighted average is 0.977±0.032.

shown in Fig. 5.25. The Λ ratios are very close to 1.00 and are virtually independent of W, Q^2, and θ_{cm}. Fitting the ratios to a linear term plus a constant gives $(0.972 \pm 0.044) + (0.0002 \pm 0.0019)\theta_{cm}$, confirming the lack of θ_{cm} dependence. The weighted average is 0.977$\pm$0.032. A previous back-of-the-envelope calculation for what this ratio should be gives 0.957 [Boy71], and the only previous experimental measurement of this ratio, for photoproduction at W=4.6 GeV, was 1.02$\pm$0.04$\pm$0.05 [Boy71].

Fig. 5.26 shows extrapolated cross sections for the combined Σ on deuterium as well as ratios to hydrogen Σ^0 production. First of all, it is clear that there is more than the Σ^0 contributing to the combined Σ cross section since the ratio is not 0.977 as it was for the Λ. It is also interesting to see the dependences on W/Q^2 and on θ_{cm}. The only previous measurements of this ratio are for photoproduction at W=4.6 and 5.6 GeV. The ratio (a ratio of $d\sigma/dt$) measured at 5.6 GeV was 2.73$\pm$0.18 [Qui79], and the corresponding measurement at 4.6 GeV was 2.37$\pm$0.11$\pm$0.12 [Boy71], although the super-ratio calculated by dividing the ratio of deuterium to hydrogen Σ cross sections by the ratio of deuterium to hydrogen Λ cross sections was given as 2.07$\pm$0.19. As mentioned in Chapter 1, the expectation was that if the only contributions to the cross section came from t-channel diagrams, the ratio should be 3.00, with the Σ^- cross section being twice the Σ^0 cross section. At the same time, the ratios extracted from the previous

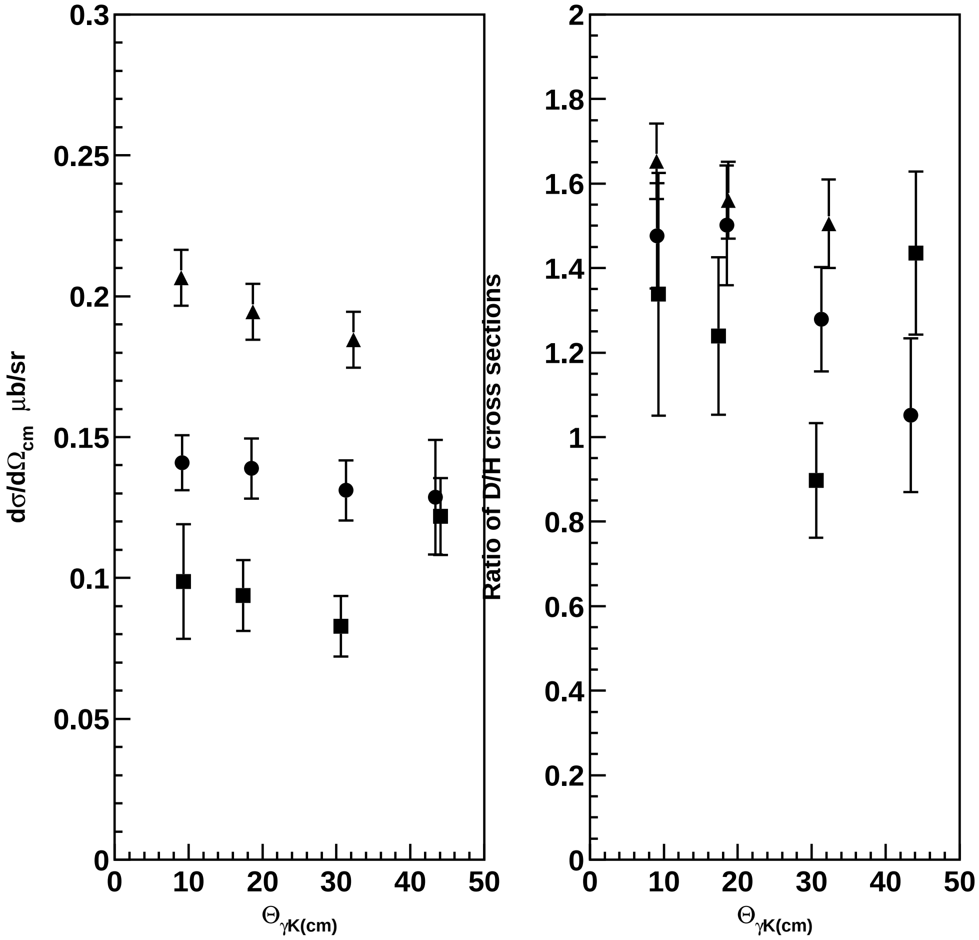

Figure 5.26: Deuterium (e,e′K$^+$)ΣN experimental cross sections. Deuterium data have been scaled in W to hydrogen at the same setting using the W-dependence previously derived. On the right is the ratio of deuterium/hydrogen cross sections.

electroproduction measurement [Beb77] found ratios (with 50–200% error bars) that ranged between 1.2 and 1.8 at the same range in θ_{cm} but higher W and Q^2 values than probed in this experiment. One current theoretical model for kaon photoproduction predicts total cross-section ratios around 1.8 [Ben99]. For this set of data the ratios for $d\sigma/d\Omega_{cm}$ are found to range from 0.9 to 1.7 (most within the range 1.2 to 1.7) with error bars one-tenth those from the previous electroproduction measurement. Adding the cross sections over the angular distributions for each W/Q^2 value gives ratios of 1.59±0.07 for settings 1, 6, and 11, 1.34±0.09 for settings 0, 4, 8, and 13, and 1.24±0.11 for settings 0l, 4l, 8l, and 13l.

5.2.5 Cross Sections

Cross sections for Σ^- production are shown in Fig. 5.27. Cross sections can be obtained in two different ways. The first is to fit the deuterium data to two curves (Λ and Σ^0) and subtracting from the combined Σ cross section the Σ^0 cross section on hydrogen scaled by the ratio of deuterium to hydrogen Λ cross sections. The second is to fit the deuterium data to three curves (Λ, Σ^0, and Σ^-) where the strength of the Σ^0 curve is fixed such that it corresponds to the Σ^0 cross section on hydrogen scaled by the ratio of deuterium to hydrogen Λ cross sections. The results from using the two methods are quite similar since the Σ^0 and Σ^- only differ by 5 MeV in mass, and the cross sections obtained using the first method are

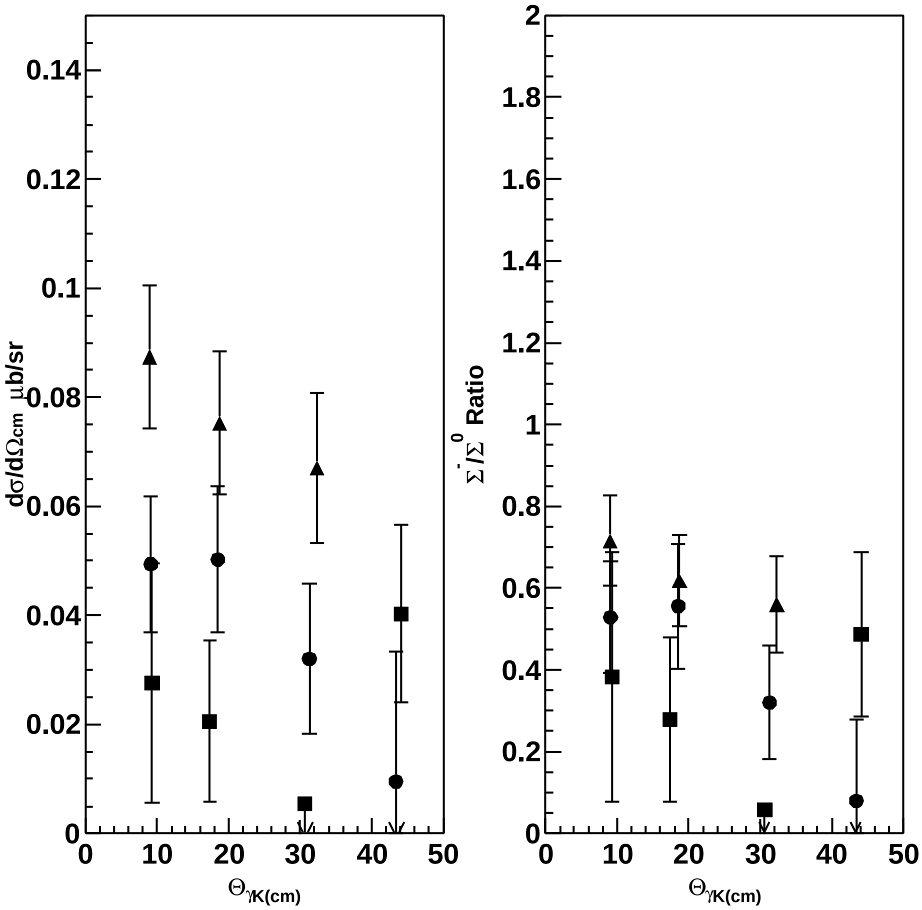

Figure 5.27: Deuterium $n_{bound}(e,e'K^+)\Sigma^-$ experimental cross sections, obtained by subtracting the Σ^0n cross section (equal to the Σ^0 cross section on hydrogen times the ratio of deuterium/hydrogen for Λ production at the same setting) from the total ΣN cross section on deuterium. Deuterium data have been scaled in W to hydrogen at the same setting using the W-dependence previously derived. On the right is the ratio of Σ^-/Σ^0 cross sections on deuterium.

presented here (see Table 5.9). For all settings, the cross sections obtained using the second method are within 0.003 μb/sr of these values.

The Σ^- cross sections are dependent on W/Q^2 and decrease as a function of increasing θ_{cm}. The ratios of Σ^-/Σ^0 cross sections follow the ratios of combined Σ/Σ^0 cross sections shown in Fig. 5.26. These ratios also are dependent on W/Q^2 and decrease with increasing θ_{cm}. The differences between the behavior of Σ^- and Σ^0 cross sections imply that the dominant production mechanisms for the two final states are not the same. The cross sections are the world's first precision measurements for $n_{bound}(e,e'K^+)\Sigma^-$. Also in Table 5.9 are cross sections for free neutrons for which the assumption is made that the ratio of cross sections on a deuterium target and a free target is the same for Σ^- production as it is for Λ production. Similar to the situation with the hydrogen data mentioned at the end of the previous section, there are currently no theoretical predictions for Σ^- production for this experiment. Certainly these results will provide tight constraints on theories that have cross sections that vary by a factor of 100 [Mar95].

5.2.6 Subtractions of SIMC from Data

Subtractions of data and simulation missing-mass spectra can be used to determine whether any physical process other than quasi-free kaon electroproduction is making a contribution. Looking at the subtractions, in general it seems as if there

Table 5.9: Deuterium (e,e$'$K$^+$) Λn, ΣN, and Σ^-p cross sections. Cross sections are in the center-of-mass of the virtual photon-target nucleon system. The n$_{free}$(e,e$'$K$^+$)Σ^- cross sections are the deuterium cross sections divided by 0.977. See Tables 5.5 and 5.6 for the average values for kinematic variables to which these settings correspond. Deuterium data have been scaled in W to hydrogen at the same setting using the W-dependence previously derived.

setting	p$_{bound}$(e,e$'$K$^+$)Λ μb/sr	(e,e$'$K$^+$)Σ μb/sr	n$_{bound}$(e,e$'$K$^+$)Σ^- μb/sr	n$_{free}$(e,e$'$K$^+$)Σ^- μb/sr
0	0.408±0.019	0.141±0.010	0.049±0.012	0.050±0.013
4	0.416±0.019	0.139±0.011	0.050±0.013	0.051±0.014
8	0.405±0.019	0.131±0.011	0.032±0.014	0.033±0.014
13	0.354±0.017	0.129±0.020	0.009±0.024	0.010±0.024
0l	0.438±0.029	0.099±0.020	0.028±0.022	0.028±0.022
4l	0.455±0.026	0.094±0.013	0.021±0.015	0.021±0.015
8l	0.440±0.024	0.083±0.011	-0.008±0.014	-0.008±0.015
13l	0.360±0.020	0.122±0.014	0.040±0.016	0.041±0.017
1	0.407±0.018	0.207±0.010	0.087±0.013	0.089±0.013
6	0.393±0.018	0.194±0.010	0.075±0.013	0.077±0.013
11	0.344±0.015	0.185±0.010	0.067±0.014	0.069±0.014
23	0.373±0.018	0.178±0.012	0.075±0.015	0.076±0.015
25	0.383±0.021	0.099±0.018	0.033±0.022	0.033±0.022
29	0.400±0.028	0.087±0.015	0.013±0.020	0.013±0.020

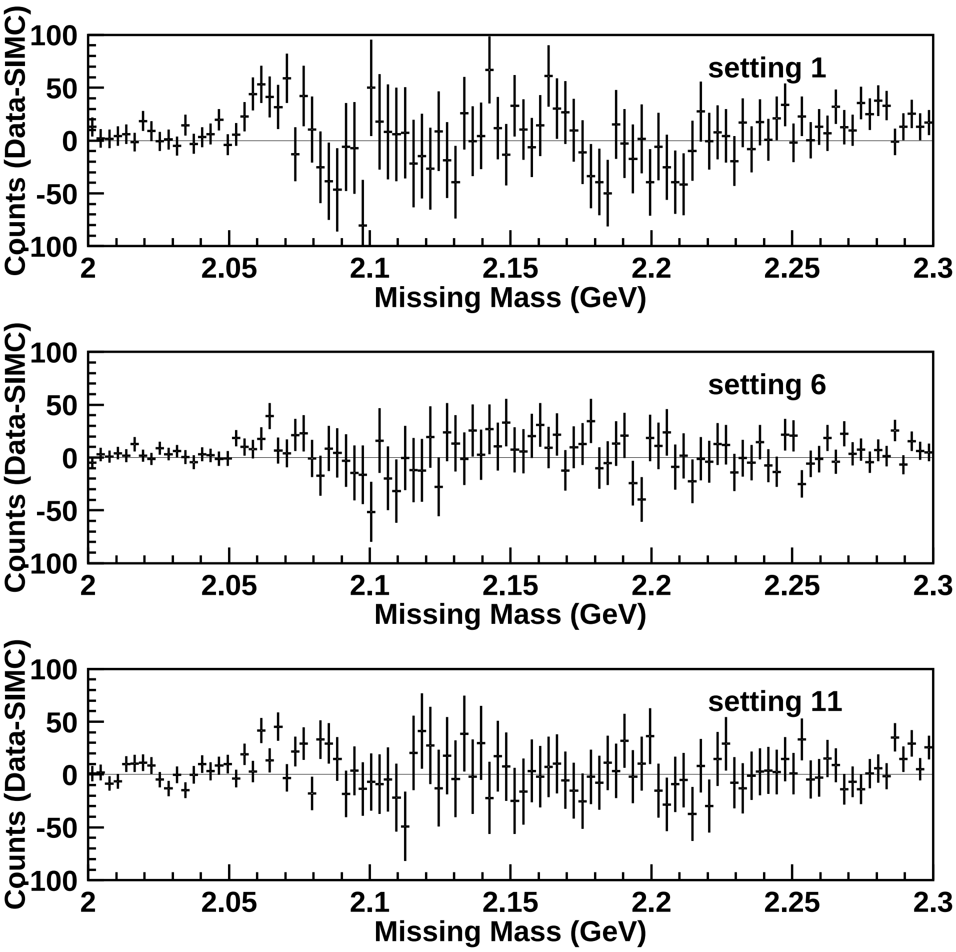

Figure 5.28: Deuterium (e,e′K$^+$) Data-SIMC for E_{beam}=3.245 GeV, Q^2=0.38 GeV^2, W=1.90 GeV, $\theta_{\gamma K(lab)}$=1.5, 6, 11°. Only statistical errors are shown.

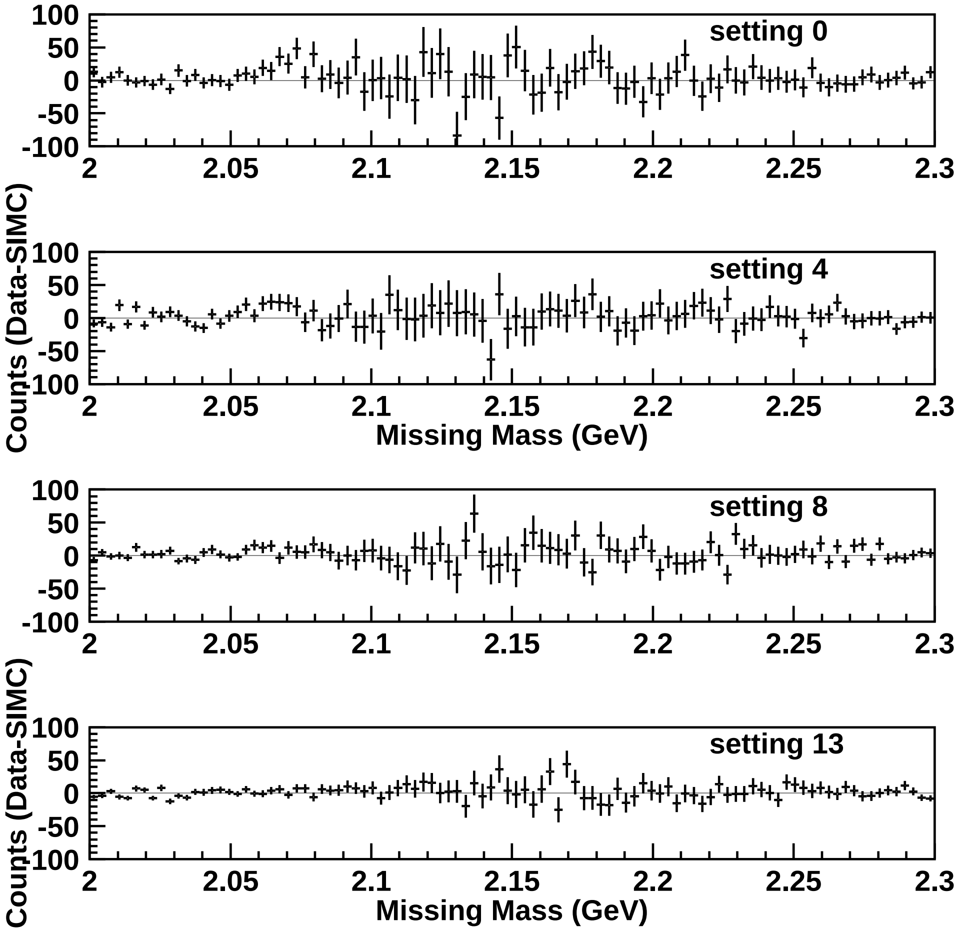

Figure 5.29: Deuterium (e,e$'$K$^+$) Data-SIMC for E_{beam}=3.245 GeV, Q^2=0.50 GeV^2, W=1.80 GeV, $\theta_{\gamma K(lab)}$=0, 4.3, 8.8, 13.3°. Only statistical errors are shown.

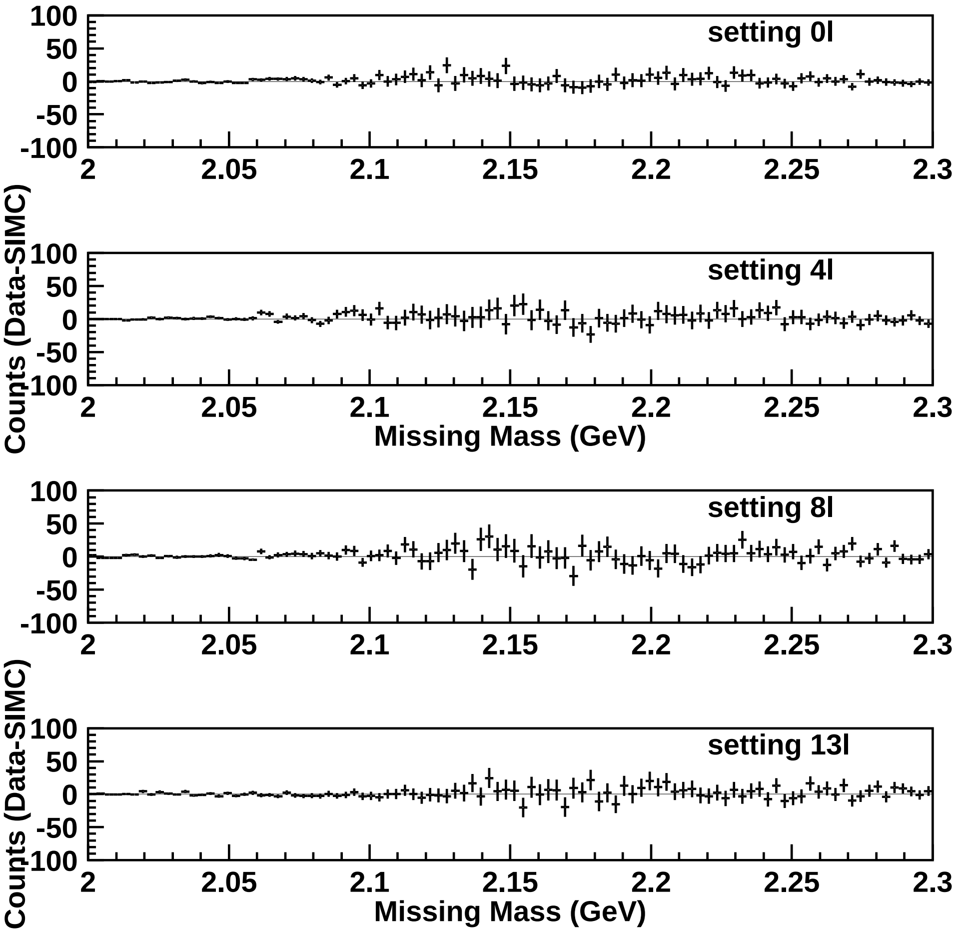

Figure 5.30: Deuterium (e,e$'$K$^+$) Data-SIMC for E$_{beam}$=3.245 GeV, Q^2=0.52 GeV^2, W=1.76 GeV, $\theta_{\gamma K(lab)}$=0, 4.3, 8.8, 13.3°. Only statistical errors are shown.

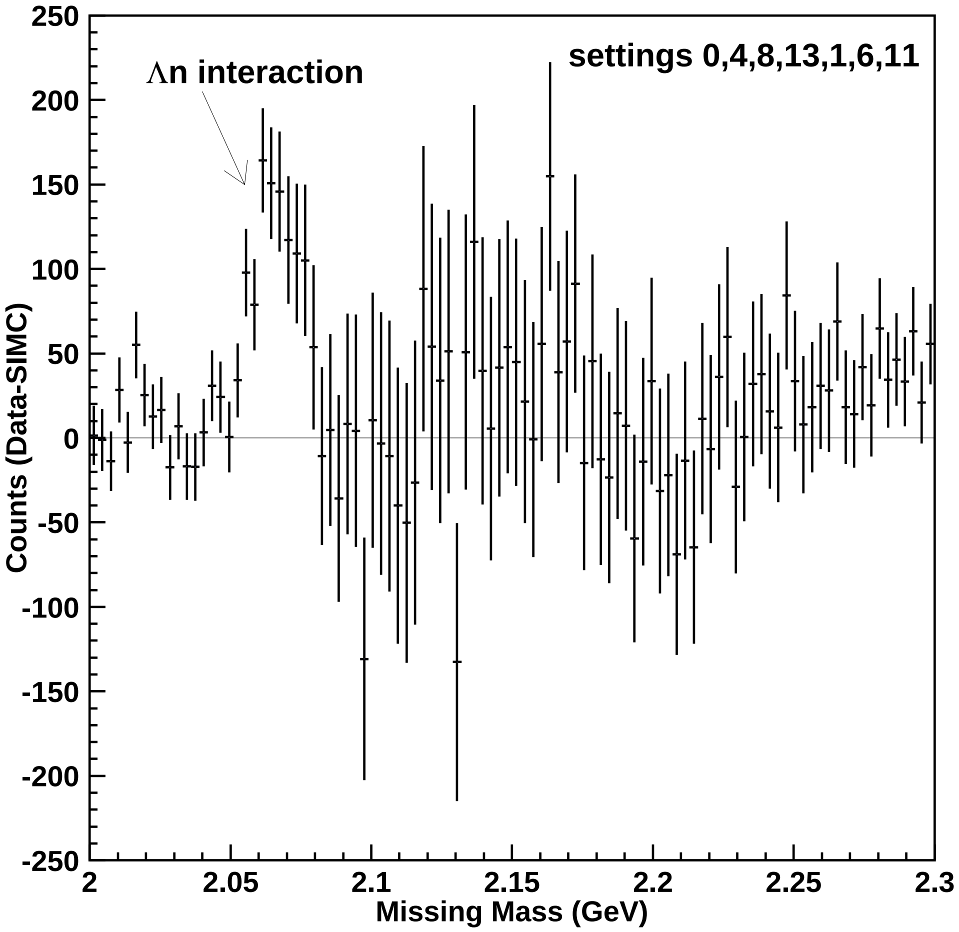

Figure 5.31: Deuterium (e,e$'$K$^+$) Data-SIMC for settings 0, 4, 8, 13, 1, 6, 11. Only statistical errors are shown.

is very little that is not well described by the simulation. The main exception is at the Λ threshold, where an enhanced yield is seen due to Λ–n final state interaction. The subtractions for the 0 and 1 settings are the only ones where significant fluctuations are seen in other missing-mass locations. Setting 1 appears to have a peak near 2.165 GeV, but the fit over the region 2.165–2.185 GeV appears to be poor and the average over that region is zero. If that peak is ignored then that setting does not have any other broad unexplained structures. The 0 setting appears to have a peak near 2.180 GeV. However, the average over the region 2.180–2.200 GeV is close to zero, so for both settings the existence of excesses in that area could simply be due to flaws in the Σ parameterization. The 0 setting also has two high points near 2.150 GeV, but their significance is mitigated by the low point just below them.

Looking at the combined subtractions from several settings (Fig. 5.31), there are only three bins (bin width 3 MeV) with significant deviations: at 2.097 GeV (135 counts below local average), 2.130 GeV (200 counts below local average), and 2.165 GeV (120 counts above local average). The Σ^0n threshold is at 2.130 GeV, and there are dibaryonic states predicted at 2.110 GeV and 2.164 GeV [Mul80], although the presence of dibaryonic states would be indicated by an enhancement in the yield rather than by not having enough counts in a bin. This analysis does not demonstrate the existence of dibaryonic states.

The excess data counts over the region 2.055–2.080 GeV can be explained with confidence as originating from the Λ–n final state interaction. A model exists to describe the effect of that interaction, and the model output fits well to the data. Analysis of this excess yield (that peaks at small θ_{cm} and falls off significantly as θ_{cm} increases) will not only quantify the strength of this interaction, but will also provide a measurement of the Λ–n scattering length [Cha99b].

5.3 Summary

An outstanding set of data has been collected on hydrogen and deuterium kaon electroproduction. Angular distributions have been measured for both targets, and Λ and Σ^- production appear to be forward-peaked, whereas Σ^0 production is angle-independent over the measured range. Cross sections for Σ^0 are ϕ-independent, whereas Λ cross sections have a ϕ-dependence that turns on somewhere between W=1.80–1.90 GeV. With an assumed Q^2 dependence, the W-dependence for Λ and Σ^0 production has been analyzed. Both reactions follow a simple phase-space factor dependence derived from earlier electroproduction data, but only above 1.81 GeV. Below that point both Λ and Σ^0 production have strong deviations indicative of contributions/interference of resonance channels. Deuterium missing-mass spectra are well described by quasi-free production along with the contribution of a final state interaction at the Λ–n threshold. Deuterium Λ cross sections are found to be 0.977 times the strength of corresponding hydrogen cross sections. Combined Σ deuterium cross sections are found to be 1.2–1.7 times the strength of Σ^0 cross sections on hydrogen. Cross section dependences for Σ^- production are dramatically different from those for Σ^0 production. Cross sections for Σ^- production have been measured with error bars one-tenth those from the only previous measurement.

Appendix A

Basic Structure of SIMC

*indicates subroutine call

simulate:

    *dbase_read:

        reads .inp file, other input files

        initializes random seeds, assign flags

            *target_init:

                calculates energy loss in target

            *limits_init:

                sets boundaries for generation, radiation

            *results_init: (not used)

    *radc_init:

initializes radiation flags

*brem_init:

initializes radiation flags

*calculate_central: (not important)

*complete_ev: (described later)

*radc_init_ev: (described later)

*complete_main: (described later)

calculates luminosity

start of event loop

*generate:

calculates raster position (default sine wave)

calculates position at target

calculates energy loss in target

picks flat distribution of angles, energies

picks initial nucleon momentum if not doing hydrogen

(based on probability distribution generated from

Bonn potential for deuterium)

*complete_ev:

calculates 4-vectors for outgoing electron, virtual photon

solves for hadron momentum

(assuming spectator nucleon is on-shell)

calculates 4-vector for hadron

calculates missing momentum (and energy)

*radc_init_ev:

calculates lambdas

*bremos:

calculates hard rad weight

*basicrad_init_ev:

calculates c's, g's

*generate_rad:

rad_flag 0:

picks an arm for radiation

*basicrad:

calculates radiated photon energy

calculates basicrad weight

if necessary, calls *complete_ev

calculates radiative weight

*peaked_rad_weight:

calculates external weight

*bremos:

calculates internal weight

OR rad_flag 2:

basicrad weight×extrad_phi

if necessary, calls *complete_ev

calculates main.gen_weight

*montecarlo:

checks if initial 4-vectors fall within loose spectrometer cuts

*mc_sos:

transports through SOS spectrometer

checks collimator, apertures

uses sequential matrix elements

*mc_sos_hut:

transports through SOS hut

checks detector limits

does multiple scattering

calculates focal plane quantities

*mc_sos_recon:

reconstructs target quantities

checks if target quantities fall within tight spectrometer cuts

*mc_hms:

same as for mc_sos

(except uses forward matrix elements)

checks if target quantities fall within tight spectrometer cuts

*complete_ev: (recon mode)

*complete_main:

*peepi:

calculates center-of-mass kinematic quantities

calculates center-of-mass cross section

(using theoretical model)

calculates jacobian

calculates virtual photon flux

calculates decay

calculate main.weight

*inc:

increments .gen quantities

*results_update: (not used)

*limits_update:

updates ranges for final report

*results_ntu_write:

fills ntuple

end of event loop

calculates generation volume

calculates normalization factor

writes .gen file

*results_write: (not used)

*report:

writes .hist file

Bibliography

[Abr71] R.J. Abrams et al., Phys. Rev. D **4**, 3235 (1971).

[Abb95] D. Abbott et al., *The CODA System and its Performance in the First Online Experiments at CEBAF*, Proceedings of the 1995 IEEE Conference on Real-Time Computing Applications in Nuclear, Particle and Plasma Physics (May 1995), pp. 147–151.

[Ade88] R.A. Adelseck, dissertation, Ohio University (unpublished) (1988).

[Ade90] R.A. Adelseck and B. Saghai, Phys. Rev. C **42**, 108 (1990).

[Arr98] J. Arrington, dissertation, California Institute of Technology (unpublished) (1998).

[Ass97] K. Assamagan, D. Dutta, and P. Welch, *Hall C Matrix Element Optimization Package (CMOP)*, TJNAF Hall C Document (unpublished) (1997).

[Beb77] C.J. Bebek et al., Phys. Rev. D **15**, 594 (1977).

[Ben99] C. Bennhold et al., preprint nucl-th/9901066 (1999).

[Ber90a] M. Berz, Nuc. Inst. and Methods A298, 473 (1990).

[Ber90b] M. Berz, Nuc. Inst. and Methods A298, 426 (1990).

[Boc94] M. Bockhorst et al., Z. Phys. C **63**, 37 (1994).

[Boy69] A.M. Boyarski et al., Phys. Rev. Lett. **22**, 1131 (1969).

[Boy71] A.M. Boyarski et al., Phys. Lett. **34B**, 547 (1971).

[Bra79] P. Brauel et al., Z. Phys. C **3**, 101 (1979).

[Bro82] K. Brown, *A First- and Second-Order Matrix Theory for the Design of Beam Transport Systems and Charged Particle Spectrometers*, SLAC Report-75 (1982).

[Cas98] C. Caso et al., The European Physical Journal **C3**, 1 (1998).

[Cer94] CERN Program Library Long Writeup D506, *MINUIT–Function Minimization and Error Analysis*, Version 94.1 (1994).

[Cer95] CERN Program Library Long Writeup Q121, *PAW–Physics Analysis Workstation* (1995).

[Cha99a] J. Cha, private communication.

[Cha99b] J. Cha, dissertation, Hampton University (unpublished, currently unfinished) (1999).

[Coo61] V. Cook et al., Phys. Rev. Lett. **7**, 182 (1961).

[Cum96] W. Cummings, The SOS Handbook, Rev. 1.1, TJNAF Hall C Document (unpublished) (1996).

[Dav96] J.C. David et al., Phys. Rev. C **53**, 2613 (1996), and B. Saghai, private communication.

[Dov82] C.B. Dover and G.E. Walker, Phys. Rep. **89**, 1 (1982).

[Dun97] J. Dunne, *Cryo and Dummy Target Information*, TJNAF Hall C Document (unpublished) (1997).

[Dut99] D. Dutta, dissertation, Northwestern University (unpublished) (1999).

[Gas98] D. Gaskell, private communication.

[Gee96] D. Geesaman, *Computer Dead Time and Prescaling Corrections*, TJNAF Hall C Document (unpublished) (1996).

[Gus96] K. Gustafsson, *Cryotarget Density Dependence on Beam Current*, TJNAF Hall C document (unpublished) (1996).

[Hab98] H. Haberzettl, C. Bennhold, T. Mart, and T. Feuster, Phys. Rev. C **58**, R40 (1998).

[Kra93] G. Krafft and A. Hofler, *How the Linac Beam Position Monitors Work*, CEBAF-TN-93-004 (1993).

[Li92] Xiaodong Li, L.E. Wright, and C. Bennhold, Phys. Rev. C **45**, 2011 (1992).

[Mac87] R. Machleidt et al., Phys. Rep. **149**, 1 (1987).

[Mac98] D. Mack, private communication.

[Mak94a] N.C.R. Makins et al., Phys. Rev. Lett. **72**, 1986 (1994).

[Mak94b] N. Makins, dissertation, Massachusetts Institute of Technology (unpublished) (1994).

[Mak98] N.C.R. Makins, et al., to be published.

[Mar95] T. Mart, C. Bennhold, and C.E. Hyde-Wright, Phys. Rev. C **51**, R1074 (1995).

[Moh98] R. Mohring, private communication.

[Moh99] R. Mohring, private communication.

[Mul80] R.J. Mulders, A.Th.M Aerts, and J.J. de Swart, Phys. Rev. D **21**, 2653 (1980).

[Nic96] G. Niculescu, *Resonant Cavities Used as Beam Current Monitors*, TJNAF Hall C Document (unpublished) (1996).

[Nic98a] G. Niculescu et al., Phys. Rev. Lett. **81**, 1805 (1998).

[Nic98b] G. Niculescu, dissertation, Hampton University (unpublished) (1998).

[One94] T.G. O'Neill, dissertation, California Institute of Technology (unpublished) (1994).

[Qui79] D.J. Quinn et al., Phys. Rev. D **20**, 1553 (1979).

[Rei98] J. Reinhold, private communication.

[Van98] D. VanWestrum, dissertation, University of Colorado (unpublished) (1998).

[Wei89] W. Weise, Il Nuovo Cimento **102A**, 265 (1989).

[Wil92] R.A. Williams, C.-R. Ji, and S.R. Cotanch, Phys. Rev. C **46**, 1617 (1992).

[Yan94] C. Yan, CEBAF-PR-94-002 (1994).